Episodic density-induced current velocities at the Gemini offshore wind park

M.Sc. Thesis

June 30, 2016

Episodic density-induced current velocities at the Gemini offshore wind park

by

Christiaan Claessens

in partial fulfillment of the requirements for the degree of

Master of Science

in Hydraulic Engineering

at the Delft University of Technology,
to be defended publicly on 1 July, 2016 at 11:00 AM
in lecture room E of the CiTG building.

Supervisor:	Prof.dr. J.D. Pietrzak,	
Thesis committee:	Dr. ir. G.J. de Boer,	Van Oord
	Dr. ir. M. Verlaan,	TU Delft
	Ir. S. Rijnsburger,	TU Delft

An electronic version of this thesis is available at
http://repository.tudelft.nl/.

TU Delft Delft University of Technology

Van Oord
Marine ingenuity

Abstract

This thesis investigates the origin of observed current velocities at the Gemini offshore wind farm in 2015. Currents have been measured of 1.2 m s^{-1} while, based upon tidal and storm predictions, currents of only 0.7 m s^{-1} were expected. The aim of this research is to gain insight into the origin of these higher currents, taking into account the physical oceanography at this location.

We find that these high currents measured in August are forced by baroclinic currents. Stratification was present at a measurement ship, 32 km northeast from Gemini. In addition, satellite imagery shows Gemini to be located in a region with fronts, between warm water from the Wadden Sea and colder water from the North Sea. In fact, a tidal mixing front is formed on top of the already established saline stratification [VAN AKEN, 1986].

The origin of fresh water is found to be from sluices discharging onto the Wadden Sea. Prior to the period with high currents a pulse of fresh water is discharged onto the Wadden Sea. Followed by the lowest winds recorded in 2015, an optimal climate is formed in which fronts can travel offshore. This is supported by the satellite imagery. In addition, density-induced currents are calculated based upon the mathematical model of HEAPS [1972]. The analysis if the data suggests that density driven currents of 0.4 m s^{-1} are generated in August, which combined with the tide can give 1.2 m s^{-1} currents.

Acknowledgments

This Master Thesis has been carried out as the finalizing part of the Master of Science program Hydraulic Engineering at the Faculty of Civil Engineering and Geosciences, Delft University of Technology, The Netherlands. The project has been funded by van Oord within the framework of the Gemini offshore wind project. The research has been conducted at the office of Van Oord in Rotterdam. This unique cooperation between Delft University of Technology and Van Oord has resulted in an improved knowledge of the physical oceanography just north of the Wadden Sea.

I would like to thank my graduation committee for their supervision during the project. My expressions of gratitude go especially to Prof.dr. J.D. Pietrzak, Dr. ir. G.J. de Boer, Dr. ir. M. Verlaan and ir. S. Rijnsburger, who provided input and also guided me through the whole project. Furthermore I would like to thank A.R. Costerus for providing me with the current dataset which made this project possible. Additionally I want to show my expression of thanks to W. Kanneworff for taking the time to show me around the actual project at Eemshaven. Furthermore I would like to thank Van Oord for facilitating a place to work in a community with other M.Sc. students.

My parents, John and Anneke showed me the beauty in doing things you really like and also stimulated me during my studies en throughout my M.Sc. thesis. I would also like to thank my family-in-law for always showing interest and support. My little brothers Alexander and Laurens were also interested in my work and contributed to ideas in their own and original way. Last but definitely not least, I would like to thank my girlfriend Chantal for sharing this adventure with me. Thank you for de-stressing me so many times, coaching me and most importantly, just simply being there.

Rotterdam, June 30, 2016,

Christiaan Claessens

Contents

1

Introduction

Van Oord is the EPC-contractor for the Gemini offshore wind park (Figure 1.1), the second largest wind project in the world. In January 2015 the construction began of 150 4 MW wind turbines, which will supply a total of 600 MW of renewable energy for 785,000 households by 2017. With a value of more than EUR 1.3 billion, it is the largest contract in Van Oord's history.

During project preparations questions were raised about the maximum current velocities in the area. A metocean report made earlier by DHI was consulted [DHI WASY, 2012]. 29 years of ADCP current measurements from the nearby German measurement station, FINO1, were used to calibrate the DHI model MIKE 21 HD. This depth-averaged barotropic model can be used for any hydrostatic two-dimensional currents, for which the stratification can be neglected. Data-analysis on the numerical results show a maximum surface current of 1.2 m s^{-1} to appear during winter (January and December) with a return period once every ten years. In summer (May to September) currents of 1.0 m s^{-1} are found, also with a return period once every ten years. Since the barotropic mode is only forced by tide and wind, it produces the highest currents when storms are strongest.

By contractual requirements a TRIAXYS buoy was also placed at the project location from February to November 2015. In marked contrast to the predictions, current velocities of up to 1.2 m s^{-1} were measured in August. ROEST [2015] analyzed the data and made a tidal fit using T_TIDE. However, he did not find a correlation between the high current, wind and tidal signal. Both the DHI model and the work of ROEST [2015] only focused on the barotropic tidal and wind currents. As a follow-up, this study is being carried out to find an explanation for these large currents.

Baroclinic currents are known to dominate the southern North Sea [DE BOER, 2009; RIJNSBURGER, 2014; PIETRZAK *et al.*, 2011]. Notably, stratification is due to two large regions of freshwater influence (ROFI's); the Rhine ROFI [SIMPSON *et al.*, 1993; MCCANDLISS *et al.*, 2002; DE BOER *et al.*, 2006, 2008, 2009] and the East Anglia Plume [MCCAVE, 1987], as well as a seasonal tidal mixing front that extends across the southern North Sea in the summer [EISMA AND KALF, 1987; HILL *et al.*, 1993].

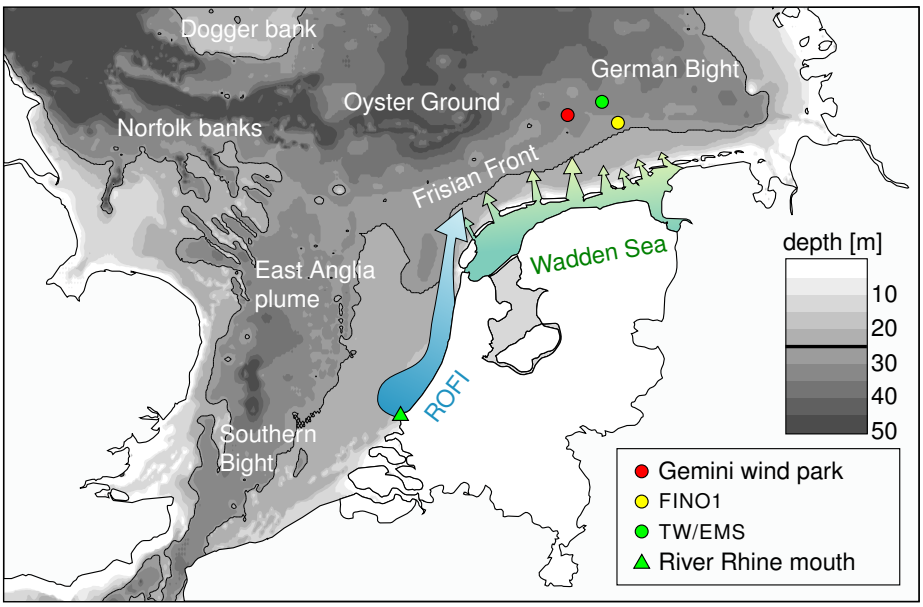

Figure 1.1: Overview map of the area. The freshwater influence from the Rhine is indicated by the large blue arrow. Notice the lighter end of the arrow, this indicates the water column becoming more well-mixed further downstream. The green area demonstrates the fresh water discharge from the Wadden Sea. Gemini is located at the red dot. Bathymetry map with area description after PIETRZAK *et al.* [2011]

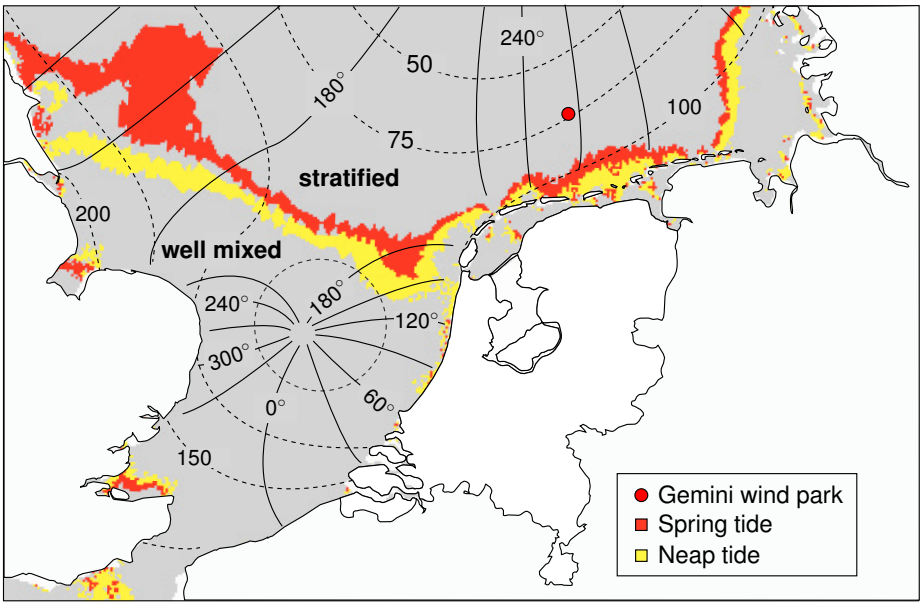

Figure 1.2: Predicted position of frontal boundaries at spring tide (red) and neap tide (yellow) [KLEPTSOVA, 2013]. Based upon the Simpson-Hunter criteria for tidal fronts only taking into account tidal mixing and solar heating. The effects of salinity differences balancing the vertical are not taken into account. The red dot marks the location of the Gemini wind park. Co-tidal lines (degrees) and co-range lines (amplitudes in cm) are from PROUDMAN AND DOODSON [1924]

The hypothesis explored in this thesis is that the baroclinic currents are the most likely cause of the large velocities in August.

1.1 Physical oceanography

The Gemini offshore wind park is located 60 km north of the Wadden Sea in North Sea (Figure 1.1). This region is dominated by tides [PROUDMAN AND DOODSON, 1924]. In the shallow southern North Sea bottom friction dissipates considerable amounts of energy [SIMPSON, 1998]. The tide comes into the North Sea from the north and south of Great Britain. Influence from the rotation of the earth deflects the water along the British coast towards the south. Then, as the channel between the UK and The Netherlands narrows, the main body of water turns along the Dutch coast towards the north. This effect is enhanced by a predominant northward flow through the Dover Straits. Combined with meteorological and buoyancy driven residual currents, the North Sea shows a strong cyclonic circulation [PRANDLE, 1978]. Buoyant water from the English coast are forced offshore by the residual current to form the East Anglia Plume [HOLT AND JAMES, 1999].

The Rhine ROFI transports large quantities of freshwater northwards along the Dutch coast, it is stratified in the vertical near the mouth of the Rotterdam Waterway. DE BOER *et al.* [2006, 2008, 2009]; RIJNSBURGER *et al.* [2016] showed that it is more well mixed over the vertical at a site 80 km downstream. It is expected that at the Gemini site the fresh water of the Rhine is well-mixed in the vertical.

There is yet another fresh water source in the more immediate vicinity of Gemini, the Wadden Sea. As it rains, the low lying land surrounding the Wadden Sea collects rain water. This has to be drained by pumping it onto higher located, man-made rivers, which can then transport the water under gravity to the IJselmeer. The excess fresh water collected in the IJselmeer is discharged onto the Wadden Sea during ebb. This water quickly becomes well-mixed because of strong tidal mixing in the shallow Wadden Sea [DURAN-MATUTE *et al.*, 2014].

SIMPSON AND HUNTER [1974] postulated that a tidal front would be found where the intensity of turbulent mixing was just enough to overcome temperature stratification from the solar radiation. PINGREE AND GRIFFITHS [1978] approached tidal fronts from the point of view of the turbulent kinetic energy rate due to tidal flow. They predicted a tidal mixing front should also form at the approximate location of the East Anglia Plume, at Flamborough Head and the Frisian Front. It separates well-mixed water in the southern Bight, from the seasonally stratified central North Sea waters. Following this technique, KLEPTSOVA [2013] estimated the tidal velocities with a numerical model for the North Sea. She calculated an index $S = \log_{10}(h/(C_d|u_s|^3 \cdot 10^4))$ and showed that in areas where $S < 1$ the waters are tidally mixed throughout the year, and where $S > 2$ the waters were stratified in summer (Figure 1.2).

Flows generated by tidal mixing fronts have been investigated using dynamical models [JAMES, 1978; GARRETT AND LODER, 1981]. They predict a frontal jet and secondary cross-frontal flow [LWIZA *et al.*, 1991], and the evolution of deep jets, associated with the presence of the seasonal thermocline [BROWN *et al.*, 1999; HILL *et al.*, 2008]. Figure 1.3 summarizes schematically the two-dimensional

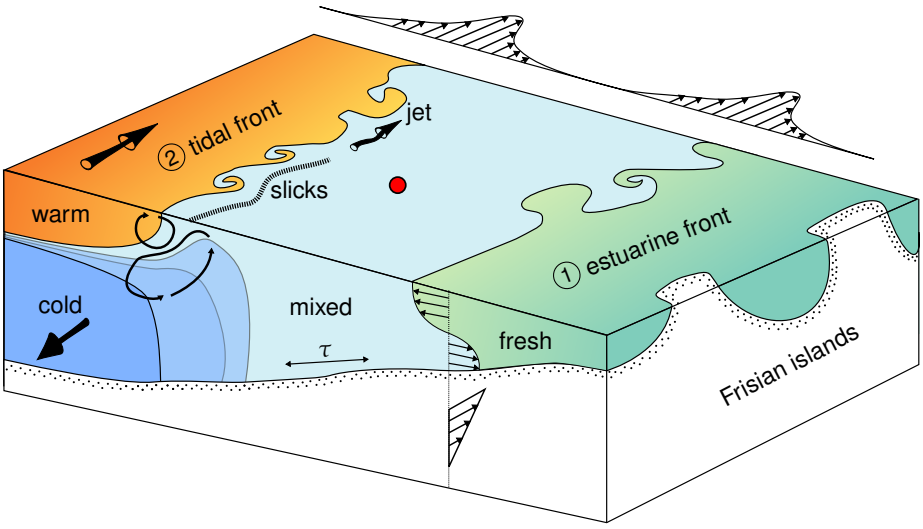

Figure 1.3: The ① estuarine front is created with fresh coastal waters. Further offshore this fresh water is tidally mixed. Even further offshore mixing is decreased conjointly, allowing solar heating to stratify the water column. This is where the ② tidal front is formed. The red dot indicates the location of Gemini, in between the two different fronts. Drawing is a combination between images from SIMPSON [1997]; HILL *et al.* [1993]; SIMPSON *et al.* [1981] and terminology from YANAGI [1987]

steady-state density driven circulation at tidal mixing fronts which arises from a combination of observations and model predictions [HILL *et al.*, 1993].

However, the model based on the Simpson-Hunter criteria cannot be correctly applied at the Dutch coast. It does not incorporate a mechanism to allow for variations in salinity and waves. Salt stratification allows the formation of a separate surface layer, initiating stratification. Turbulence is suppressed in the halocline allowing the surface layer to raise in temperature without the water column becoming vertically mixed [VAN AKEN, 1986]. Therefore the location of these tidal mixing fronts can deviate significantly under the influence of fresh water input.

In his paper, VAN AKEN [1986] used data from three cruises in 1978, 1981 and 1982 to highlight that the onset of stratification was not consistent with the Simpson-Hunter criteria. He found salt stratification which appeared to be caused by an "estuary-like" stabilizing advection of fresh coastal water in the upper layers of the water column. Based on this they concluded the Simpson-Hunter criteria failed to predict the onset of stratification in areas subject to fresh water influence. A source for these salinity fronts just north of the Wadden Sea was not found. In this thesis we will further investigate the origin of currents associated with baroclinic effects.

1.2 Methods and approach

In chapter 2 the necessary theoretical background will be presented to support in understanding the physical processes which play a role at Gemini.

The approach of this study is to first gather available measurements made at, and surrounding the Gemini location. Besides the current measurements recorded on site, salinity- and temperature measurements through the water column have been used from the TW/EMS measurement ship. Even though this ship is located 32 km northeast from Gemini, this is the closest dataset available and can still give an indication whether or not stratification is present. To provide a birds eye view of frontal activity, remotely sensed sea surface temperature measurements have also been collected. Influence from the Wadden Sea is characterized by fresh water discharged from the IJselmeer and warmer water during intensified summer heating. For this sluice data from Rijkswaterstaat is used to obtain daily freshwater discharge values. The warmer water can then be picked up from the satellite imagery. The acquisition and processing of these measurements is treated in chapter 3.

First the findings from the buoy are validated using another (smaller) ADCP current dataset from the cable-laying ship Nexus. Then the measured currents are analyzed using an EOF analysis to see what the principal components of the signal are. Followed by a tidal analysis using T_TIDE the barotropic currents can be separated from the baroclinic. This is further confirmed by comparing them with the barotropic model results of the DCSMv6-ZUNOv4-KF model used by Rijkswaterstaat. Lastly five Delft3D simulations are made. A swimming pool with five different depths is heated using meteorological measurements from the KNMI. This way the heating behavior can be compared with that of the sea surface temperature measured at Gemini. A description of these methods can also be found in chapter 3, after which the results are described in chapter 4.

Everything comes together in the discussion (chapter 5). The conclusions and recommendations are given in chapter 6.

2

Theoretical background

This chapter treats the theoretical background needed for understanding density driven flow in frontal systems. First an overview of different types of fronts will be given. Then the two most important fronts for this thesis are described in more detail. Lastly influence from wind and tide is presented.

2.1 Fronts

Density-induced current velocities are greatest at the place where two distinct water masses with two different densities meet, called a front. There are many kinds of fronts in the sea and they are classified into three types according to the place where they are formed: coastal sea-, continental shelf sea- and open sea fronts [YANAGI, 1987]. Only coastal sea fronts are treated here since the shallow North Sea is part of the European continental shelf. Within this category YANAGI [1987] proposed four types of fronts; the estuarine, tidal, thermohaline and thermal effluent front (Figure 2.1). A thermohaline front is generated during the winter and a thermal effluent front is similar to an estuarine front as it is formed by a power plant. This leaves the ① estuarine and ② tidal front to possibly occur in the southern North Sea during August (Figure 1.3).

Estuarine fronts are formed in the region close to the coast where riverine water meets the salty sea water. The lighter fresh water sits on top the more dense sea water, stratifying the water column. Here the flow is determined by a balance between internal friction and pressure. When saline stratification reaches further offshore, the rotation of the earth starts to effect baroclinic flow. A case study done by HEAPS [1972] in the Liverpool Bay area found the 3D currents to follow a balance between internal friction, pressure and Coriolis. A mathematical model based on these forces was formulated. In general, the observations indicate the presence of a bottom drift to the coast, and an inclined offshore surface drift (to the right); both are confirmed by the theory. Observations by DIETRICH [1953] off Texel island have indicated the presence there of residual currents directed similarly to those in the Liverpool Bay. With a bottom drift towards the coast and an essentially north-going surface drift. It seems likely the mechanism for density currents proposed by HEAPS [1972] may also be applicable to the belt of coastal sea off Texel Island.

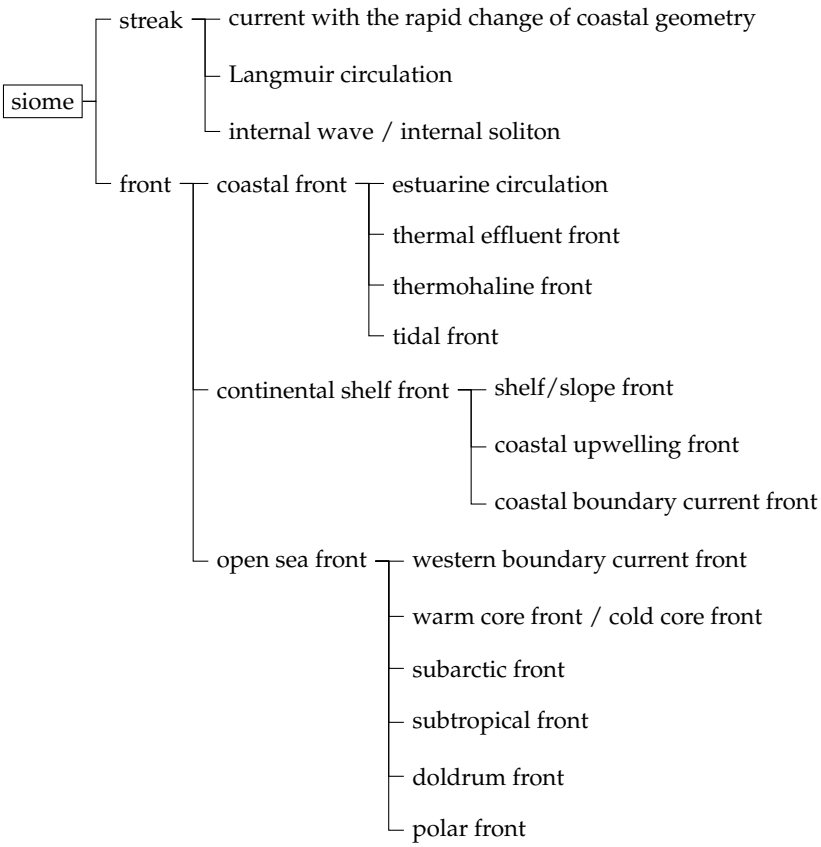

Figure 2.1: Classification of siome after YANAGI [1987]

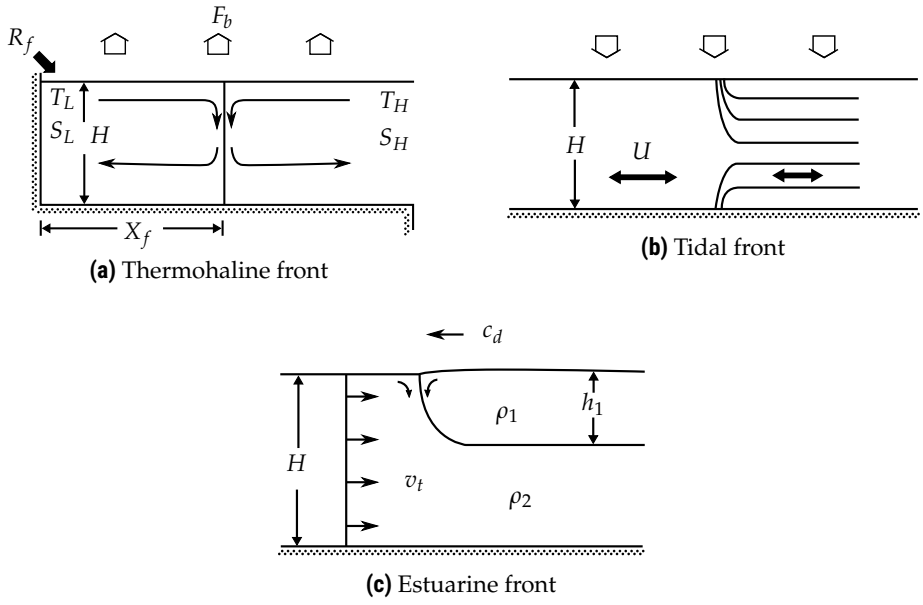

(a) Thermohaline front

(b) Tidal front

(c) Estuarine front

Figure 2.2: Coastal fronts after YANAGI [1987]

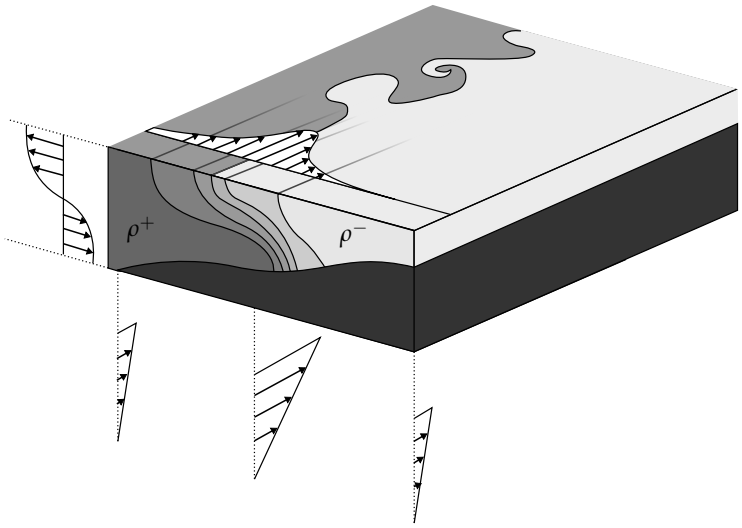

Figure 2.3: Concept by HEAPS [1972]. Less dense water (ρ^-) from the coast wants to flow over the denser water from the sea (ρ^+). Under the influence of friction and Coriolis a 3D current pattern is created

The tide comes into the North Sea from the north and south of Great Britain. Influence from the rotation of the earth deflects the water along the British coast towards the south. Then, as the channel between the UK and The Netherlands narrows, the main body of water turns along the Dutch coast towards the north. The periodic nature of the tide makes the flow pattern reverse during the ebb phase.

Tidal mixing is strongest close to the coast. Further offshore the influence from the fresh water becomes less, permitting the tide to vertically mix the water column. However, when moving even further offshore, tidal mixing becomes less as the water depth increases. At some point heating from the sun is allowed to heat to top surface of the seawater without it becoming mixed. This region is called the tidal front or tidal mixing front SIMPSON AND HUNTER [1974].

2.1.1 Heaps

In Physical Oceanography the concept of Thermal wind is often used. Basically a balance between a baroclinic pressure gradient and the rotation of the earth is made to explain the current pattern. However, because the area around Gemini is a shallow frictional sea, there is a significant influence from bottom friction. To account for this deviation HEAPS [1972] theorized an analytical solution for the thermal wind balance in combination with friction.

The result of the balance by HEAPS [1972] is a 3D current structure induced by density differences which take place against the alternating background of the dominant tidal streams. An infinitely long, straight coast with no alongshore geometry gradients is considered. The convective terms in the acceleration relative to the Earth have been neglected. Furthermore his steady state solution

takes no account of the internal stresses acting in a horizontal plane. In his paper a practical case was studied: the Liverpool Bay area. At the coast there is freshwater runoff and further out to sea the water gets more saline. This area appears for the most part to be nearly vertically homogeneous throughout the whole year.

Results of his analytical solution agreed with measurements taken in the area. As turns out, there is a landward current at the sea bed while the sea surface current is inclined (in the horizontal) at an obtuse angle to those at the bottom. Apparently when there is vertical stratification and the balance between tidal energy and fresh water runoff is just right; there is an onshore density driven bottom current. Following continuity the vertical current profile is twisted as such that the sea surface current makes an angle of around 120 degrees with the bottom current. Both internal friction and the Earth's rotation are significant factors determining the density-current structure. This particular case can be seen as an intermediate type between those in an estuary and in the deep sea. In an estuary the frictional effects dominate while in the deep sea the geostrophic effects dominate.

His analytical solution is given below,

$$\begin{aligned} u &= \frac{gH}{f\rho}\frac{\partial \rho}{\partial x}(XQ - YP) + \frac{fq}{kS}(MP - LQ) \\ v &= \frac{gH}{f\rho}\frac{\partial \rho}{\partial x}(XP + YQ + \Lambda + \eta) + \frac{fq}{kS}(1 - LP - MQ) \end{aligned} \tag{2.1}$$

$$\begin{gathered} Z = z + \xi, \quad H = h + \xi, \quad \eta = Z/H, \\ a = \pi H/D, \quad a_1 = a(1-\eta), \quad a_2 = a\eta, \quad b = kH/N, \\ C = a(\sinh a \cos a - \cosh a \sin a) + b \cosh a \cos a, \\ E = a(\sinh a \cos a + \cosh a \sin a) + b \sinh a \sin a, \\ L = b \cosh a_2 \cos a_2, \quad M = b \sinh a_2 \sin a_2, \\ P = C/(C^2 + E^2), \quad Q = E/(C^2 + E^2), \\ R = P \cosh a \cos a + Q \sinh a \sin a, \quad S = 1 - Rb, \\ \Lambda = (R - P - S)/S, \quad \lambda = 1 + b + b\Lambda, \\ X = \cosh a_1 \cos a_1 + (b/2a)(\sinh a_1 \cos a_1 + \cosh a_1 \sin a_1) - \lambda \cosh a_2 \cos a_2 \\ Y = \sinh a_1 \sin a_1 + (b/2a)(\cosh a_1 \sin a_1 - \sinh a_1 \cos a_1) - \lambda \sinh a_2 \sin a_2 \end{gathered} \tag{2.2}$$

The basic parameters of the list are η, a, b, these being non-dimensional and functions of Z, H, D, N, k where Z is depth below the sea surface and H the total depth from surface to bottom. The input values for the evaluation of u and v in Equation 2.1 may therefor be taken as η, H, N, k, f, g, $(\partial\rho/\partial x)/\rho$, q. In the expressions for u and v the first term clearly represents the effect of density gradient and the second the influence of coastal discharge. His result for the Liverpool Bay are is depicted in Figure 2.4.

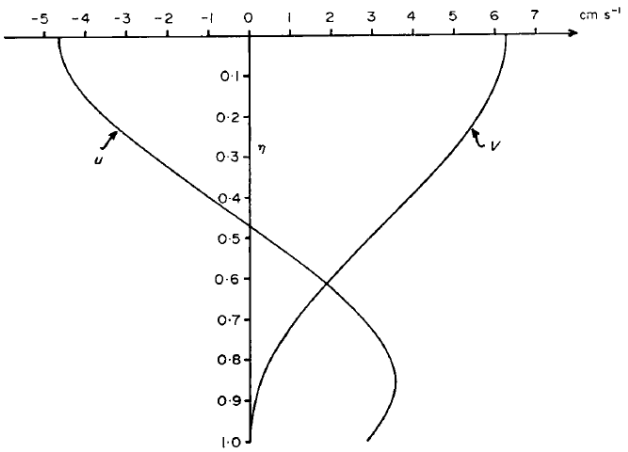

Figure 2.4: Vertical profiles of the current components u and v at position P, 12 nautical miles from the coast

2.1.2 Simpson and Hunter

The transition between a stratified and unstratified regime is controlled by the level of tidal mixing. A simple case is discussed; water with an amount of buoyancy is considered. In this case the buoyancy is established by an amount of heat q into the surface of the water column of depth h and initial density ρ. This heat input produces a density change $\Delta\rho$ in a thin surface layer Δh. To mix the column vertically to a uniform density ρ' in a depth h' the potential energy must be increased by an amount $V_2 - V_1$ where,

$$V_1 = \frac{1}{2}\rho g h^2 - \Delta\rho\Delta h g h + Ph \tag{2.3}$$

$$V_2 = \frac{1}{2}\rho' g h'^2 + Ph' \tag{2.4}$$

With V_1 the potential energy before mixing, V_2 the potential energy after mixing and P the atmospheric pressure. Assuming the density is a linear function of temperature and neglecting salinity as a source of buoyancy input it is easily shown that $h = h'$. For a rate of heat input Q the demand for potential energy to maintain mixing would be,

$$\frac{\mathrm{d}(V_1 - V_2)}{\mathrm{d}t} = \frac{\alpha Q g h}{2c} \tag{2.5}$$

with α the linear expansion coefficient and c the specific heat. On the other hand energy is lost from the tidal motion at a mean rate of,

$$\frac{\mathrm{d}E}{\mathrm{d}t} = \overline{\tau_b u_b} = k\rho|\overline{u_b^3}| = \frac{4k\rho u_0^3}{3\pi} \tag{2.6}$$

where u_b and τ_b are the velocity and shear stress respectively, near the bottom, and u_0 is the amplitude of u_b. k is a constant in the assumed quadratic friction

law. A fraction ϵ of this kinetic energy is considered to be available for increasing the potential energy of the water column so that at transition there is a balance defined by

$$\frac{\mathrm{d}(V_1 - V_2)}{\mathrm{d}t} = \frac{\mathrm{d}E}{\mathrm{d}t} \qquad \rightarrow \qquad \frac{h}{u_0^3} = \frac{8c\rho k\epsilon}{3\pi\alpha g Q} \tag{2.7}$$

If the area and time of interest are limited, Q can be regarded as constant. Then, providing ϵ and k are also constants, the locus of the front should be defined by a critical value of h/u^3. This is the famous SIMPSON AND HUNTER [1974] criterion for determining the location of fronts.

2.2 Tide

The tides are generated by the gravitational pull of the moon and sun on the earth. The rise and fall of the water level near the shore causes water to move horizontally, creating currents. The periodic rotation of the earth and the movement of the sun and moon causes these currents to be predictable.

The tide in the North Sea is semi-diurnal. This means twice every day the water level rises (flood) and falls (ebb). The amplitude of this rise and fall is maximum during spring tide, when moon and sun strengthen each other, and is minimum during neap tide, when moon and sun undermine each other.

PRANDLE [1982] examines the accuracy to which the vertical structure of tidal currents can be predicted. Tidal vectors cover a horizontal elliptical path during a tidal cycle. To observe the behavior of these ellipses he decomposed this signal into two counter rotating vectors (R^+ and R^-). Solving the momentum equations on a regular Cartesian grid is impossible, but through the decoupling into phase vectors it is possible.

For the research in this thesis the maximum amplitude of the tidal velocity is of importance. Usually, tidal information is obtained from tide and tidal current tables, or from computer models. For example the Bundesamt für Seeschifffahrt und Hydrographie (BSH) in Germany predicts hourly tidal velocities with their Operational modelling system.

2.2.1 Tidal straining

As the river Rhine releases large quantities of fresh water into the North Sea, the lighter riverine water sits on top the more dense sea water. As a result, the water column is stratified. The outflow of this riverine water is deflected to the right by the earth's rotation. Typically a bulge region is formed near the river mouth followed by a narrow downstream coastal current. Stratification is most intense near the mouth of Rhine at 3 to 5 km from the shoreline [DE RUIJTER *et al.*, 1997]. Closer to the shore wind, waves and the tide have a bigger impact, mixing the water column. This results in a typical river plume; a ROFI, which is short for Region of Fresh Water Influence [HORNER-DEVINE *et al.*, 2015, Fig. 5].

The tide is of significant importance on the appearance and long-term fate of the Rhine ROFI. Approximately twice a month the spring-neap cycle switches

the ROFI between mixed and stratified conditions. Higher currents impelled by spring tide are enough to force the water in a vertically well-mixed state. The reduced neap tide mixing levels on the other hand allow for the ROFI to stratify. Wind mixing can further effects these basic states [SIMPSON *et al.*, 1993]. The main time scale of the system is set by the spring-neap mixing cycle, with irregular components due to wind mixing [DE BOER, 2009; VAN WIECHEN, 2011].

Periodic stratification can also develop on a shorter time scale, the semi-diurnal tidal cycle. Over this cycle the Rhine ROFI can change from a vertically -stratified state to a well mixed one, or vice versa. This process known as tidal straining is clearly described by SIMPSON *et al.* [1990]. To understand how this works, the tide needs to be considered as a propagating Kelvin wave. With maximum flood velocities at HW (High Water) and maximum ebb velocities at LW (Low Water). This assumption is justified when the small phase shift due to bottom friction is neglected. Furthermore, the main tidal current is alongshore whereas the main density gradient is cross shore. This can be seen in Figure 2.5 at $t = 0$. The water column is vertically well-mixed, though a horizontal density gradient is present in the cross-shore direction. During slack water these stratified conditions cause the anti-cyclonic surface currents to be directed offshore instead of dropping to zero. Simultaneously the bottom currents advect more dense water onshore. This can be seen in the current profile at $t = T/4$. At HW the plume is maximally stratified ($t = T/2$) when the cross shore currents is reduced to zero to reverse. From HW to LW the cross shore currents work exactly the other way around, effectively transporting the upper- and bottom layer back to the original well-mixed position at $t = T$ [DE BOER, 2009].

DE RUIJTER *et al.* [1997] had a closer look at the evolution of stratification further downstream from the Rhine mouth. A peak discharge from the Rhine of 6000 m^3 s^{-3} was followed in January 28, 1986. Knowing the vertical mixing rates and using the potential energy anomaly, an estimate can be obtained for the time it takes for a pulse of fresh water to be vertically well mixed. Without the influence of large winds, it turns out the water column is vertically well mixed within two weeks, which is equivalent of $\pm$80 km. Furthermore an alongshore salinity transect of 100 km through the axis of the Rhine ROFI at $\pm$4 km from the shore was taken on January 28, 1986. The freshwater pulse is clearly visible. Also salinity values increase significantly once the ROFI flows downstream. This is confirmed by the work of RIJNSBURGER *et al.* [2016], in which two cross shore salinity transects between the cities of Petten and IJmuiden have been investigated. It turns out small salinity differences are present within these transects, in accordance with the tidal straining theory.

2.3 Wind

To get a clear notion of the influence of the earth's rotation, and also of the friction in the water, consider the simplest possible case of a wind-current. A large ocean of uniform depth without differences of density is taken. Suppose the sea surface is impelled by a steady and uniform wind equal in strength and direction over the whole region. These circumstances have lasted so long the motion has become practically stationary. According to EKMAN [1905] it then follows by symmetry that the motion will consist of a gliding of the water

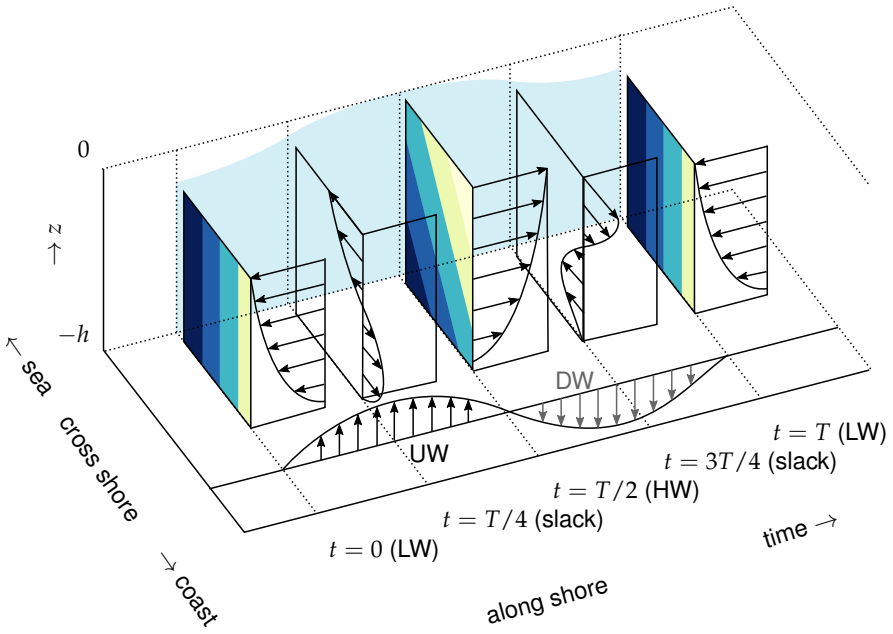

Figure 2.5: The concept of tidal straining. During slack water the anti-cyclonic surface layers are offshore directed instead of of dropping to zero, forming a stratified water column. During slack water after the flood phase the process is conversed, de-stratifying the water column. Figure is redrawn from [DE BOER, 2009, Figure 2.23]

layers over one another much as a bundle of thin boards might be imagined; the direction and velocity of the motion being uniform within each horizontal layer.

The result is a simplification of the equations of motion. Only a balance between Coriolis and friction remains. To continue with the terminology of EKMAN [1905];

$$\frac{\partial^2 u}{\partial z^2} + 2a^2 v = 0; \qquad \frac{\partial^2 v}{\partial z^2} - 2a^2 u = 0, \tag{2.8}$$

With the notation,

$$a = \pm\sqrt{\frac{q\omega \sin\phi}{\mu}} \tag{2.9}$$

With q the density of the fluid, ω the angular velocity of the earth ($7.29 \cdot 10^{-5}$), ϕ the latitude and μ the coefficient of viscosity.

The general solution consists of two equations with four arbitrary constants. To get a physical solution we must assume ϕ to be positive, which means the solutions are applicable in the northern hemisphere. Furthermore two boundary conditions must be applied. The solution takes the simplest form if the ocean is assumed to be infinitely deep. The second boundary condition is an assumption that the tangential pressure of the wind on the sea surface is T, and is directed

along the positive y-axis. If further V_0 is defined as the absolute velocity of the water at the surface, the solution becomes;

$$\begin{aligned} u &= V_0 e^{-az} \cos(45^\circ - az) \\ v &= V_0 e^{-az} \sin(45^\circ - az) \\ V_0 &= \frac{T}{\mu a \sqrt{2}} = \frac{T}{\sqrt{2\mu q \omega \sin\phi}} \end{aligned} \tag{2.10}$$

Equation 2.10 shows that in the northern hemisphere the drift-current at the very surface will be directed 45° to the right of the velocity of the wind (relative to the water). In the southern hemisphere this is vice versa. This angle further increases uniformly with the depth, four right angles for each time the depth increases by $2\pi/a$. At the same time the velocity of the water decreases with the depth to $e^{-2\pi} = 1/535^{\text{th}}$ part for each time its direction rotates four right angles. This structure is called the Ekman spiral.

The research done by WEBER [1983] suggests a rule of thumb for transforming wind velocities to surface currents speeds. The assumption is made of a fully developed sea and the eddy viscosity is taken to be proportional to the friction velocity times a characteristic depth. Hence the total current (Ekman plus wave-induced current) can be expressed as functions of the wind speed. The results show that the magnitude of the total surface current lies between 3.1 and 3.4% of the wind speed at 10 m height for winds between 5 and 30 m s^{-1}.

3

Methodology

A number of datasets are available with which the origin of high current velocities at the Gemini offshore wind park are investigated. In this chapter these datasets and analysis techniques are presented. In section 3.1 the measurement data are treated. The depth averaged current velocities acquired from the DCSMv6-ZUNOv4-KF model are presented in section 3.2. Tools for analyzing both measured and modeled data are treated in section 3.3. The meteorological data is also used to setup a small scale model to investigate the heating behavior of a water body using Delft3D. The setup of this model is presented in section 3.4.

3.1 Measurement data

In this section the current velocity measurements will be presented. After this the meteorological data provided by the KNMI will be treated. Then temperature and salinity measurements made over depth are presented. Fresh water sluice discharge in the Wadden Sea provided by the Dutch Waterboards will be discussed. And finally the remotely sensed sea surface temperature is presented. A summary of the location and measured parameters is displayed in Figure 3.1 and Table 3.1.

3.1.1 Current velocities

As part of the Gemini project, Van Oord placed a TRIAXYS and Wave Rider buoy at the wind farm location, see ① in Figure 3.1. The Directional Waverider MkIII buoy measures wave -height, -direction and water surface temperature. The TRIAXYS Wave & Current Buoy also measures wave -height, -direction and water surface temperature. This buoy is also equipped with a current profiler (ADCP), which measures current speed and direction in 18 depths over the water column.

An ADCP follows the premise of the Doppler effect. It emits a series of high-frequency pulses of sound that bounce off of moving particles in the water. If the particle is moving away from the instrument, the return signal is at a lower frequency. If the particle is moving toward the instrument, the return signal is at a higher frequency. Because the particles move at the same speed as the

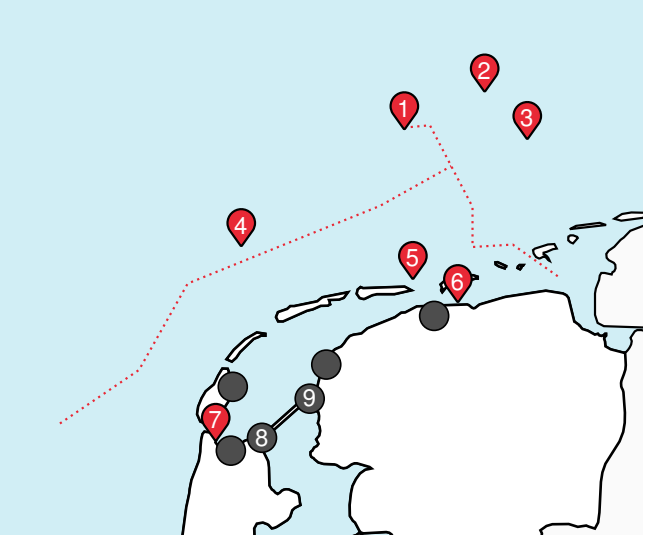

Figure 3.1: Measurement locations, for description see Tab.3.1.

Table 3.1: Legend for Figure 3.1

	Location	Measurement
1	Gemini	Current velocities, water temperature and wave height
2	TW/EMS	Water temperature and salinity over depth
3	FINO1	Water temperature and salinity over depth
4	KNMI 207-L9-FF-1	Wind speed and direction, cloudiness, air temperature and relative humidity
5	KNMI 208-AWG-1	Wind speed and direction, cloudiness, air temperature and relative humidity
6	KNMI 277-Lauwersoog	Wind speed and direction, global radiation, air temperature and relative humidity
7	KNMI 235-De Kooy	Wind speed and direction, global radiation, cloudiness, air temperature and relative humidity
8	Den Oever	Sluice fresh water discharge
9	Kornwederzand	Sluice fresh water discharge
	Dotted red line	The path of Van Oord's Nexus ship for when the ADCP was turned on
	Grey circles	Location of sluices which discharge fresh water in de Wadden Sea

water that carries them, the speed of the water's current can be determined. The systems electronics integrates Doppler velocity with temperature, pressure, tilt and compass sensors.

The ADCP measurements are made in the water column with steps of 2 m, see Figure 3.7. This device does not know where the seabed is, the signal will be reflected by the bottom of the sea. This would make it seem as though there is a current velocity below the bottom, but in fact it is the current velocity above the bed. The reflection of the signal can help to identify the location of the seabed as it displays symmetry.

Both buoys can accurately measure wave height differences up to 0.01 m and wave directions up to 3 degrees. The accuracy of temperature measurements is ± 0.5 °C for the TRIAXYS buoy compared to ± 0.1 °C for the Waverider. The absolute current velocity measurements made by the TRIAXYS is accurate up to ± 10 cm s^{-1}. Measurements from both buoys are made every hour and are then transmitted with an Iridium Internet module to an OMC-database.

The current time series start on 16 February 2015 and come to an abrupt stop after a storm event on the night of 28 November 2015. The GPS of the TRIAXYS buoy shows a two week journey to Denmark, after which a truck transported the adrift buoy to the Moerdijk yard. Thus the TRIAXYS buoy has measured data over a period of 10 months. The Waverider buoy is still up and running at the time of writing this thesis.

The obtained current dataset does not show any outliers. The data is however not continuous. Due to communication errors through the iridium connection, 24 missing data points are encountered. Not only current measurements, but also the time vector is discontinuous. A new and complete time vector is constructed by filling the missing current values as a NaN[1].

The current velocities measured by the TRIAXYS buoy are validated by comparing them to a second dataset. On board Van Oord's cable laying ship, the Nexus, an ADCP is installed. Measurements have been made from 27 May to 2 November. These measurements are discontinuous in both time and space; 12 weeks are missing and some measurements are made far away from Gemini. The path taken by the Nexus is visible as the dotted red line in Figure 3.1

With Matlab a script is written which checks if the Nexus is within 150 m of the TRIAXYS buoy. Only then the Nexus ADCP data will be plotted. A small phase shift was visible between both datasets, this appeared to be caused by the different time zones for which the ADCP's measure. A time shift has been applied of 2 hours to the Nexus ADCP current time series. After these operations an effective measuring period is realized for the 3-4 July, 6-11 August, 30-31 August, 9-21 September, 2-10 October, 17-21 October and 26 October to 3 November.

3.1.2 Meteorology

To predict weather and climate the Royal Dutch Meteorological Institute (KNMI) uses different kind of measurement devices. To find a relation with the mea-

[1]Not a Number, used in computing to represent an undefined or unrepresented value

sured current velocities, five meteorological parameters have been collected for the year of 2015. The wind direction and velocity, global radiation, cloudiness, relative humidity and air temperature. For each of these parameters the measurement instrument will be presented and how the data is recorded and processed by the measurement institute. Then the location of the measurement is treated, how the dataset is obtained and processed. More information can be found in KNMI [2006].

Since 1960 the KNMI measures the wind velocity and direction with a cup-anemometer, see Figure 3.2. The World Meteorological Organization (WMO) prescribes measurements should be made on a 10 m high mast surrounded by open terrain. Wind direction is measured with an accuracy of ± 5 degrees and wind velocity with ± 0.5 ms^{-1}. The average wind velocity is determined for periods of ten minutes and recorded in ms^{-1}. Weather reports containing present-day wind measurements are preliminary. Afterwards all data is verified, validated and sometimes corrected. For climate statistics and storm analysis the hourly averaged wind data is used.

At the Gemini project location no meteorological measurements are made, though in the near surroundings the KNMI has measurement stations available. In Figure 3.1 the location of these stations is indicated with ④, ⑤, and ⑥. This data is available through the KNMI database from 2001 to the present[2]. The data forms a complete time series, so no further processing is done.

A pyranometer measures the total shortwave radiation (global radiation) of the sun. This is made up of the direct- and diffuse radiation. To form a complete dataset the pyranometer has to function in all weather conditions. Therefore the measuring surface is protected against moisture and precipitation by one or two halved glass spheres, see Figure 3.3. Global radiation is normally measured in Jm^{-2} during an hour. Because this unit results in huge numbers the KNMI uses Jcm^{-2} and stores it as hourly averaged values. The sensitivity of the instruments used by the KNMI is around 20 Jcm^{-2}.

Only the land-based measurement stations in Figure 3.1, ⑥ and ⑦ provide global radiation measurements. These can be downloaded from the KNMI database for the period of 1991 up to and including the present[3].

Global radiation has been used in this thesis as a meteorological forcing in a Delft3D model. This model requires the standard unit for irradiance (Wm^{-2}) instead of the energy flow unit (Jcm^{-2}) over the course of an hour used by the KNMI. For this reason the values are transformed from Jcm^{-2} to Wm^{-2} as follows:

$$1\frac{\text{J}}{\text{cm}^2} \text{ during 1 hour} = 1\frac{\text{W}}{10^{-4}\text{m}^2} \cdot 3600 \approx 2.78\frac{\text{W}}{\text{m}^2} \tag{3.1}$$

No further processing has been done with the global radiation data since both datasets form a complete and continuous time series.

[2]KNMI database for hourly averaged data from North Sea stations:`https://www.knmi.nl/nederland-nu/klimatologie/uurgegevens_Noordzee`

[3]KNMI database for hourly averaged data from the land-based stations: `https://www.knmi.nl/nederland-nu/klimatologie/uurgegevens`

Figure 3.2: Cup-anemometer (photo: KNMI website)

Figure 3.3: Pyranometer (photo: Ronald van de Vate)

Figure 3.4: Temperature measuringneedle (photo: KNMI [2006])

Figure 3.5: LD40 cloud height meter (photo: KNMI [2006])

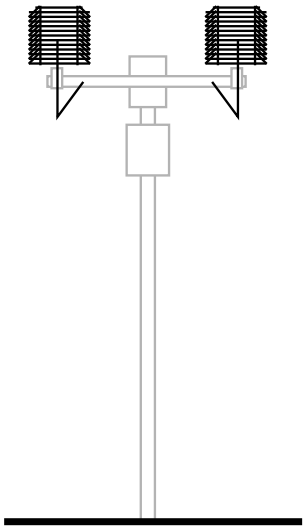

Figure 3.6: (Left) the Relative humidity, and (Right) the air temperature is measured. Both use a measurement needle as seen in Figure 3.4

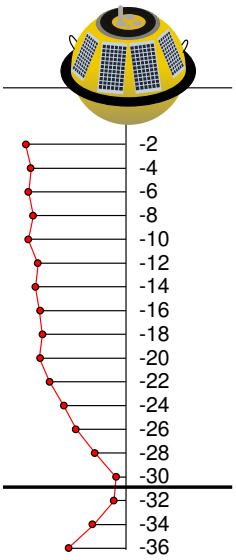

Figure 3.7: ADCP current measurement locations in the water column. A clear reflection of the signal is seen because of the seabed

Clouds are a collection of very small water droplets or ice crystals situated above the ground surface. The maximal diameter for these liquid particles is around 200 micron (0.2 mm). A bigger size leads to flocculation which results in rain or drizzle. The degree of cloud cover is calculated in octants by the LARSSON AND ESBJÖRN [1955] cloud algorithm. An octant is a number from 0 to 8, for which 0 means no clouds, and 8 dense cloud cover. To calculate the cover the LD40 cloud height meter is used by the KNMI. The sensor uses the LIDAR principle, see Figure 3.5 for the actual measuring device. The accuracy of the measurements is one octant.

Measurement location ④, ⑤ and ⑦ collect cloud cover data during the year of 2015, see Figure 3.1. Location ⑥ has no LD40 cloud height meter. The measurements are available for the year of 2001 up to and including the present. Within the datasets values of 9 are present. Since octants only contain eight values, number 9 indicates a dummy variable used when the sky is invisible due to mist or other phenomena. Cloud cover also is a parameter used in the Delft3D simulation. Since Delft3D only accepts cloud cover in percentages, the octant values are transformed to a percentage based value. This is easily done by multiplying the octants with 12.5. No further processing has been done since all three datasets form a complete and continuous time series.

The air temperature is measured in °C at 1.5 m above the earth's surface. A platinum resistance element is used at the top of a measurement needle, see Figure 3.4. A high resistance (500 Ω) is chosen to fulfill the accuracy of 0.1 °C. The measurement needle is covered by a meteorological shield to protect against radiation.

All four KNMI measurement stations from Figure 3.1 record the air temperature. Measurements are available for the year of 2001 up to and including the present. The data is stored in 0.1 °C. This has been transformed to the whole unit °C by multiplying by 10. All four datasets are complete and continuous, no further processing have been done.

KNMI uses the Vaisala capacitive relative humidity sensor to measure the relative humidity. This hygrometer looks just like the measurement needle used to measure the air temperature in Figure 3.4. Both the temperature and the relative humidity are protected by a meteorological shield and placed together on the same installation, see Figure 3.6.

Technically the relative humidity is calculated from the absolute pressure (e), equilibrium vapor pressure (e_s) and the temperature (T) using:

$$\text{Relative Humidity} = \frac{e}{e_s(T)} 100\% \tag{3.2}$$

The resulting measurement is recorded as a percentage. Satisfying the WMO guidelines, the accuracy of the relative humidity is less then 3%. Just like the temperature measurements all four KNMI measurement stations from Figure 3.1 record the relative humidity. Measurements are available for the year of 2001 up to and including the present. The four datasets are complete and continuous. Every hour the average relative humidity is recorded, no further processing has been done.

3.1.3 Salinity and Water temperature

The sea surface temperature is measured by both buoys at the project location. There are however in the near surroundings two measurement locations which measure both the water temperature and salinity through the water column, FINO1 and TW/EMS.

FINO1 is a research platform managed by the Kiel University of Applied Sciences. Located in the North Sea at location ③ in Figure 3.1, this platform is used for comprehensive physical, hydrological, chemical and biological research. Within the center of the FINO1 platform jacket a chain of instruments is installed to measure temperature and salinity in several depth layers. Both salinity (conductivity) and temperature are measured with SBE37 Microcats at a depth of 6 and 25 meter. Within the SBE37, the internal field conductivity cell sensor measures salinity with a resolution of 0.0001 S m^{-1}. Temperature is measured with a thermistor sensor at an accuracy of ± 0.002 °C. At the depths of 3, 10, 15, 20 and 26 meter thermistor sensors from Sea and Sun (Model T40) are used to measure the water temperature. Salinity measurements are thus not made at these depths. The accuracy for this type of sensor is ± 0.005 °C. See Figure 3.8 for a sketch.

Both salinity and water temperature measurements are freely available through the EMODNET database assembled by the German National Oceanographic Center[4]. For the year of 2015 data is missing from January up to and including April. Due to physical damage and/or communication problems these datasets can be interrupted several times.

TW/EMS is a radioactivity monitoring station located at number ② in Figure 3.1. Within the framework of the Strahlenschutzvorsorgegesetz (StrVG - Act on the Precautionary Protection of the Population against Radiation), the BSH routinely monitors radioactivity in the North Sea and Baltic Sea including the coastal waters. Besides radioactivity this monitoring station also measures salinity and temperature over different layers through the water column. In Figure 3.9 the location of the radioactivity, salinity and temperature measurements are given. The exact same sensors are used for measuring both temperature and salinity as for the FINO1 measurement station.

Just like the FINO1 data, salinity and temperature measurements are freely available through the EMODNET database. For the TW/EMS data is missing in March and November of 2015. Both datasets did not need any processing. The downloaded datasets from both FINO1 and TW/EMS could readily be used.

3.1.4 Sluice fresh water discharge

The Wadden Sea receives fresh water from rain, and sluices which discharge on to it. The impact from rain is very little compared to the amount sluices discharge. This fresh water is important because of the density differences induced by it. In this section the obtained sluice discharges are presented.

A total of twelve sluices discharge fresh water onto the Wadden Sea. For all twelve sluices daily averaged discharges have been acquired for the year of 2015.

[4] FINO1 time series available through the EMODNET database: `http://www.emodnet-physics.eu/Map/platinfo/PIROOSDownload.aspx?PlatformID=8557`

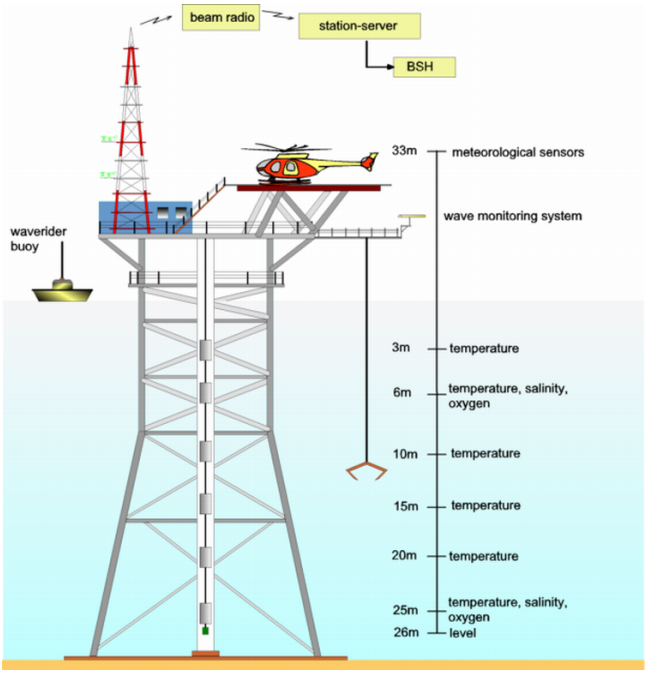

Figure 3.8: FINO1 research platform. In the center of the jacket a chain of instruments is installed to measure temperature and salinty in several depth layers. ©Federal Maritime and Hydrographic Agency of Germany

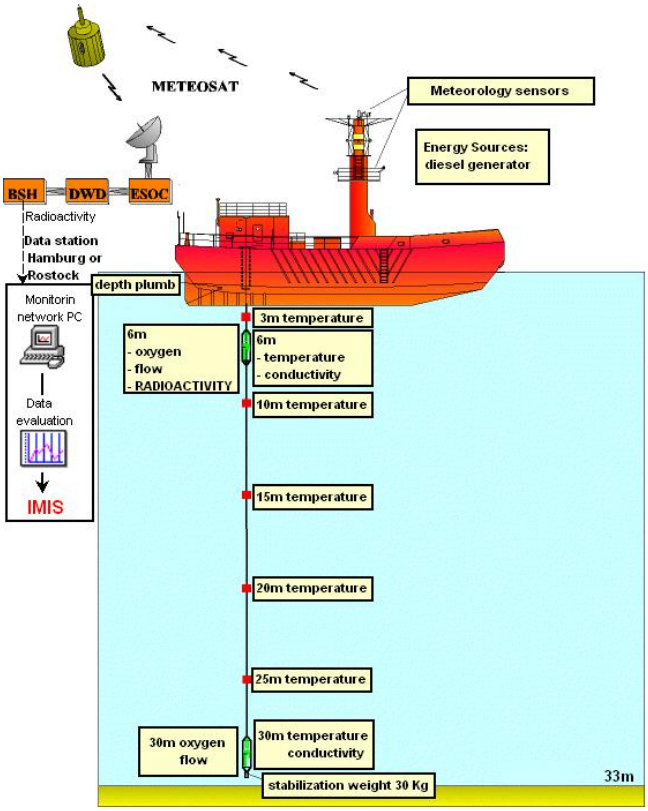

Figure 3.9: Measurement ship TW/EMS. A line with multiple CTDs is used to measure temperature and salinity through depth. ©2016 Bundesamt fr Seeschifffahrt und Hydrographie

Only fresh water is discharged onto the Wadden Sea. Salt water is discharged onto the IJsselmeer to stimulate fish migration, the sluices open a little bit, after which the salt water is pumped back into the Wadden Sea with a salt water discharge system.

Table 3.2 and Figure 3.10 give the location and yearly averaged discharge of all twelve sluices. Den Oever and Kornwederzand contribute to 87% of all fresh water discharged into the Wadden Sea. For this reason only those two sluices are displayed on the general overview map of Figure 3.1.

For the Den Oever and Kornwederzand sluices data is collected from Rijkswaterstaat. Together both sluices discharge freshwater over a length of 300 meter into the Wadden Sea. Rijkswaterstaat prescribes water is only discharged when the water level difference between the IJsselmeer and Wadden Sea is 10 cm. The 25 lock boxes of 12 meter length each open, from this moment discharge is calculated by measuring the water level slope and using calibrated resistance parameters.

The accuracy of the resulting daily averaged discharges is quite poor. Rijkswaterstaat uses a 10 - 20% accuracy on these calculated values. This has to do with the crude calculation method and the big influence the wind can have.

Rijkswaterstaat provided the discharge data for the Den Oever and Kornwederzand sluices. Sluices 4, 5, and 7 to 12 (see Figure 3.10) are managed by the Dutch Waterboard[5] Hollands Noorderkwartier. Sluice 6 is managed by Dutch Waterboard Waterschap Friesland and sluice 3 by Dutch Waterboard Noorderzijlvest. All the Waterboards and Rijkswaterstaat provided the daily averaged discharges for whole 2015. This data is complete and continuous. This data has not been further processed.

3.1.5 Remote sensing

Remote sensing has become one of the most effective means of assessing sea surface temperature (SST). The radiation detected by satellite sensors is determined by the temperature of the upper 1 mm of the ocean surface. Although there is mixing in the upper portion of the water column, these values may not accurately represent the true temperature of water volume at the upper meter of the ocean. Nonetheless, estimates of SST temperature based on observations from satellite sensors provide some of the most valuable and widely used sources of SST data. A given area may be viewed several times a day, collecting data at an intensity that would be infeasible using other methods [CAMPBELL AND WYNNE, 2011].

A satellite can orbit the earth in two ways: the first kind of satellite passes the equator multiple times per day and scans the entire earth once or twice every 24 hours. This type of satellite is called a geocentric satellite, see Figure 3.11. The second kind is a geostationary satellite which is placed at an altitude of approximately 35,800 km directly above the equator. At this particular altitude, one orbit takes 24 hours, the same length of time as the earth requires to rotate once on its axis. The term geostationary comes from the fact that such a satellite

[5]Dutch: Waterschap

Table 3.2: Average and maximum freshwater discharges in $m^3\ s^{-1}$ at the different sluices for the year of 2015. The sluice numbers correspond to those in Figure 3.10.

Number	Name	Yearly averaged discharge [$m^3\ s^{-1}$]
1	Den Oever	252.43
2	Kornwederzand	241.20
3	Clevering	47.79
4	Helsdeur	11.34
5	Oostoever	6.56
6	Harlingen	2.54
7	Krassekeet	0.67
8	Dijkmanshuizen	0.67
9	Prins Hendrik	0.46
10	Eierland	0.41
11	De Schans	0.15
12	Zandkes	0.01
	Total sluices	564.23
	Lobith	1924.04

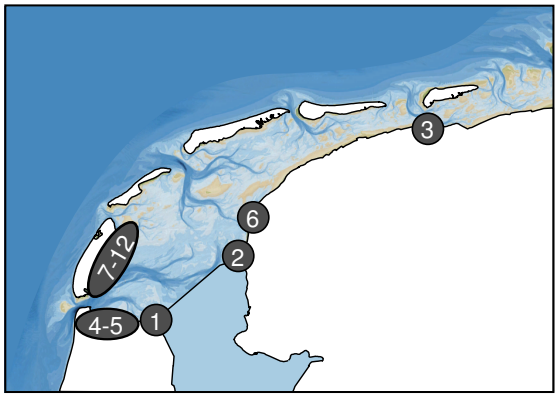

Figure 3.10: Location of sluices discharging fresh water into the Wadden Sea. The sluice numbers correspond to those in Figure 3.2

Table 3.3: Available SST data for 2015 from the NOAA database. The symbol in front of each row indicates whether or not the dataset is used for this thesis. The spatial resolution is the resolution measured right below the satellite (nadir)

	Satellite	Instrument	Spatial resolution	Orbit	Launch date
✓	Aqua	MODIS	1 km	Geocentric	04-05-2002
✗	GCOM-W	AMSR2	25 km	Geocentric	17-05-2012
✓	MetOp-A	AVHRR	1.1 km	Geocentric	19-10-2006
✗	MetOp-A	IASI	12 km	Geocentric	19-10-2006
✓	MetOp-B	AVHRR	1.1 km	Geocentric	17-09-2012
✗	MSG03	SEVIRI	25 km	Geostationary	05-07-2012
✓	NOAA-18	AVHRR	1.1 km	Geocentric	20-05-2005
✓	NOAA-19	AVHRR	1.1 km	Geocentric	06-02-2009
✓	Suomi NPP	VIIRS	0.75 km	Geocentric	28-10-2011
✓	Terra	MODIS	1 km	Geocentric	18-12-1999

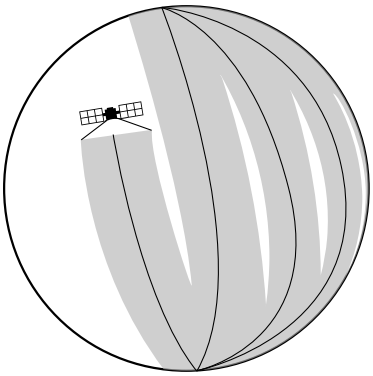

Figure 3.11: Path taken by a satellite in geocentric orbit, also called a swath. Some satellites, like the Aqua or Terra can not cover the entire width of the equator in one day, as is shown in this picture. Though in the higher latitudes swaths can overlap, resulting in multiple images of the same location

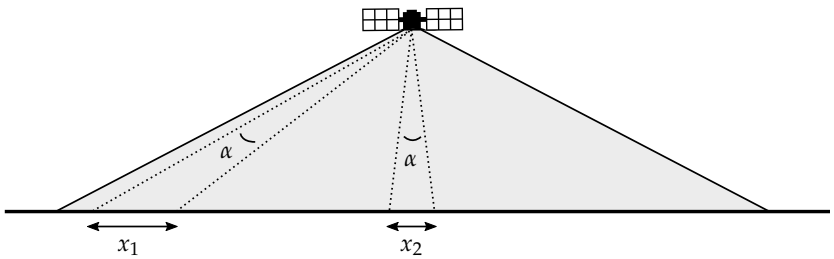

Figure 3.12: The spatial resolution of satellite images is not consistent everywhere on the image. Right beneath the satellite (nadir) the resolution is at its finest, closer to the sides of the picture the resolution becomes less as can be seen by the pixel width: $x_1 > x_2$. This effect is clearly observed with the geostationary MSG03 satellite when taking photographs

appears nearly stationary in the sky as seen by ground-based observers. The disadvantage of these satellites is the diminishing resolution when used for measurements in the higher latitudes. This is caused by the phenomena illustrated in Figure 3.12, where pixel width increases on the border of a photograph. This is always the case, also when for example you take a photograph of a building. This effect is more noticeable with satellite imagery however, because of the shear area recorded in a remotely sensed photograph. Satellites with a geocentric orbit do feel this effect as well, though the photographed area is smaller compared to geostationary satellites.

Satellite data is freely available through the National Oceanic and Atmospheric Administration (NOAA) database[6]. Table 3.3 shows the available datasets on the database which have produced data for the year of 2015. Every dataset from Tab.3.3 will be shortly treated as to why it is used (indicated by a ✓) or why it is not used (indicated by a ✗)

There is only one geostationary satellite, the MSG03 (renamed to Meteosat-10). The photographs taken with this satellite have a 25 km pixel width at the Gemini location. This is too large for the research in this thesis and thus this dataset is not used.

MODIS is a wide field of view instrument that is carried by both the US Terra and Aqua satellites. The Terra satellite has an equatorial crossing time of 10:30 while the Aqua satellite has an equatorial crossing time of 13:30, so that two MODIS instruments can be used to collect information. It is a conventional radiometer, using a scanning mirror measuring in 36 spectral bands. These bands each record a part of the electromagnetic spectrum optimized for different usages like: leaf/canopy differences, sediments, chlorophyll, cloud amount, etc. Spectral band 20 is used for measuring the sea surface temperature, with a resolution of 1 km at the nadir [MATHER AND KOCH, 2011].

The Advanced Very High Resolution Radiometer (AVHRR) is a scanning system with five spectral bands. The fifth band is used for sea surface temperature having a resolution of 1.1 km at the nadir. Carried by the American NOAA series and by the MetOp series developed by the European Space Agency (ESA), these satellite series were intended to be a meteorological observing system. The imagery acquired by AVHRR has, however, been widely used in land cover monitoring at global and continental scales.

The Visible/Infrared Imager Radiometer Suite VIIRS will replace the AVHRR and MODIS instruments. With a spatial resolution of 750 m at the nadir, data from the VIIRS instrument is only available from the Suomi NPP satellite.

On board the MetOp-A satellite the IASI sensor is mounted. This instrument is the main payload for the purpose of supporting numerical weather prediction. It provides information on the vertical structure of the atmospheric temperature and humidity in an unprecedented accuracy with a vertical resolution of 1 km. Sea surface temperature measurements are also made, though with a spatial resolution of 12 km at the nadir. This resolution is too inaccurate for the purpose of this thesis, hence this dataset will not be used.

[6]NOAA database: `http://data.nodc.noaa.gov/thredds/catalog/ghrsst/L2P/catalog.html`

The last satellite from the list in Table 3.3 is the GCOM-W with the AMSR2 sensor on board. This instrument is special in the way that it does not record light from the infrared (IR) spectrum, but rather from the microwave spectrum. While IR SSTs have a higher resolution than microwave SSTs (1-4 km for IR as compared to 25 km for microwave), the IR retrieval is prevented by clouds where the microwave signal is not. The through-cloud capabilities of microwave radiometers provide a valuable picture for global sea surface temperature studies. For more detailed interpretation this dataset is not sufficient and thus won't be used in this thesis.

The datasets marked with a check mark (✓) in Table 3.3 are used for this thesis. MODIS, AVHRR and VIIRS are able to give a high enough resolution. The accuracy of these instruments has been investigated by LIANG AND IGNATOV [2013]. The MODIS can give accurate SST measurement up to 0.6 K, the AVHRR instrument has an accuracy of 0.1 K and VIIRS of 0.14 K.

3.1.6 Remote sensing processing

The chosen satellites from Figure 3.3 produce the accurate enough SST data needed for this investigation. However, photographs are made of the entire earth. The NOAA database is huge, Choices have to be made and smart crawling has to be done to get SST data at the Gemini location for the year of 2015.

The SST data on the NOAA database is maintained by GHRSST. This Group for High Resolution Sea Surface Temperature[7] provides a new generation of global high-resolution SST data products to the scientific community. Proposed in Tokyo 2002, the processing and management of large datasets are distributed between international institutions which share the load. The main agencies responsible for SST collection (NASA, ESA, etc.) share their data with GHRSST.

SST data is processed on different levels. Table 3.4 shows the definition of these levels conform the standard NASA definitions, and more or less following common usage trends [GHRSST, 2008]. Basically raw instrument data is labeled as L0. L1 then adds time referencing and the exact coordinates for the SST measurements. The L2 product contains all processing done on the original swath data, without any gridding or averaging. L3 products average the SST product over time and space. This is especially useful for looking at global temperature patterns. The L4 product then uses multiple datasets and basically cross-pollinates these.

L3 and L4 processing are not wanted for the purpose of this thesis. This is because these products average SST measurements over multiple days, effectively filtering out the small temperature nuances. It are these small differences we are interested in. The L2 product contains the raw instrument data with time referencing and a calibrated coordinate system. Also for the VIIRS and AVHRR the effects of clouds are filtered out. This can be seen in Figure 3.13a and 3.13b. The MODIS dataset measures clouds as very cold water, giving the dark blue color. The VIIRS and AVHRR datasets assign a NaN value to the clouds making the area white. Both images are taken only 8 minutes apart.

[7] GHRSST website: `https://www.ghrsst.org/`

Table 3.4: Definition of satellite data processing levels, from GHRSST [2008]

Level	Description
L0	Unprocessed instrument and payload data at full resolution.
L1A	Reconstructed unprocessed instrument data at full resolution, time referenced, and annotated with ancillary information, including radiometric and geometric calibration coefficients and geo-referencing parameters, computed and appended, but not applied, to the Level 0 data.
L1B	Level 1A data that have been processed to sensor units.
L2	Geophysical variables derived from Level 1 source data at the same resolution and location as the Level 1 data i.e., satellite projection with geographic information.
L3	Level 2 variables mapped on uniform space-time grid scales.
L4	Results from analyses of lower level data (e.g., variables derived from multiple measurements). E.g., SST data sets generated from multiple source satellite data using optimal interpolation.

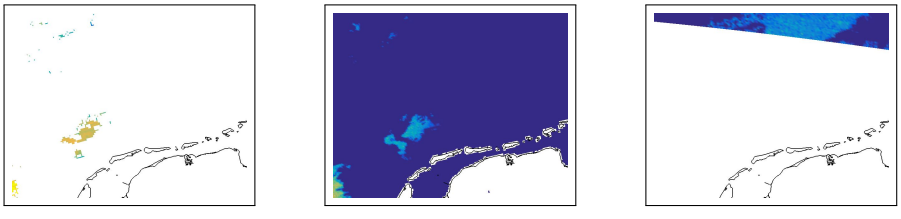

(a) **(b)** **(c)**

Figure 3.13: Reasons for discarding imagery. **(a)** shows the VIIRS or AVHRR instrument filtering out clouds. White areas represent NaN's. **(b)** is the MODIS instrument recording clouds as very cold water. **(c)** shows the end of a photograph. The region of interest is not visible hence this image is discarded as well

The L2 satellite data is hosted on the NOAA database. These satellites make a geocentric orbit around the earth. This means the database contains tens of thousands of photographs of the entire earth. The way this works is the continuous photo series is cut up into pieces and uploaded to the server. The first processing step is to make a database crawler designed to list only those photographs in which the region of interest is visible.

Data is stored as netcdf files. This is a file format which is self describing. This means that there is a header which describes the layout of the rest of the file. By storing the data in such a way that allows efficient subsetting, data is quickly accessible. In other words: data can be quickly accessible without downloading the entire data file, which can sometimes amount up to 300 mb. The Matlab crawler works by exploiting this property. A server request is made to only give the borders of the photograph (easternmost, westernmost longitude and northernmost, southernmost latitude). If the borders contain the Gemini location, the url is logged, otherwise the next netcdf file is investigated.

The result of this crawler was a list of 4,837 links to the netcdf files. The next step is to download each of those files and make an inventory of the data inside the netcdf file. All available parameters are stored in a .mat file and saved in corresponding folders. Basically all 4,837 files have been downloaded and saved as a matlab data file for quick access.

The next step is to process the raw .mat files in such a way intricate temperature differences are visible. A Matlab script is made cutting a predefined bounding box out of the raw data. After this bounding box operation the data is again saved as a .mat file. The raw dataset is kept for backup means. The smaller cut-out dataset is used for the actual plotting of the sea surface temperature. Matlab is used again to plot the sea surface temperature. The sea surface temperature measured at the Gemini location is used to calibrate the colorbar in the plots. The colorbar is calibrated at 1 °C below and 1 °C above the reference sea temperature. By iterating through every .mat file, generating a plot and saving the result as a .png file, 4,837 images have been created.

Most of the images can be discarded right away. This is because the Netherlands and the North Sea are cloudy most of the time, see Figure 3.13a and 3.13b. These images are useless for the research in this thesis and are therefore discarded. Another reason to discard images right away is the nett measurement area of the satellite. Sometimes SST values are within our bounding box of interest, but lay too far away from the Gemini project location. This phenomena can be seen in Figure 3.13c. Both phenomena result in a discarded image. After this visual inspection 411 usable images result from the period of 16-02-2015 to 14-10-2015. Still interpretation should be done with care.

The resulting 411 images are gathered in CLAESSENS *et al.* [2016]. Interpretation should be made with care. Still phenomena occur which seem like interesting temperature distortions but in reality originate from other processes, here a summation is made;

- The effect of diminishing resolution treated in Figure 3.12 can give rise to a distorted image. Figure 3.14 is the result of this distortion. Both images are taken 10 minutes apart by the same sensor (on a different satellite though). Figure 3.14a clearly shows a lower resolution then Figure 3.14b.

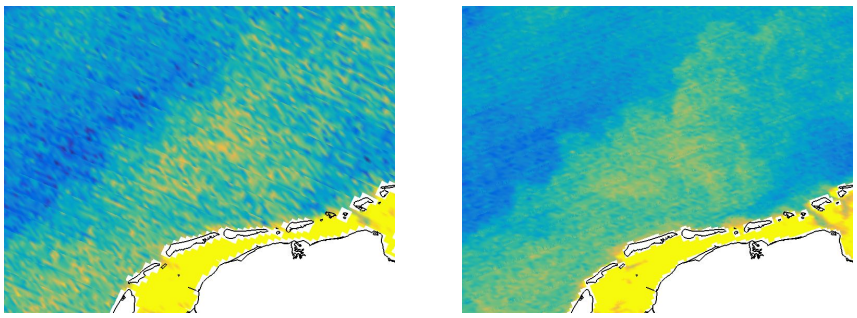

Figure 3.14: The effect of diminishing resolution at the borders of large image. **(a)** is recorded at the border of an image by the Terra satellite, a poor resolution is observed. **(b)** is recorded 10 minutes later by the Aqua satellite. A better resolution can be seen eventhough the same instrument made the photograph. The Aqua satellite made this picture closer to the nadir then the Terra satellite did, see Figure 3.12 for an explenation of the phenomena observed

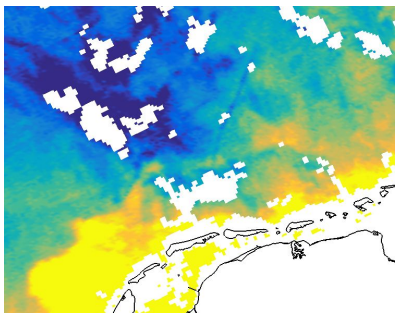

Figure 3.15: Cloud effects penetrating through the L2flags processing. The white area indicates the removal of data which is flagged. Still darker patches of water are observed at the border of the easternmost white areas. These are cloud effects which are not picked up completely

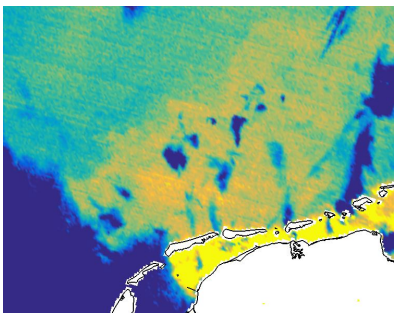

Figure 3.16: This picture is made by a MODIS instrument in which clouds are observed by dark patches of water. The small darker areas are not an indication of cold water, these are cloud artefacts

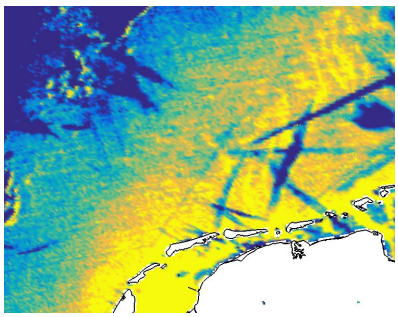

Figure 3.17: Stripes of dark blue water are most likely vapor trails caused by airplanes. The straight line is not natural. The vapour is recorded by the satellite instrument as a cloud which is cold

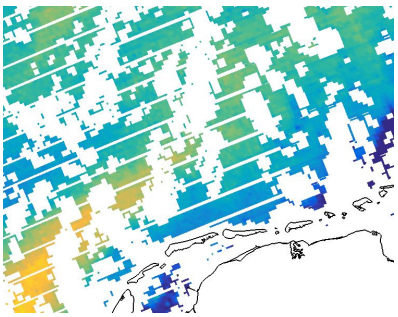

Figure 3.18: VIIRS SST image with bow-tie distortions and deletions. On board deleted pixels are shown as the white lines, see GLADKOVA *et al.* [2016] for more details about this phenomena

- The border of flagged phenomena can persist through and appear as cold/warm water. Figure 3.15 shows the discarded temperatures due to clouds as white pixels. The edges of these pixels are however still dark blue. This does not mean cold water is present, it means cloud effects persisted through the filtering.
- Making a clear distinction between clouds and cold water can be difficult especially with the MODIS dataset. Figure 3.16 seems to contain cold water patches. This is not true, the surrounding area gives away clouds are present. The interpreter should be weary, these dark patches of water in the middle of the image are most likely the influence of clouds.
- Planes leave behind trails of condensed water vapor similar to clouds. The unnatural straight blue lines in Figure 3.17 are no special cold water phenomena. Instead, planes probably flew over this area.
- The VIIRS dataset sometimes show erroneous values in its SST data. Satellites scan the earth's surface in bands. These bands are afterwards stitched together to form a uniform image. Due to bow-tie distortions and an erroneous correction white stripes can occur representing failed "stitching". See GLADKOVA *et al.* [2016] for more information on this phenomena.

3.2 Model results

Current velocities at the Gemini location are acquired from measurements as described in section 3.1. In this section the acquisition of current velocities is treated which are calculated by the DCSMv6-ZUNOv4-KF model used by Rijkswaterstaat.

This model is a combination between the DCSMv6 and ZUNOv4 models which are coupled through a horizontal domain decomposition. The ZUNOv4 model is a two dimensional model which covers the whole southern North Sea including a part of the English Channel and has a finer resolution then the DCSMv6 model. The boundary conditions of the more detailed ZUNOv4 model are implemented from the larger continental shelf model DCSMv6. Figure 3.19 shows both domains and the boundary conditions for the ZUNOv4 model as dotted white lines.

The DCSMv6ZUNOv4-KF model is actuated through meteorological data: wind speed and air pressure over the surface of the entire area of the model. This forcing is realized by the meteorological forecast of the HIRLAM v7.2 from the KNMI. After 2014 this data is obtained directly from the KNMI ftp server providing a robust system.

The last part of the DCSMv6-ZUNOv4-KF model name refers to the Kalman Filter. This filter assimilates water level measurements from 32 locations (the red dots with white borders from Figure 3.19) to improve accuracy considerably. A recent test has shown a water level prediction improvement by a factor of two compared to the model without a Kalman filter [SUMIHAR, 2012].

The resulting DCSMv6-ZUNOv4-KF model is barotropic and depth averaged designed for storm surge predictions with a maximum water level deviation of 5 cm compared to the actual measurements [ZIJL, 2013]. This validated

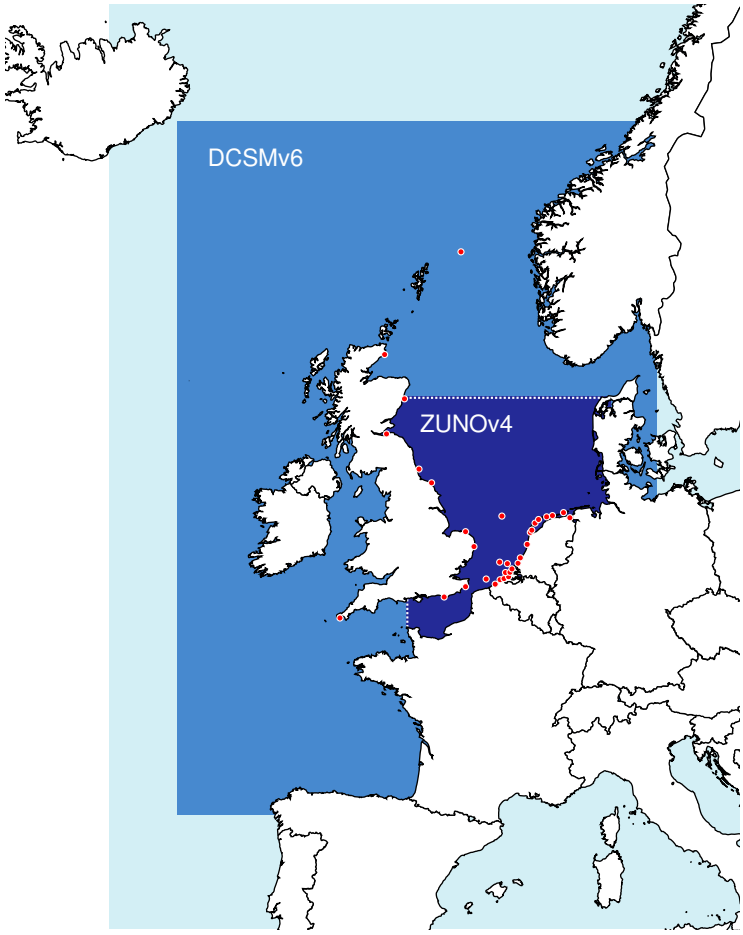

Figure 3.19: Model domain of DCSMv6-ZUNOv4-KF: The dotted white line indicates the border coupling between the DCSMv6 and ZUNOv4 models. The red dots with a white border are the locations of 32 water level measurement stations used for data assimilation

accuracy does not apply for current velocities, as there are little current velocity measurements to validate it with. According to ZIJL AND TIESSEN [2015] during normal (neap- and spring tide) conditions the current velocity is represented correctly by both models. The high current velocities during the March 2007 storm have been predicted correctly by both the DCSMV6 and the DCSMV6-ZUNOV4-KF model.

The most recent hindcast and forecast of different parameters like astronomical tide, total water elevation, current velocities, etc. are exported to MATROOS, an online database hosted by Rijkswaterstaat. The hourly water level and current velocities have been extracted from this database for the year of 2015 at the project location (53.0403°N and 5.8857°E).

Within this dataset four values of -9999 are found, these are dummy values indicating for example when the water disappears on a tidal flat due to the falling tide or when the measurement equipment used by the data assimilation malfunctions. The exact reason why these four values have a dummy variable instead of a real measurement is not looked into. The resulting time-series is the hourly, depth averaged and barotropic current velocity forced by wind and tidal motions. Baroclinic effects are not included.

3.3 Data analysis

In section 3.1 and 3.2 the obtained data has been presented. In order to investigate the high currents, a tidal analysis is done to extract the tidal components from the signal. Furthermore an EOF analysis is made to extract the mathematical patterns in the current velocity. The methods of both data analysis tools will be treated in this section.

3.3.1 Tidal analysis

A standard part of any oceanic pressure gauge or current meter analysis is the separation of tidal from non-tidal components of the signal. The tidal signal can either be discarded, or its characteristics described in some fashion useful for further analysis.

To separate the tidal signal from the measured- and modeled current velocities the harmonic analysis T_TIDE by PAWLOWICZ *et al.* [2002] is used. Although tidal signals can be removed by standard high or bandpass filtering techniques, their relatively deterministic character and large amplitude make special techniques more effective. In classical harmonic analysis, the tidal signal is modeled as the sum of a finite set of sinusoids at specific frequencies related to astronomical parameters.

Current velocity vectors serve as input for T_TIDE in Matlab. This function outputs tidal constituents, phases and the tidal current profile. T_TIDE has been used for all 18 different depth layers the ADCP has measured in.

3.3.2 EOF analysis

In statistics the method of Empirical Orthogonal Function (EOF) analysis is a decomposition of a signal or data set, just like Fourier analysis or wavelet

transforms. In the case of EOFs, the constituents are a set of mutually orthogonal components. The methods depends on finding the eigenfunctions of the correlation function of the variable [KANTHA AND CLAYSON, 2000]. EOFs constitute the most optimum means of decomposing (and reconstituting) a signal, made possible by the fact that they are orthogonal to one another. They can also be looked upon as the most efficient way of characterizing a time series or data set.

The decomposed time series consist of the dominant modes found in the time series, these modes are called the EOFs of the system. They are an ordered set in that the first one contains the most variance, the second one the second-most, and so on, so that it is possible to retain only the most essential components of the signal (and reconstitute it appropriately).

For the data analysis in this thesis the program DINEOF is used[8]. This software is is an EOF-based tool to quickly analyze large datasets and plot the EOF patterns with their corresponding "importance". DINEOF has proven to be an accurate technique, and it produces reliable results [ALVERA-AZCÁRATE *et al.*, 2007].

DINEOF makes use of the Singular Value Decomposition (SVD) to make the EOF analysis. SVD is one of the most useful matrix factorizations in applied linear algebra with applications such as data compression or solving linear equations. SVD gives us an optimal low-rank representation of a system, getting rid of the least important modes. More information about the theoretical background of the SVD decomposition can be found in appendix A.

To sum up for clarity:

- EOF is an analysis technique
- SVD is a matrix operation from linear algebra
- DINEOF is a tool which uses the SVD decomposition to make an EOF analysis

3.4 Delft3D

The effect of the meteorological parameters on the sea surface temperature is modeled with Delft3D. Developed by Deltares, this fully integrated computer software suite can carry out simulations of flows, sediment transports, waves, water quality, morphological developments and ecology.

The Delft3D suite is composed of several modules, grouped around a mutual interface, while being capable to interact with one another. Delft3D-FLOW, which is used for the heating computation, is one of these modules. Delft3D-FLOW is a multi-dimensional (2D or 3D) hydrodynamic (and transport) simulation program which calculates non-steady flow and transport phenomena that result from tidal and meteorological forcing on a rectilinear or a curvilinear, boundary fitted grid [DELTARES, 2014]:

The sea surface temperature will be modeled for different water depths. A 5×5 grid with closed boundaries will be used. This results in undisturbed heating behavior without the mixing effects of the tide. Meteorological and wind forcing

[8]Homepage of DINEOF: `http://modb.oce.ulg.ac.be/mediawiki/index.php/DINEOF`

will be added by using the KNMI data from station 235 - De Kooy (see location ⑦ in Figure 3.1).

Delft3D's heat flux model 5 (Ocean model) is used for this simulation. Following GILL [1982] and LANE [1989] this model was calibrated for the North Sea and successfully applied for great lakes. For computation of the heat terms the equations (3.3) to (3.9) are used (See Figure 3.20). An explanation of the coefficients and resulting equations are displayed in Table 3.5.

$$Q_{eb} = \epsilon\sigma\bar{T}_s^4(0.39 - 0.05\sqrt{e_a})(1.0 - 0.6F_c^2) \tag{3.3}$$

$$Q_{ev} = Q_{ev,\text{forced}} + Q_{ev,\text{free}} \tag{3.4}$$

$$Q_{ev,\text{forced}} = L_v\rho_a f(U_{10})\{q_s(T_s) - q_a(T_a)\} \tag{3.5}$$

$$Q_{ev,\text{free}} = k_s L_v\bar{\rho}_a(q_s - q_a) \tag{3.6}$$

$$Q_{co} = Q_{co,\text{forced}} + Q_{co,\text{free}} \tag{3.7}$$

$$Q_{co,\text{forced}} = \rho_a c_p g(U_{10})(T_s - T_a) \tag{3.8}$$

$$Q_{co,\text{free}} = k_s\bar{\rho}_a c_p(T_s - T_a) \tag{3.9}$$

The hourly meteorology data is used in Delft3D by means of .tem files. Part of the file is displayed in Figure 3.7. Time is recorded in minutes from an arbitrarily chosen reference date, for this model at 01-01-2015. The first column in the .tem file represents the measurement time in minutes determined with respect to the reference date. The second column is the relative humidity [%], the third column the air temperature [°C], fourth the cloud coverage [%] and the fifth column is the solar radiation [W m^{-2}].

KNMI station De Kooy records all four parameters on an hourly interval. As calculated in Equation 3.1 the global radiation is measured in energy flow units [J cm^{-2}] and needs to be converted to the standard unit for irradiance [W m^{-2}]. This can be done by multiplying the measurement with 2.78. With this transformation the .tem file can constructed using a simple Matlab operation.

Wind data is also incorporated in the heating simulation. This is done using Delft3D .wnd files. The first five lines of the used .wnd file is displayed in Figure 3.8. The first column again represents the time in minutes from the reference time of 01-01-2015. Column two is the absolute wind velocity and column three represents the wind direction in degrees. This data is also available from measuring station De Kooy. The .wnd file used in Delft3D is constructed using yet another Matlab script.

Both .wnd and .tem files contain the hourly averaged values for the whole year of 2015. Delft3D then uses the represented values in its computation once the internal timer hits the representing value. Computations have been made for water depths of 1, 2, 5, 10 and 30 m.

Table 3.5: Heat flux model constants and equations

Variable	Description	Value
α	Molecular diffusivity of air	ν_{air}/σ_p [m^2 s^{-1}]
c_e	Dalton number	0.0015 [-] (North Sea)
$c_{fr.conv}$	Coefficient of free convection	Calibrated to 0.14 [-]
c_H	Stanton number	0.00145 [-] (North Sea)
c_p	Specific heat of air	1004.0 [J kg^{-1} K^{-1}]
ϵ	Emissivity coefficient	0.985 [-]
e_a	Actual vapor pressure	$r_{\text{hum}} \cdot 10^{\frac{0.7859+0.03477T_a}{1.0+0.00412T_a}}$ [mbar]
e_s	Saturated vapor pressure	$10^{\frac{0.7859+0.03477T_s}{1.0+0.00412T_s}}$ [mbar]
F_c	Fraction of sky coverage	Measurement [%]
$f(U_{10})$	Wind function	$c_e U_{10}$ [m s^{-1}]
g	Acceleration due to gravity	9.81 [m s^{-2}]
$g(U_{10})$	Wind speed function	$c_H U_{10}$ [m s^{-1}]
k_s	Heat transfer coefficient, (if $\rho_{a10} - \rho_{a0} \leq 0$)	0
k_s	Heat transfer coefficient, (if $\rho_{a10} - \rho_{a0} > 0$)	$c_{fr.conv}\left(\frac{g\alpha^2}{\nu_{air}\bar{\rho}_a}(\rho_{a10} - \rho_{a0})\right)^{1/3}$
L_v	Latent heat of vaporisation	$2.5 \cdot 10^6 - 2.3 \cdot 10^3 T_s$ [J kg^{-1}]
ν_{air}	Viscosity of air	$16.0 \cdot 10^{-6}$ [m^2 s^{-1}]
P_{atm}	Local atmospheric pressure	Measurement [Pa]
q_a	Specific humidity of remote air	$\frac{0.62e_a}{P_{\text{atm}} - 0.38e_a}$ [%]
q_s	Specific humidity of saturated air	$\frac{0.62e_s}{P_{\text{atm}} - 0.38e_s}$ [%]
ρ_a	Density of air	Measurement [kg m^{-3}]
$\bar{\rho}_a$	Average air density	$\frac{\rho_{a0} + \rho_{a10}}{2}$ [kg m^{-3}]
ρ_{a0}	Saturated air density	$\frac{\frac{100P_{atm} - 100e_s}{R_{dry}} + \frac{100e_s}{R_{vap}}}{T_s + 273.15}$ [kg m^{-3}]
ρ_{a10}	Saturated air density	$\frac{\frac{100P_{atm} - 100e_a}{R_{dry}} + \frac{100e_a}{R_{vap}}}{T_a + 273.15}$ [kg m^{-3}]
r_{hum}	Relative humidity	Measurement [%]
R_{dry}	Gas constant for dry air	287.05 [J kg^{-1} mol^{-1}]
R_{vap}	Gas constant for water vapor	461, 495 [J kg^{-1} mol^{-1}]
σ	Stefan-Boltzmann constant	$5.67 \cdot 10^{-8}$ [J m^{-2} s^{-1} K^{-4}]
σ_p	Prandtl number	0.7 [-] (for air)
T_a	Air temperature	Measurement [°C]
T_s	Water surface temperature	Measurement [°C]
$\bar{T}_a$	Absolute air temperature	Measurement [K]
$\bar{T}_s$	Absolute water surface temperature	Measurement [K]
U_{10}	Averaged wind speed 10 m above free surface	Measurement [m s^{-1}]

Table 3.6: Terms of the heat balance used in the Ocean heat model

Quantity	Description	According to
Q_{sn}	Net solar radiation	Measurements
Q_{eb}	Effective back radiation	Eq. (3.3)
Q_{ev}	Heat loss due to evaporation	Eq. (3.4)
Q_{co}	Heat loss due to convection	Eq. (3.9)

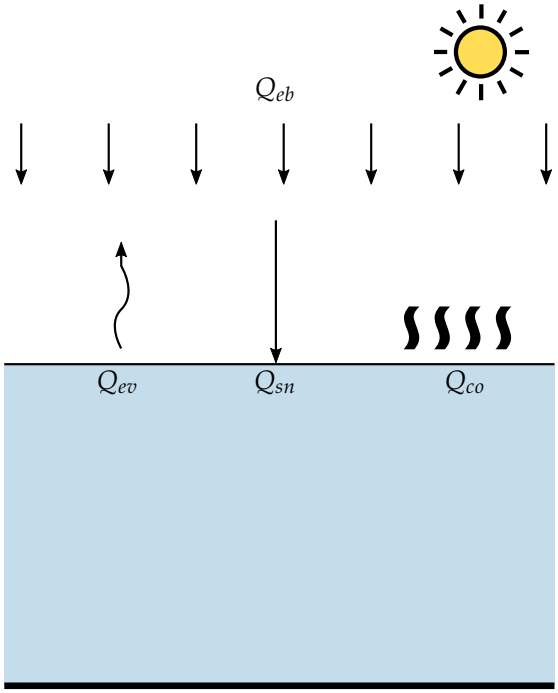

Figure 3.20: Net solar radiation (Q_{sn}) shown as the major influx arror. Effective back radiation (Q_{eb}) shown as the array of arrows. Heat loss due to evaporation (Q_{ev}) and convection (Q_{co}) are the upward arrows

Table 3.7: First 5 lines of the .tem file used by the heating simulation

2.4000000e+02	9.0000000e+01	6.9000000e+00	1.0000000e+02	0.0000000e+00
3.0000000e+02	9.3000000e+01	6.1000000e+00	0.0000000e+00	0.0000000e+00
3.6000000e+02	9.2000000e+01	6.4000000e+00	1.0000000e+02	0.0000000e+00
4.2000000e+02	9.2000000e+01	6.5000000e+00	1.0000000e+02	0.0000000e+00
4.8000000e+02	9.2000000e+01	6.5000000e+00	1.0000000e+02	1.0000000e+00

Table 3.8: First 5 lines of the .wnd file used by the heating simulation

2.4000000e+02	8.0000000e+00	2.3000000e+02
3.0000000e+02	8.0000000e+00	2.0000000e+02
3.6000000e+02	9.0000000e+00	2.1000000e+02
4.2000000e+02	9.0000000e+00	2.2000000e+02
4.8000000e+02	8.0000000e+00	2.1000000e+02

4

Results

The datasets and analysis techniques discussed in chapter 3 can help us understand more about the origin of the high current velocities. In this chapter the results from these datasets and analysis will be presented. In section 4.1 the measured and modeled current velocities will be investigated. section 4.2 presents the results of the wind influence. The third mechanism responsible for the energetic motions in the North Sea, density differences, will be treated in section 4.3. Finally, the influence from the Wadden Sea is discussed in section 4.4.

4.1 Current velocities

The starting point of this research are the measurements of the current velocities at the Gemini wind farm in 2015. This section is dedicated to presenting and validating these measurements. This measurement signal is then separated into it's most dominant mathematical modes using an EOF analysis. This section also treats another method to analyze the signal's separate components. For this the Matlab script T_TIDE is used to make a harmonic tidal analysis.

4.1.1 Measurements and validation

Depicted in Figure 4.1 are the raw buoy measurements. Both the absolute velocity and current direction is. From this the current velocity can be decoupled into an x- and y-direction as can be seen in Figure 4.3. These measurements have been made in the surface layer at 2 m depth because it is here where the highest currents occur. Figure 4.2 shows the distribution through the vertical for all measurement points. The logarithmic profile is visible, also only the top 10 m show the occurrence of currents above 1 m s^{-1}.

These high currents appear only in the month of August. It is the origin of these currents which is the research objective in this thesis. Figure 4.6 shows the 3D current profile of two moments of high currents in the beginning of August. The measurements are made by the TRIAXYS buoy on the Gemini park, more information about these measurements can be found in subsection 3.1.1.

The Nexus, Van Oord's cable laying vessel, has worked at the Gemini wind farm. During it's operations the ADCP device was turned on, logging the current

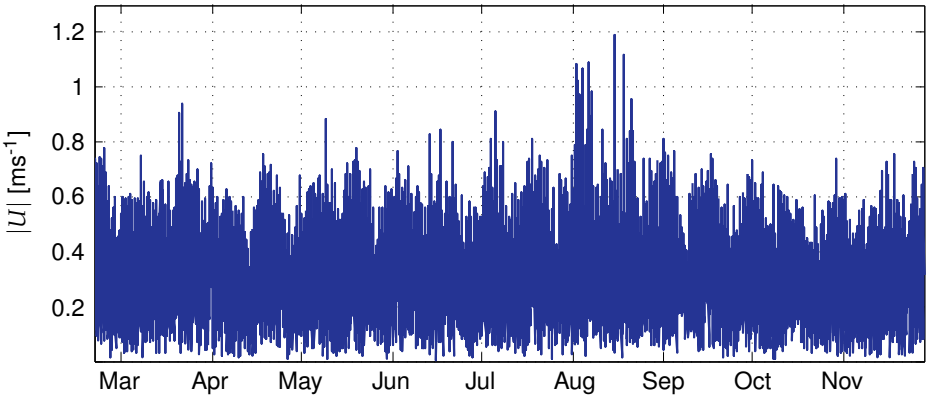

Figure 4.1: Absolute current velocity ($|U|$) measurements at the Gemini location in 2015. Measurements are made at 2 m depth

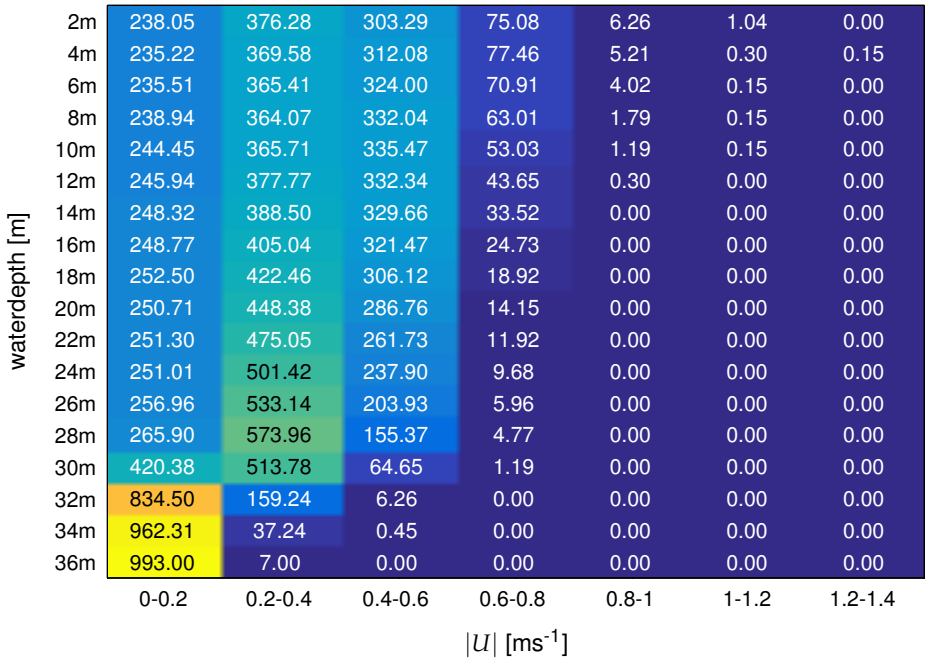

Figure 4.2: Per mille of occurrence ‰. 1000 means all measurements in that water layer fall within that absolute velocity bin

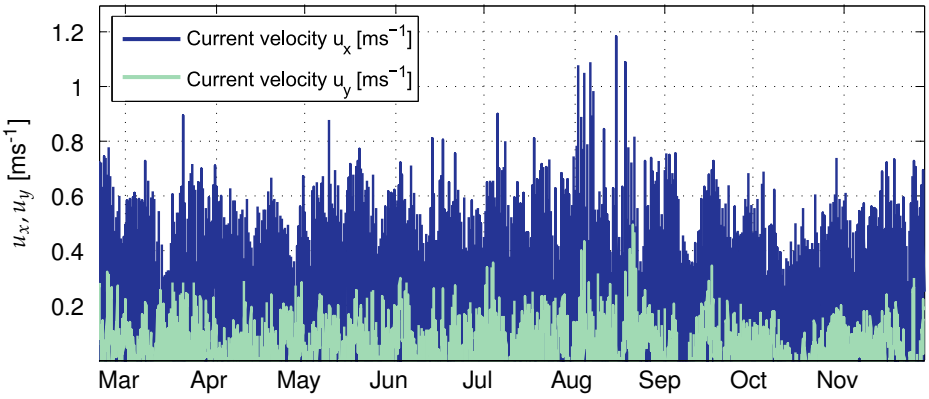

Figure 4.3: The dark line is the decoupled velocity in E-W direction (u_x). The lighter line is the decoupled velocity in N-S direction (u_y). Measurements are made at 2 m depth in the year of 2015

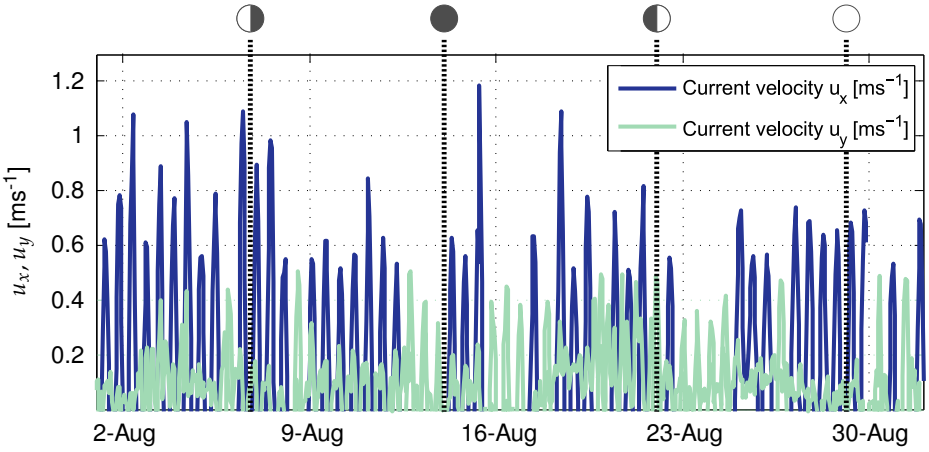

Figure 4.4: The dark line is the decoupled velocity in E-W direction (u_x). The lighter line is the decoupled velocity in N-S direction (u_y). Measurements are made at 2 m depth in the year of 2015. The circles represent the moon. Two and a half day after full moon, the springtide arrives at Gemini

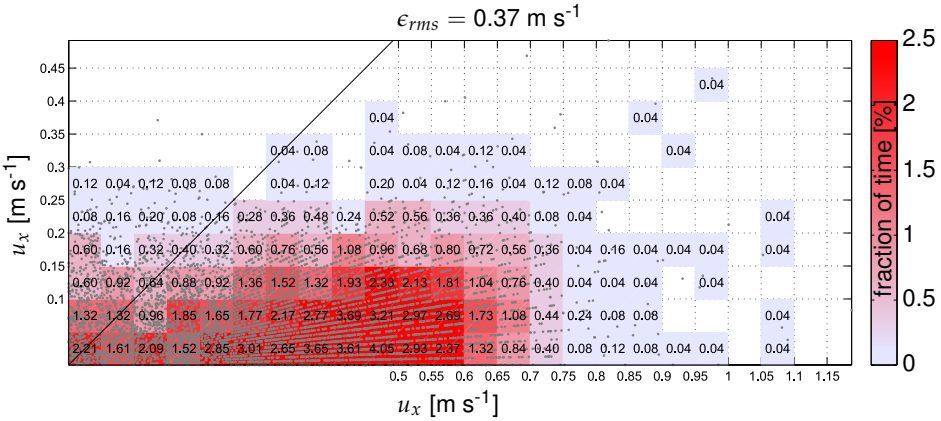

Figure 4.5: Scatter plot from the u_x and u_y current signal. Measurements are made in the first bin, thus at 2 m depth in the year of 2015

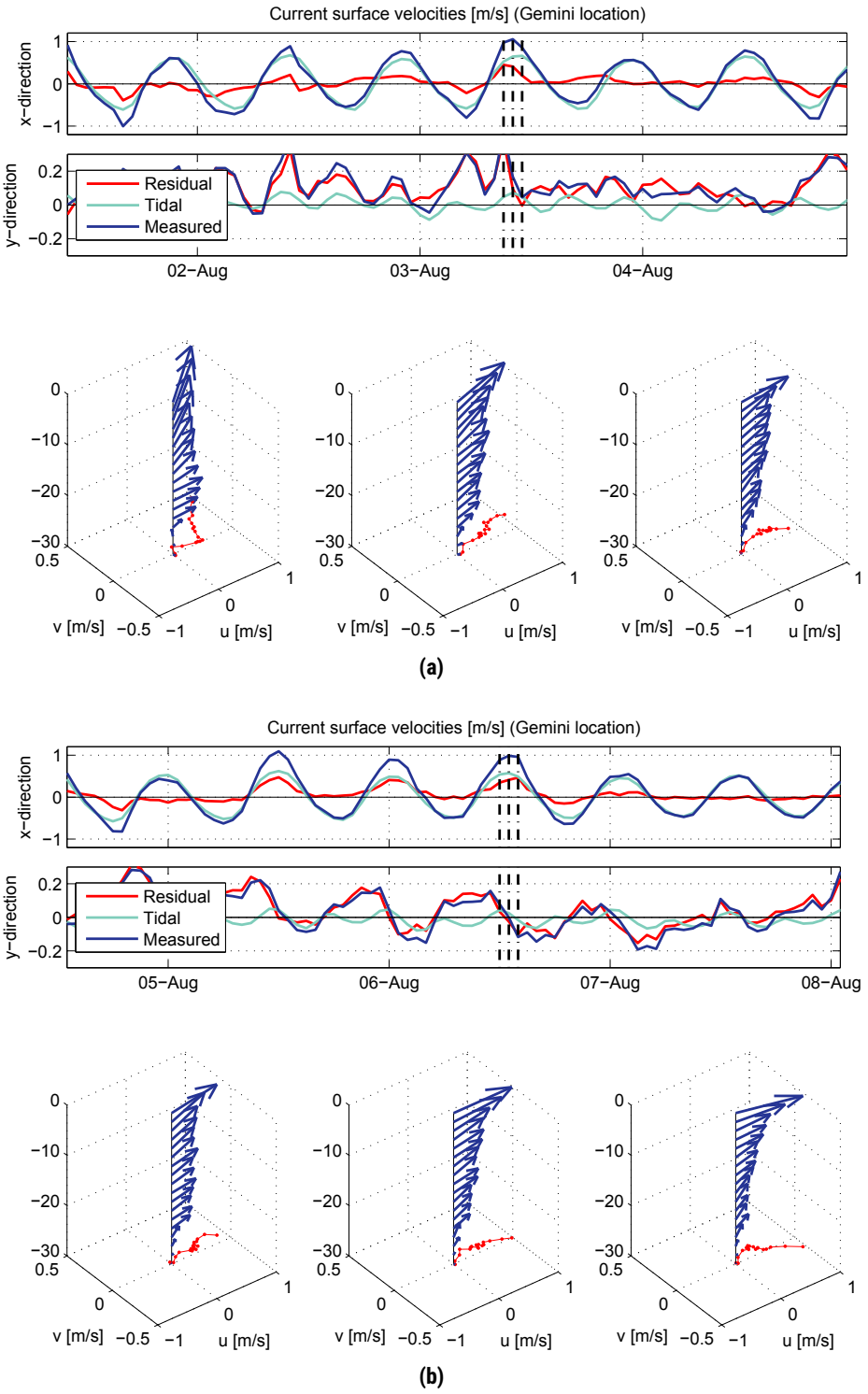

Figure 4.6: 3D current profile accessory to the high surface current measurements in the beginning of August. **(a)** is a closeup of the 2-4 August. **(b)** is a closeup of 5-8 August

velocities beneath the ship. Data has been obtained which contains the average current velocity over 23 m of water depth. According to Figure 4.2 the first 23 m water depth contain a more uniform current distribution then the entire water column. This is because the bottom 10 m are very much influenced by the bottom resulting in lower currents. Averaging over the entire water depth would give a biased signal towards the bottom, while averaging over the first 23 m will give a better representation of the top layers in which we are interested.

Only a small amount of measurements have been made close enough to the TRIAXYS buoy for a fair comparison. For more information about the selection of these time periods see subsection 3.1.1. The resulting measurements of both the Nexus ADCP and the TRIAXYS ADCP are plotted in Figure 4.7. The solid red line represents the depth averaged absolute current velocity made in the top 20 m of water column by the TRIAXYS buoy ($\Delta t = 1$ hour). The black dots are the depth averaged current measurements over the top 23 m of water column, made by the Nexus ($\Delta t = 20$ sec).

Figure 4.7 shows agreement between both datasets. The amplitude and phase seem to overall agree. Some outliers appear. The dots which deviate quite a lot from the main trend are considered outliers. They can be caused by a lot of things, i.e. passing fish, reflection of pings or influence from the ship/ROV.

4.1.2 Signal analysis

At this point we have a 9 month long, validated current time series. With this an EOF analysis can be made using DINEOF. This method makes a linear decomposition of the variations in the data in time and space. It produces a series of modes of variation. These modes are pairs of a spatial pattern (map) linked to a temporal pattern (time series). The workings of DINEOF are explained in subsection 3.3.2 and the theoretical background needed for the underlying SVD decomposition is treated in appendix A.

Four EOF analysis have been made on different datasets. First only the dominant x-direction of the current signal is taken for all 18 bins. With Matlab matrix A is formed with the bin in each row, and the columns filled with the current measurement u_x for every time.

$$A_{bin_m,t_n} = \begin{bmatrix} u_{x;bin_1,t_1} & u_{x;bin_1,t_2} & \cdots & u_{x;bin_1,t_n} \\ u_{x;bin_2,t_1} & u_{x;bin_2,t_2} & \cdots & u_{x;bin_2,t_n} \\ \vdots & \vdots & \ddots & \vdots \\ u_{x;bin_{18},t_1} & u_{x;bin_{18},t_2} & \cdots & u_{x;bin_{18},t_n} \end{bmatrix} \tag{4.1}$$

This matrix is fed into DINEOF which produces temporal and spatial patterns of the EOF modes found within this current signal. Each EOF mode captures a certain amount of the total variance present in the total dataset. By ranking the EOF's from high to low variance, we get an impression of the dominant pieces of information in the data. In Table 4.1 the relative variance for each mode is given in the column with Run_{18}. The number 18 stands for the amount of rows used in the A matrix the analysis is done for.

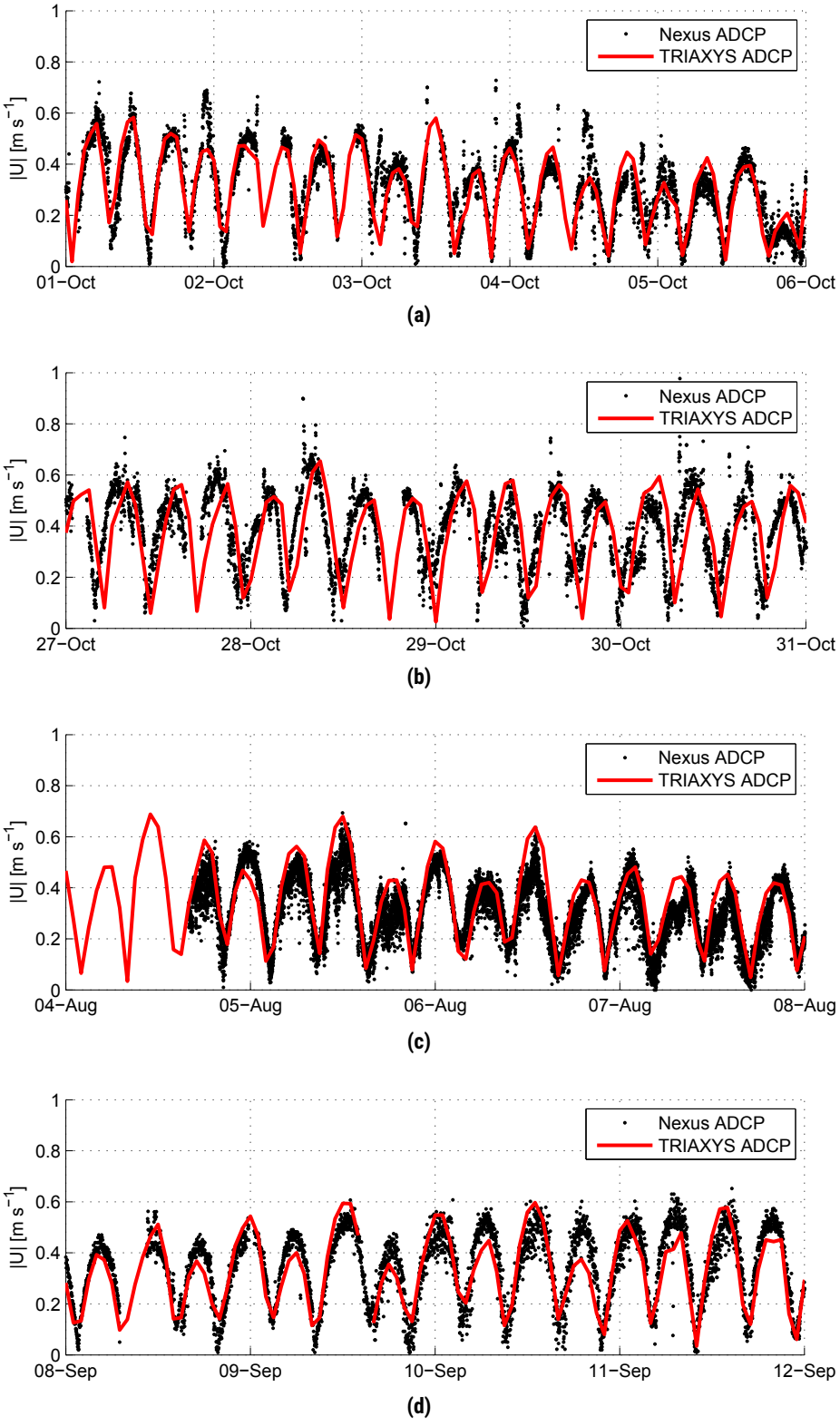

Figure 4.7: The black dots represent dept-averaged current velocities over 23 meter measured by the Nexus ADCP. The red line represents the depth averaged current velocities over 20 meter measured by the TRIAXYS ADCP. Measurements are made 110 m away from each other

Table 4.1: Relative variance (importance) for each of the EOF modes retained by DINEOF, in decreasing order of importance

	Run_{18}	Run_{36}	Run_{72}	Run_{90}
Mode 1	98.01 %	90.71 %	82.50 %	77.40 %
Mode 2	1.06 %	5.13 %	4.89 %	6.11 %
Mode 3	0.39 %	1.68 %	2.98 %	4.57 %
Mode 4	0.19 %	0.86 %	1.93 %	2.81 %
Mode 5	0.11 %	0.51 %	1.41 %	1.82 %
Mode 6		0.26 %	0.96 %	1.39 %
Mode 7		0.14 %	0.51 %	0.91 %
Mode 8		0.12 %	0.41 %	0.48 %
Mode 9		0.10 %	0.38 %	0.40 %
Mode 10			0.31 %	0.36 %

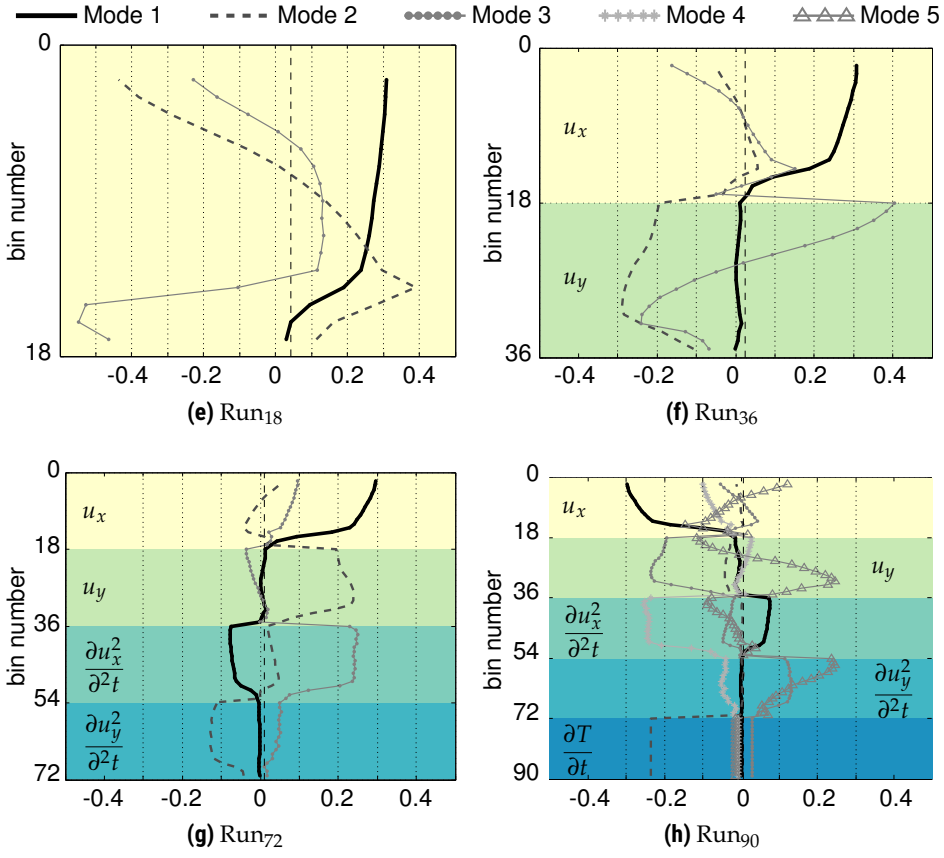

Figure 4.8: Spatial modes as calculated by DINEOF. **(a)** is the result of taken into account only the east-west current velocities (u_x). The mean of EOF patterns is 0.04219. **(b)** takes into account the north-south current velocities (u_y) as well. The mean of these patterns is 0.0231. **(c)** also the second derivatives of u_x and u_y are taken into account. The mean of these patterns is 0.01122. **(d)** shows the contribution of the first derivative of the sea surface temperature. The mean of these EOF's is 0.0092

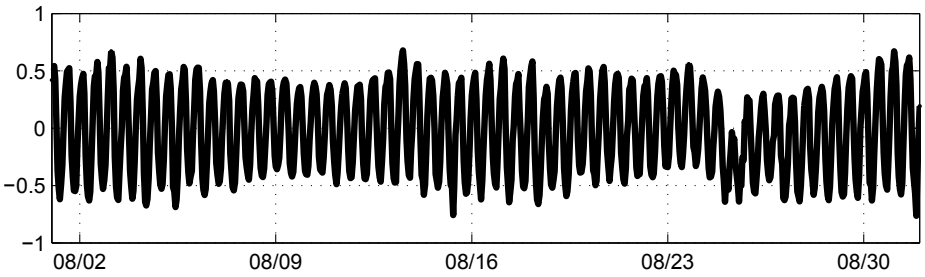

(a) Temporal mode 1 from Run_{90}

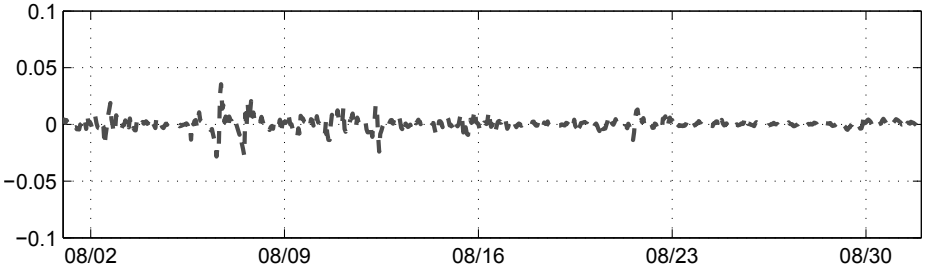

(b) Temporal mode 2 from Run_{90}

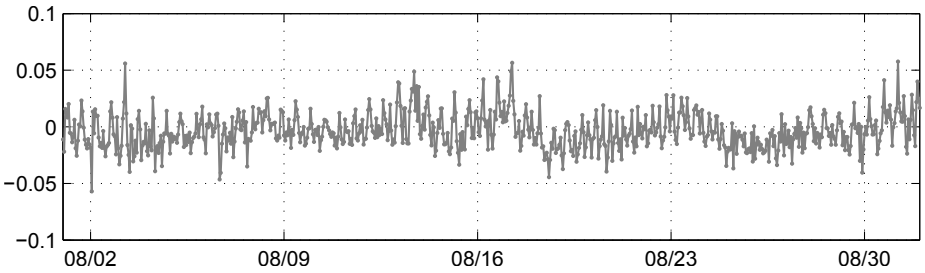

(c) Temporal mode 3 from Run_{90}

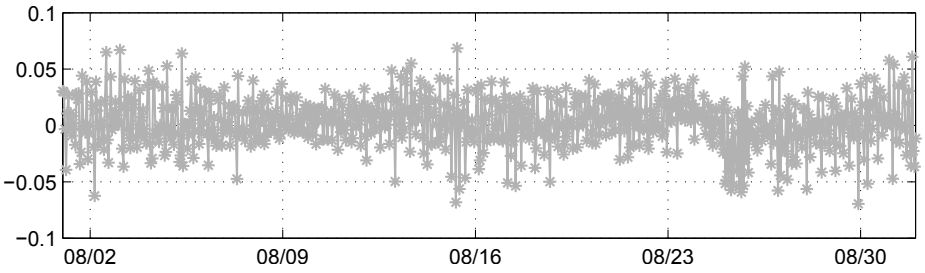

(d) Temporal mode 4 from Run_{90}

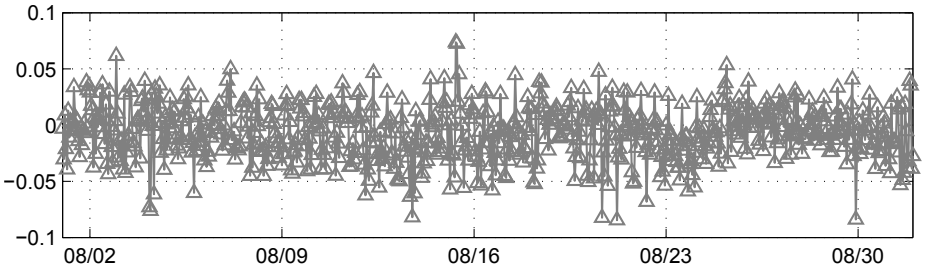

(e) Temporal mode 5 from Run_{90}

Figure 4.9: Temporal modes belonging to Run_{90}. The y-axis shows m s^{-1} in the surface layer

Mode 1 from Run_{18} has a relative variance of 98.01%. This indicates the original signal u_x can be reconstructed for 98.01% using only one EOF. The spatial patterns of the first three modes are displayed in Figure 4.8a. The y-axis shows the measurement bins with bin 1 (2 m water depth) at the top, and bin 18 (36 m water depth) at the bottom. The most dominant EOF pattern is plotted as a thick black line. This can be interpreted as the logarithmic velocity profile of the tidal current. It makes sense this signal is responsible for most of the current measurements. First of all the tidal motions dominate the waters in the area as most of the current velocities are created by this. Secondly the tidal motions are a periodic oscillating phenomena, easily picked up by signal processing.

Mode 2 from Run_{18} is clearly different from the first one as it has both negative and positive values. This means a mode is picked up which flows in one direction in the top of the water column, and in the other direction in the bottom water column. This EOF mode is responsible for 1.06% of the signal. Care has to be taken with the interpretation of these modes. It is uncertain whether this is a real physical phenomena or the representation of noise.

This first EOF analysis only takes into account half of the measurements made at the Gemini location. The second current velocity component u_y is taken into account for the second EOF analysis. To process two different datasets they simply have to be placed beneath each other.

$$A_{bin_m,t_n} = \left[\begin{array}{cccc} u_{x;bin_1,t_1} & u_{x;bin_1,t_2} & \cdots & u_{x;bin_1,t_n} \\ u_{x;bin_2,t_1} & u_{x;bin_2,t_2} & \cdots & u_{x;bin_2,t_n} \\ \vdots & \vdots & \ddots & \vdots \\ u_{x;bin_{18},t_1} & u_{x;bin_{18},t_2} & \cdots & u_{x;bin_{18},t_n} \\ \hdashline u_{y;bin_1,t_1} & u_{y;bin_1,t_2} & \cdots & u_{y;bin_1,t_n} \\ u_{y;bin_2,t_1} & u_{y;bin_2,t_2} & \cdots & u_{y;bin_2,t_n} \\ \vdots & \vdots & \ddots & \vdots \\ u_{y;bin_{18},t_1} & u_{y;bin_{18},t_2} & \cdots & u_{y;bin_{18},t_n} \end{array}\right] \tag{4.2}$$

The resulting spatial pattern is depicted in Figure 4.8b with the relative variance given in Table 4.1 in column Run_{36}. Two layers are visible, one for u_x and one for u_y.

The most dominant mode, Mode 1 in Run_{36} represents 90.71% of the signal. This spatial pattern has its dominant features in the u_x zone, and not so much in u_y. The second mode in Run_{36} is five times more significant then the third EOF mode. This could mean the signal has a physical origin instead of noise. Mode 2 shows different u_x-flow directions in the top and bottom layer. The u_y current velocities however all have the same sign. This mode seems to be dominated by the u_y signal. Mode 3 might as well be noise, the relative variance is not significant.

A mathematical trick can be used to force the EOF analysis in a certain direction. It is known the tidal signal is a harmonic oscillation. Taking the second derivative should bring back the original signal, only negative. By adding two more

datasets the same way the u_y dataset was added a matrix with 72 rows can be created. This is done for Run_{72}.

It is interesting to see if the sea temperature has an effect for the EOF analysis. To do so, the first order derivative of the temperature measurement is taken, $\partial T/\partial t$, this analysis is called Run_{90}. The temperature measurement is obtained from the TRIAXYS buoy itself. The output is depicted in Figure 4.8d.

The most dominant mode is the baroclinic tide, with a relative variance of 77.40%. It's spatial mode is only apparent in the current velocities and not in the temperature. The second mode with a relative variance of 6.11% represents the influence of the sea surface temperature flux. This mode is visible in both the derivative of the temperature and the current velocities. This indicates the processes superimposed on the tidal amplitude are depended on the change in water temperature.

For a better understanding of this result the temporal patterns of the first five modes of Run_{90} are presented in Figure 4.9. They are scaled so the y-axis shows m s^{-1} in the surface layer. As discussed above Mode 1 represents influence of the tide. The higher spatial modes do not seem to show a valuable pattern in the surface layer.

Summarizing; from these EOF analysis a clear tidal signal is picked up without the occurrence of high current velocity peaks in summer. Though another mode is detected in which the sea surface temperature flux influences high current activity in summer. This seems to indicate the water temperature has an influence on peak currents.

4.1.3 Harmonic tidal analysis

In the previous section the tidal influence was picked up by the EOF analysis. Instead, a harmonic analysis can be made to separate the tidal signal from the raw measurement signal. A Matlab program called T_TIDE by PAWLOWICZ *et al.* [2002] is used, more information about this program can be found in subsection 3.3.1. For this thesis the results from ROEST [2015] are used to make the graphs in this section.

18 continuous absolute current vectors and 18 directional vectors are inserted into the Matlab script. The output will be a list of 60 tidal constituents with their properties for every bin. Table 4.2 shows only the M_2 and S_2 constituents and their major and minor axis. From this the current velocity induced by the tide can be constructed as a time series. For the first bin, the time series is plotted in Figure 4.10 (light blue) together with the raw signal (dark blue).

The spring- and neap tide cycle is clearly noticeable in the tidal signal. Now it also can be seen that the current velocities over 1 m s^{-1} in August appear superimposed on the tidal signal.

4.2 Wind influence

In the previous section the current measurements have been analyzed and a tidal fit has been made. Besides tidal influence the wind can also have a significant

Table 4.2: M_2 and S_2 tidal constituents with their major and minor axis. Per bin in which the TRIAXYS ADCP measured in

	M_2		S_2	
	major	minor	major	minor
bin 1	0.447	-0.001	0.123	0.001
bin 2	0.453	0.001	0.125	0.002
bin 3	0.453	0.003	0.124	0.003
bin 4	0.451	0.007	0.123	0.005
bin 5	0.448	0.011	0.121	0.008
bin 6	0.442	0.017	0.119	0.011
bin 7	0.434	0.025	0.116	0.015
bin 8	0.425	0.034	0.113	0.016
bin 9	0.415	0.043	0.111	0.018
bin 10	0.405	0.052	0.109	0.019
bin 11	0.395	0.059	0.107	0.020
bin 12	0.383	0.066	0.104	0.020
bin 13	0.369	0.071	0.101	0.020
bin 14	0.353	0.075	0.097	0.020
bin 15	0.281	0.067	0.076	0.019
bin 16	0.134	0.034	0.037	0.011
bin 17	0.057	0.011	0.014	0.004
bin 18	0.043	0.004	0.012	0.004

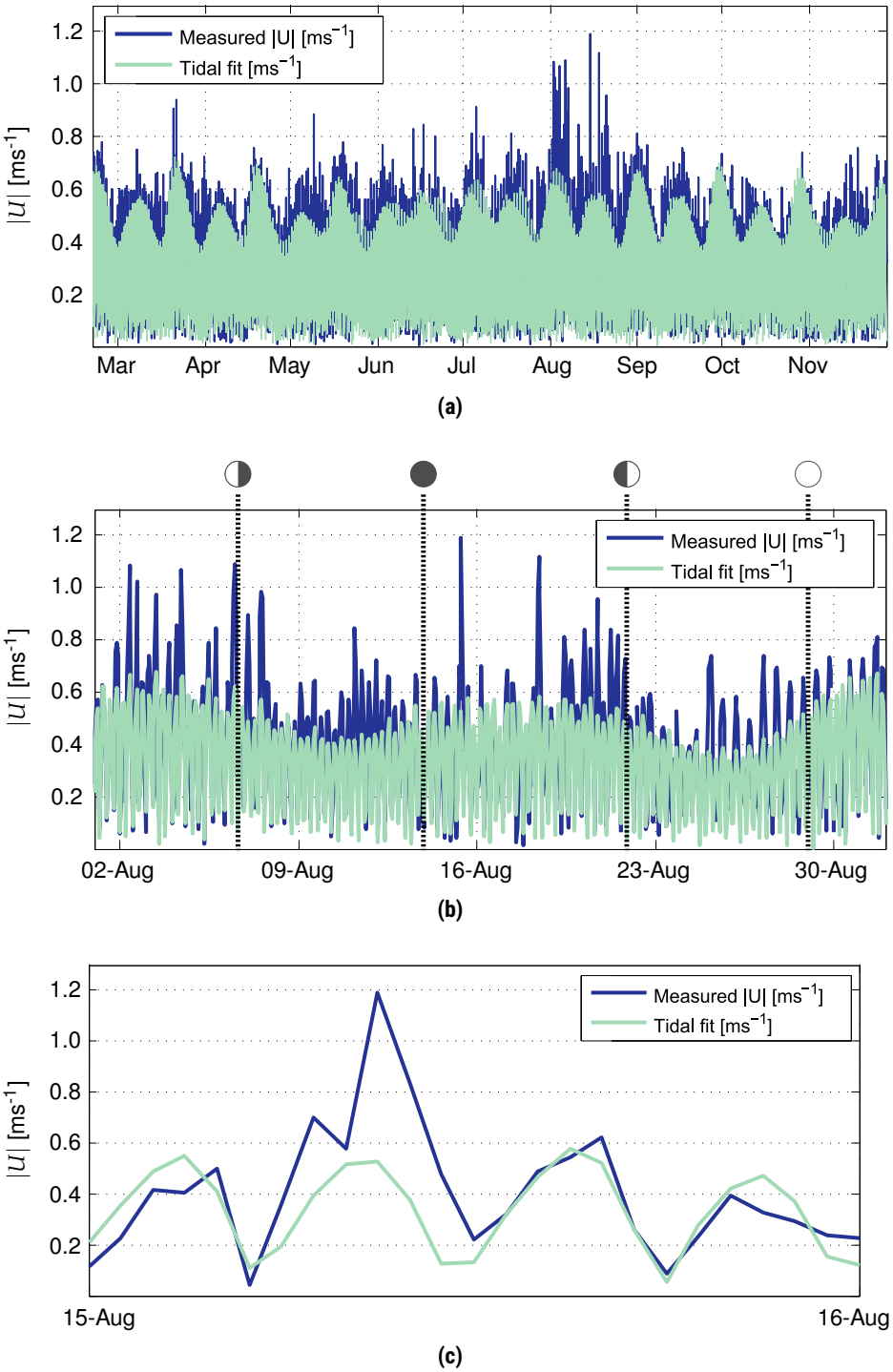

Figure 4.10: Current measurements at the Gemini location during 2015. Measurements are made at 2 m depth. The lighter line represents the result from the T_TIDE tidal analysis. **(a)** is the result for the whole year of 2015. **(b)** zooms in on the month of August only. The circles in this image represent the moon. Spring tide occurs 2.5 days after full or new moon. **(c)** further zooms in on the highest recorded current, on 15 August

Table 4.3: Pearson product-moment correlation coefficient. 1 is the maximum correlation and 0 the minimum possible. The numbers correspond to the KNMI station numbers from Figure 3.1

	207	**208**	**277**
207	1	0.85	0.71
208	0.85	1	0.83
277	0.71	0.83	1

effect on the current velocities. According to DIETRICH [1950] currents of 0.7 m s^{-1} are possible during storm surge conditions in the area. To investigate whether or not the wind could have caused the high current velocities in August the KNMI wind measurements are presented.

As discussed in subsection 3.1.2 wind measurements are not made on the project location itself. However three KNMI stations are within 60 km range of Gemini and recorded the wind velocity and direction during 2015. For the month of August the absolute wind velocity is plotted in Figure 4.11.

As can be seen the wind velocities of all three stations coincide roughly. For completeness the Pearson product-moment correlation coefficient is calculated for all three datasets for whole 2015, see Table 4.3. The value 1 indicates perfect correlation and 0 no correlation. Based on these values one can expect the wind velocities at the Gemini wind farm to roughly coincide with these time series. It is therefore justified to use one of these three time series as representative for the wind velocity at the Gemini wind park.

In August the wind velocities show a maximum of 16 m s^{-1} ($\sim$7 Bft). However, the average wind speed in the beginning of August is around 6 m s^{-1} ($\sim$3 - 4 Bft.). These wind speeds are not storm surge conditions which could explain the high current velocities. For completeness the occurence of wind speeds for the whole of 2015 are given in Figure 4.11b. As can be seen wind speeds of 24 m s^{-1} ($\sim$10 Bft.) have been measured.

The wind is the driving influence for waves. They have been measured by a waverider buoy at the Gemini location. The result is depicted in Figure 4.14, both 2015 and specifically August are plotted.

4.2.1 Barotropic model results

Based on these measurements the influence of the tide combined with the wind could not cause current velocities over 1 m s^{-1} at Gemini. There is another check that can be made to further support this claim.

The DCSMv6-ZUNOv4-KF model has computed the depth averaged current velocities at the location of the TRIAXYS buoy at the Gemini wind farm. This model is forced by wind and air pressure measurements from the KNMI, only barotropic effects are included. The resulting absolute current velocity for 2015

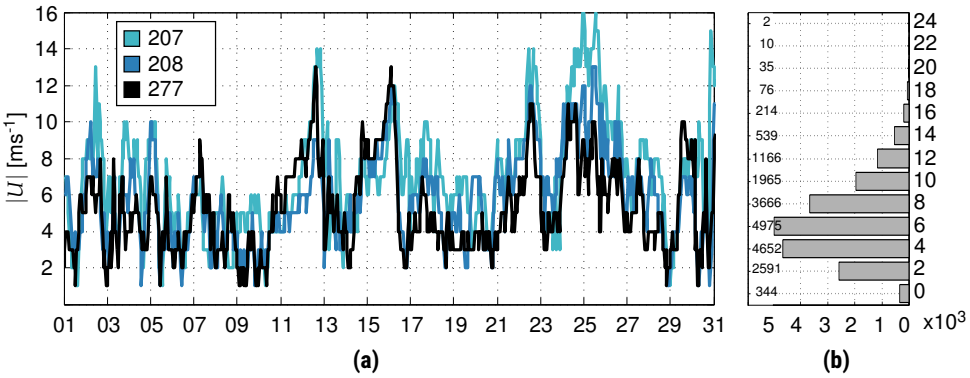

Figure 4.11: Wind velocities measured by three stations in a 60 km radius from the Gemini wind farm. **(a)** shows how these three stations coincide with one another in the month of August 2015. **(b)** gives the occurrence of all wind speeds measured during the whole of 2015

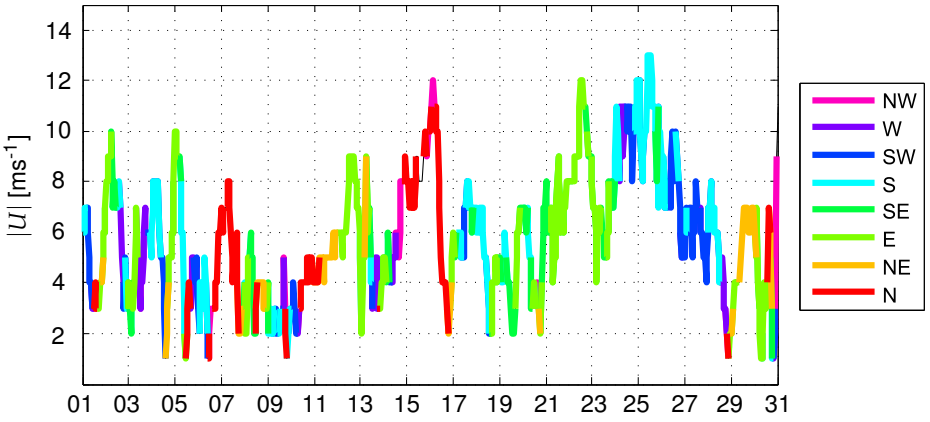

Figure 4.12: Wind velocities for August 2015 as measured by station 277. The color indicates direction from which the wind is blowing

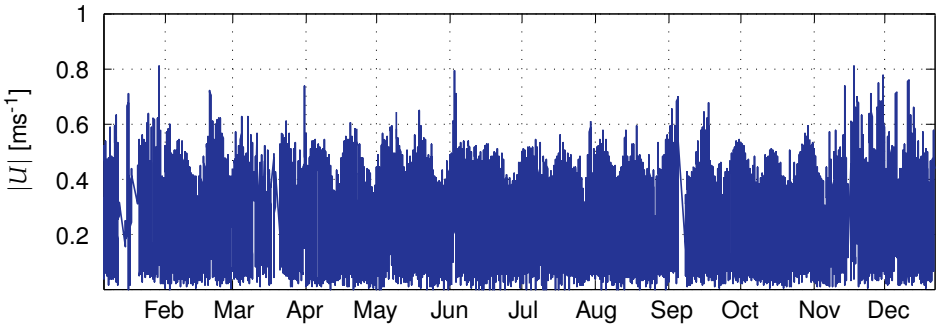

Figure 4.13: Depth averaged absolute current velocities computed by the DCSMv6-ZUNOv4-KF model

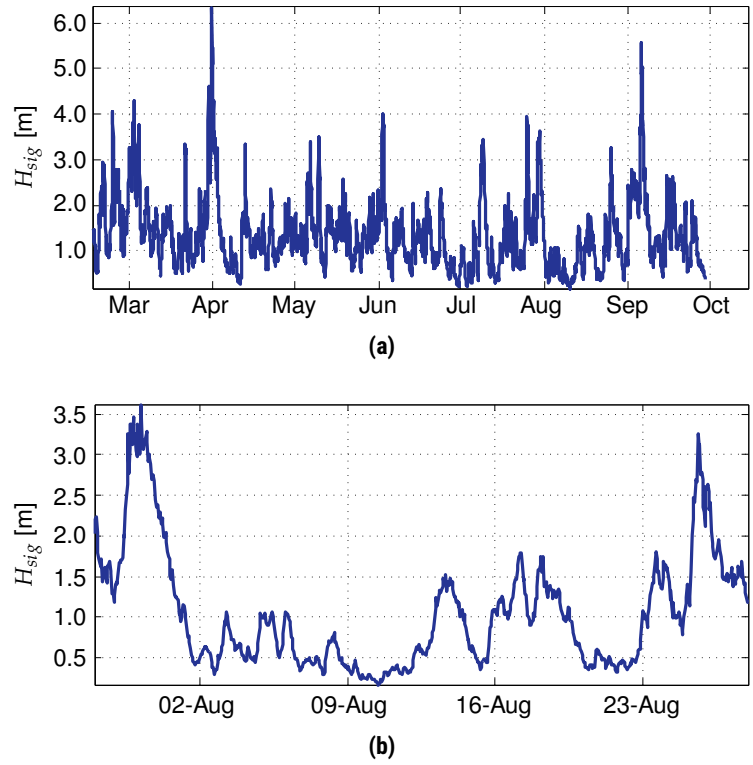

Figure 4.14: Significant wave height measured at the Gemini wind park location by the TAB02922 buoy. **(a)** is the recorded wave height over 2015. **(b)** is only the month of August

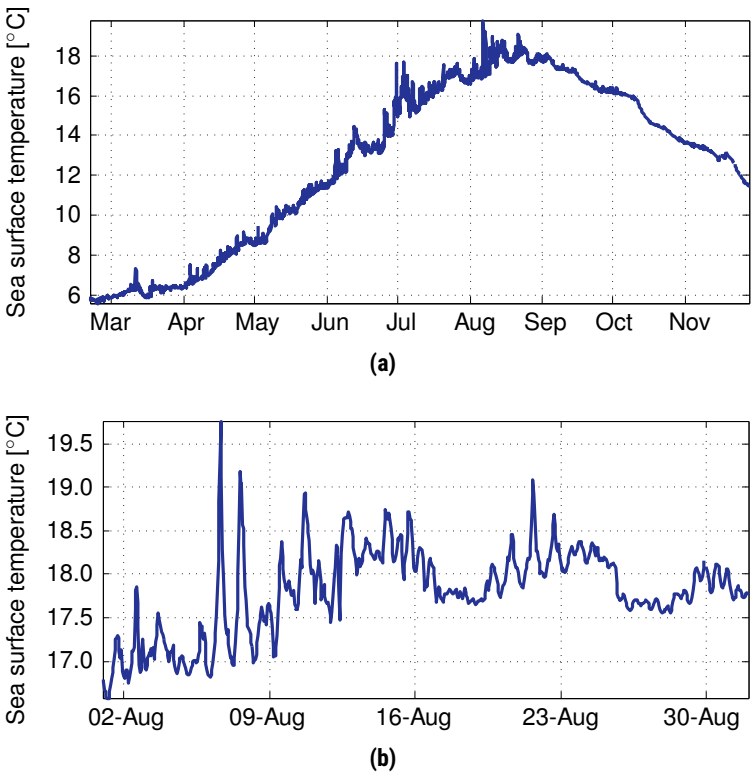

Figure 4.15: Sea surface temperature measured at the Gemini wind park location by the TRIAXYS buoy. **(a)** is the recorded temperature over 2015. **(b)** is only the month of August

is plotted in Figure 4.13. For more information about this model and how the data is processed is given in section 3.2.

The maximum computed depth-averaged current velocity is 0.81 m s^{-1}. The highest measured surface current velocity of 1.2 m s^{-1} occurred in August. Off course depth-averaged results cannot be compared with surface measurements. Though, the model results do not show an increase in current velocities late summer. Indeed, August shows even lower than average activity.

4.3 Density differences

From the previous results one can conclude the high current velocities measured in the first half of August are not caused by wind and tidal influence only. Returning to the three major mechanisms responsible for the energetic motions in the North Sea, only the forcing by density differences remains. Density differences in the North Sea waters are caused by either temperature or salinity differences, this section treats the salinity and temperature measurements made by the TW/EMS measurement station and the temperature sea surface measurements acquired by remote sensing. The surface sea temperature has also been measured by the TRIAXYS buoy at the Gemini location. The results are plotted in Figure 4.15 to gain a first insight into the water temperature.

4.3.1 TW/EMS ship

This is a measurement ship located 32 km north east from the TRIAXYS buoy at the Gemini wind farm. Salinity and temperature measurements have been made in the year of 2015. Figure 4.16 shows these measurements. Salinity is recorded in two places of the water column, at 6 and 30 m water depth. Water temperature however is measured on 3, 6, 10, 15, 20, 25 and 30 m water depth. From these measurements a contour plot is generated by interpolating these values.

Remarkable is the onset of both salinity and temperature stratification in the water column in the month of August at around the same time of the current velocity spikes. These findings further endorse the claim density differences caused these spikes.

Besides the TW/EMS measurement ship another measurement station is available in the North Sea, the FINO1 platform. This platform also measures salinity, currents and temperature throughout the water column and it is located 45 km east from the TRIAXYS buoy. These measurements have been acquired, they are however not reliable as they contain strange values. The current velocities for example, average over 2 m s^{-1} at the seabed. Temperature and salinity measurements reveal sudden shutdown after which the measurement give different values. This indicates instrument malfunction. The FINO1 measurements series of 2015 are therefore not treated in this thesis.

4.3.2 Remote sensing

To further investigate the phenomena of density induced flow more information is gathered. Using imagery from satellites, temperature fields can be generated. subsection 3.1.5 explains the methodology behind the acquisition.

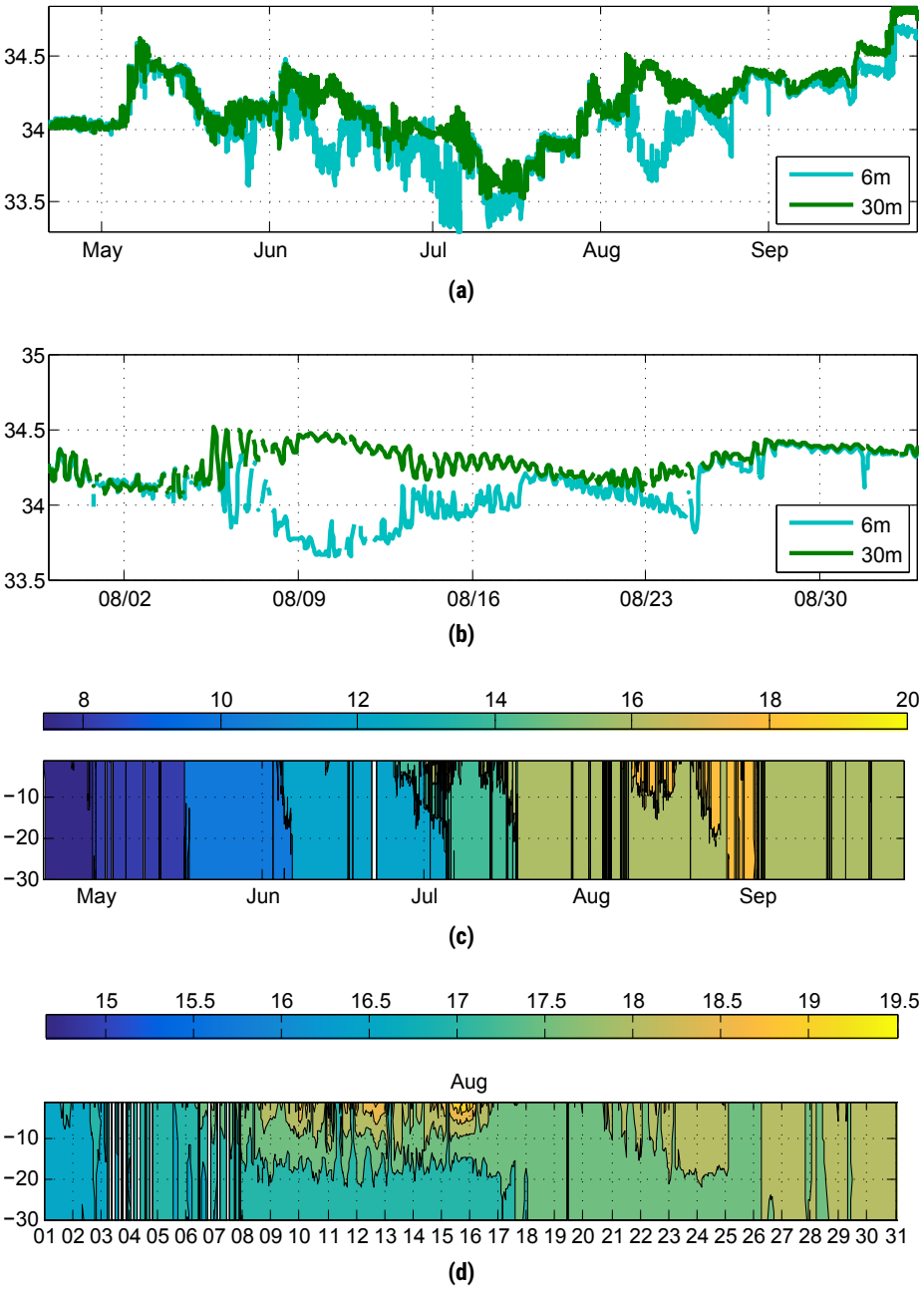

Figure 4.16: Temperature and salinity measurements through depth. Made by the TW/EMS station in 2015. Note the TW/EMS station is located 32 north east from the current measurements made at the Gemini wind farm. **(a)** Salinity measurements during 2015 at 6 and 30 meter depth. **(b)** A zoom of the salinity plot for August only. **(c)** Temperature measurements during 2015 in a contour plot. **(d)** Zoom of the same temperature during August

Usable SST measurements are made by five different satellites. Some make multiple images per day and sometimes periods go by without data. The influence of clouds makes these measurements sometimes useless. The result of processing all available satellite data for 2015 are 411 SST measurements made of the southern North Sea. These images can be found in CLAESSENS *et al.* [2016]. More detail about the the coverage per day can be found in Figure 4.17. Coverage is computed by counting the maximum amount of pixels which can be recorded per instrument. Then a bandwidth is constructed of three degrees around the actual water temperature at Gemini. For every measurement, the pixels which lie within this bandwidth are summed up, and divided by the maximum amount of pixels the instrument could record. This coverage is then binned over a day for every satellite.

With all the satellites combined, the maximum coverage is around 250% for one day. This means effectively 2.5 full SST measurements can be seen on that particular day. This is not much, there are days 30 images are available from all the satellites combined. The reason coverage seems so low is because of the clouds. There are little days the weather in The Netherlands, or the southern North Sea, is clear for 100% coverage. So even though a lot of images are available, only but a few can be used for interpretation. A strong bias is therefore observed towards unclouded days.

First an average of the SST is made for every month. By gridding the temperature pixels in a common grid, monthly averages are made by simply dividing the sum with the total amount of images. Though care has to be taken with the presence of NaN values, as the average will be affected. Having done so, the result is depicted in Figure 4.18. The seasonal cycle can be observed in the images. A band of colder water is visible in the continental and English coastal water during winter months. In summer months the warmer coastal water is visible. The same seasonal pattern is observed by PIETRZAK *et al.* [2011] in the year of 1998.

The current velocities above 1 m s^{-1} were measured in the first half of August, see Figure 4.19. Red lines are drawn in the figure, they indicate when usable satellite imagery is available. The sea surface temperature in the period of 2 - 9 August is well recorded due to the absence of clouds. Also high currents occur in this period. Figure 4.21 shows these SST recordings, with the Gemini wind farm location indicated by a red dot. Continental warm water stretches out to the project location, in some images it even seems Gemini is located exactly on a sharp border (front) between warmer and colder water.

A phenomena has been observed in the satellite images in which north of the Wadden Sea patches of warm water are visible. This phenomena, coined *warm water fingers*, is shown in Figure 4.20. These warm water structures seem to originate from the Wadden Sea. A serie of three cloudless days in June give a pollution free series of SST measurements. Depicted in Figure 4.22, these series of images show the warm water structures moving during the tide. For interpretation the tidal cycle of 10 June is given below the image.

In summary; from the three major mechanics responsible for the energetic motions in the North Sea the forcing by density difference is responsible for the high current velocities measured in August 2015. During this time both

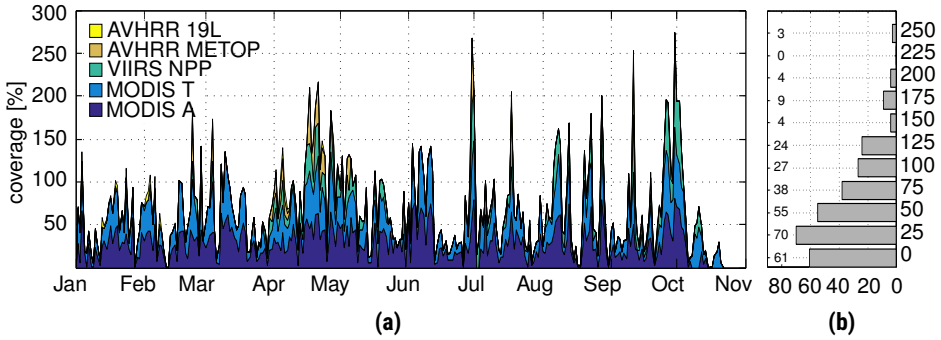

Figure 4.17: Remotely sensed SST coverage. More then 100% is possible because the coverage is cumulatively binned over an entire day. Multiple images could then add up over 100%. **(a)** area plot of the cumulative coverage of SST pixels. **(b)** gives the same cumulative coverage, only binned with an exact number

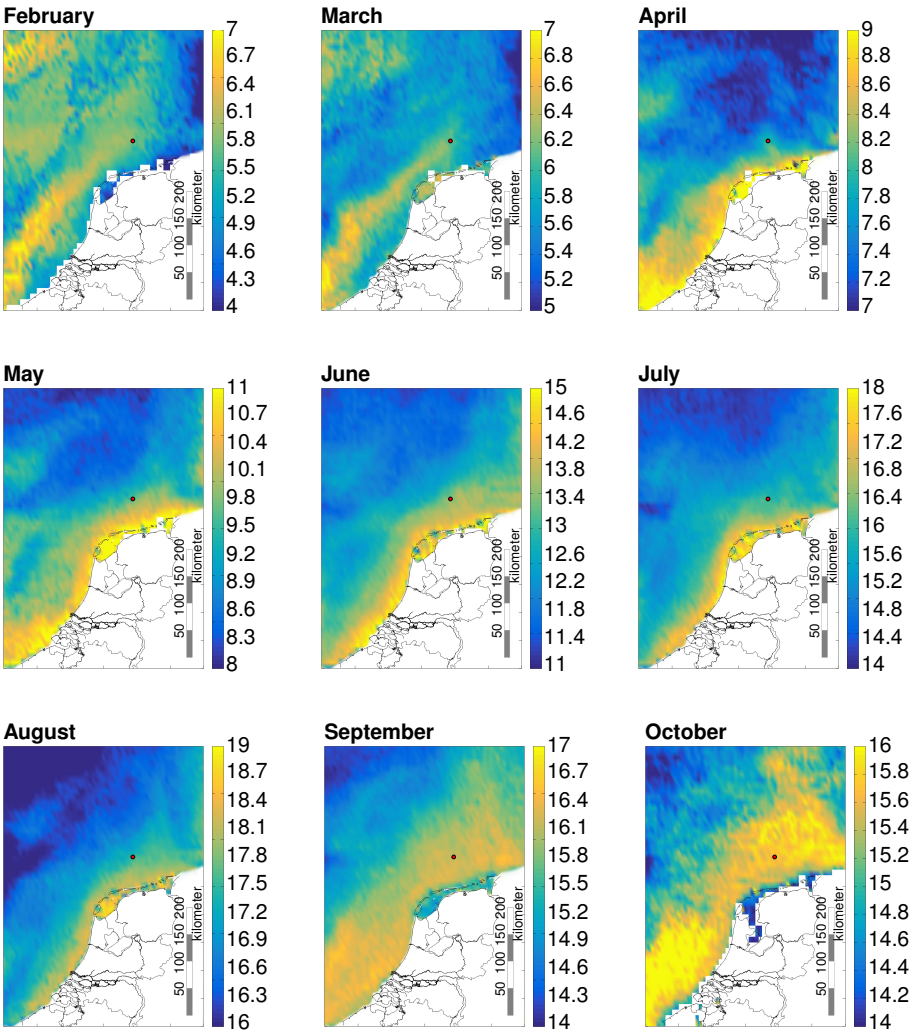

Figure 4.18: Average SST plots per month. The seasonal cycle is evident. February and march show a band of colder water in the continental and English coastal waters during the winter months. During the summer months the coastal waters are warmer. The same phenomena is observed by PIETRZAK *et al.* [2011]

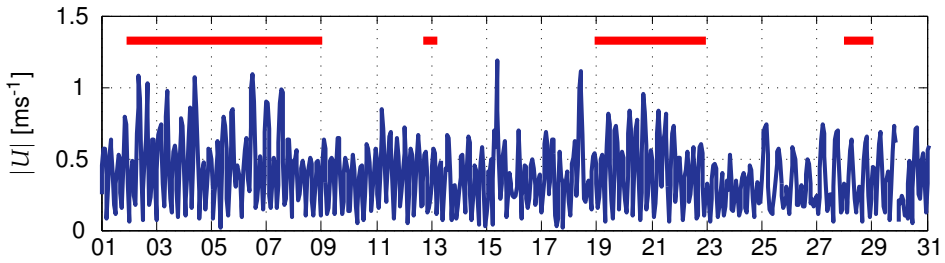

Figure 4.19: Absolute current velocity ($|U|$) measurements at the Gemini location in August 2015 at 2 m depth. Lines in red indicate periods in which good remotely sensed SST data is available

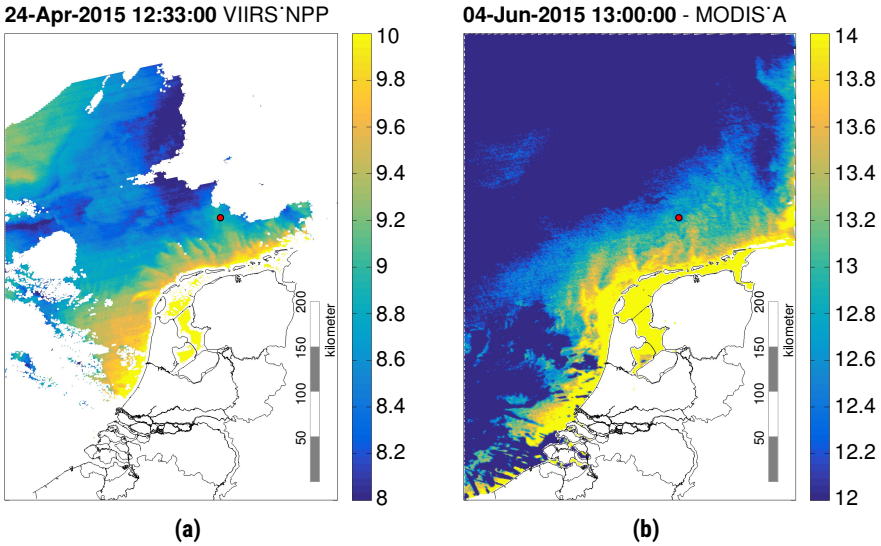

Figure 4.20: Example of warm water fingers phenomena. Warmer water is present in elongated stretches of water seeming to originate from the Wadden Sea. **(a)** is taken when the flood velocity was at its maximum. **(b)** is taken during the reversal from flood to ebb. Note: MODIS registers clouds as dark blue

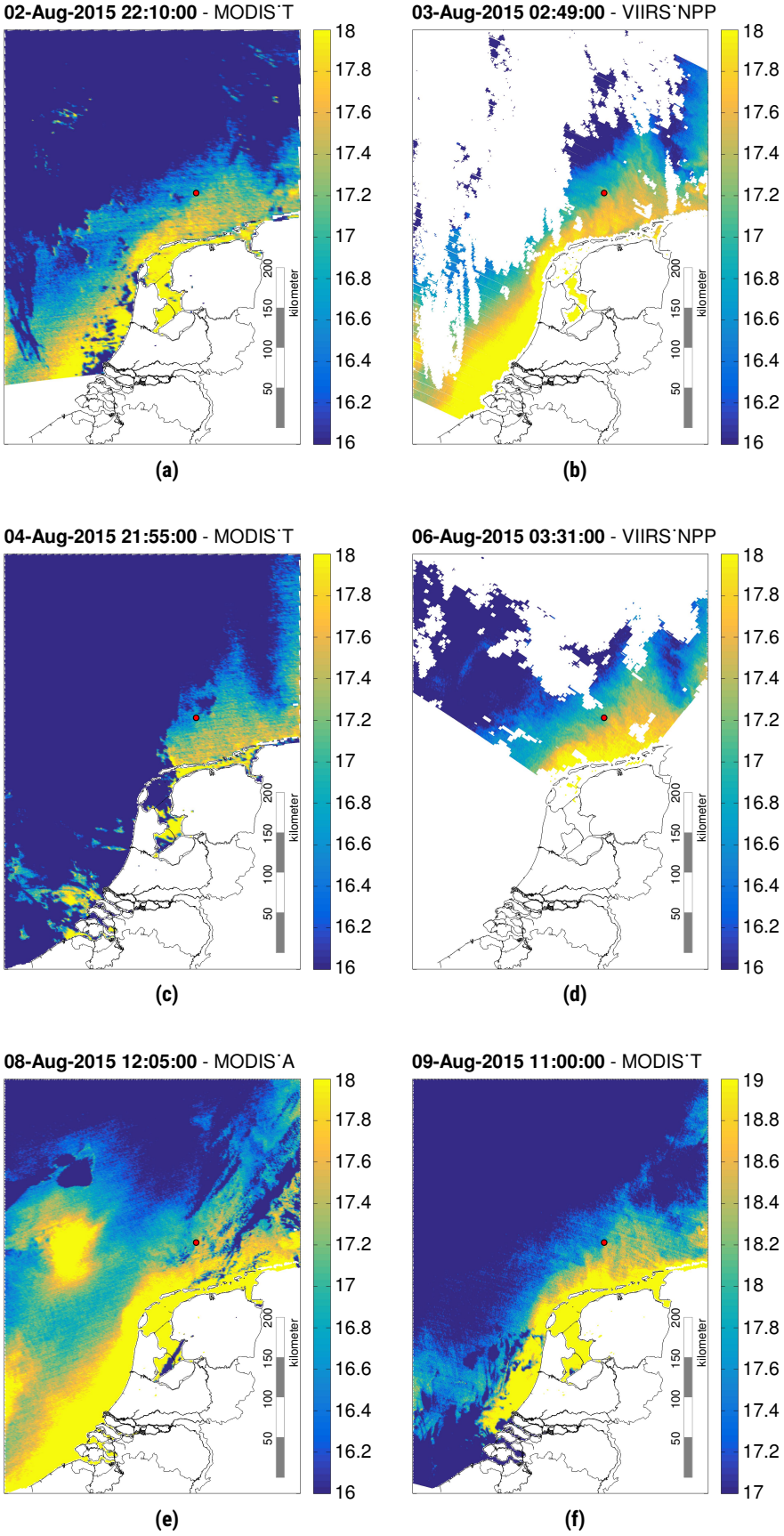

Figure 4.21: SST images from 2-9 August. During this period current velocities of over 1 m s^{-1} occurred, see Figure 4.19. The Gemini wind farm seem to be located on the front created by the warmer coastal water and the colder North Sea water. Note: MODIS registers clouds as dark blue

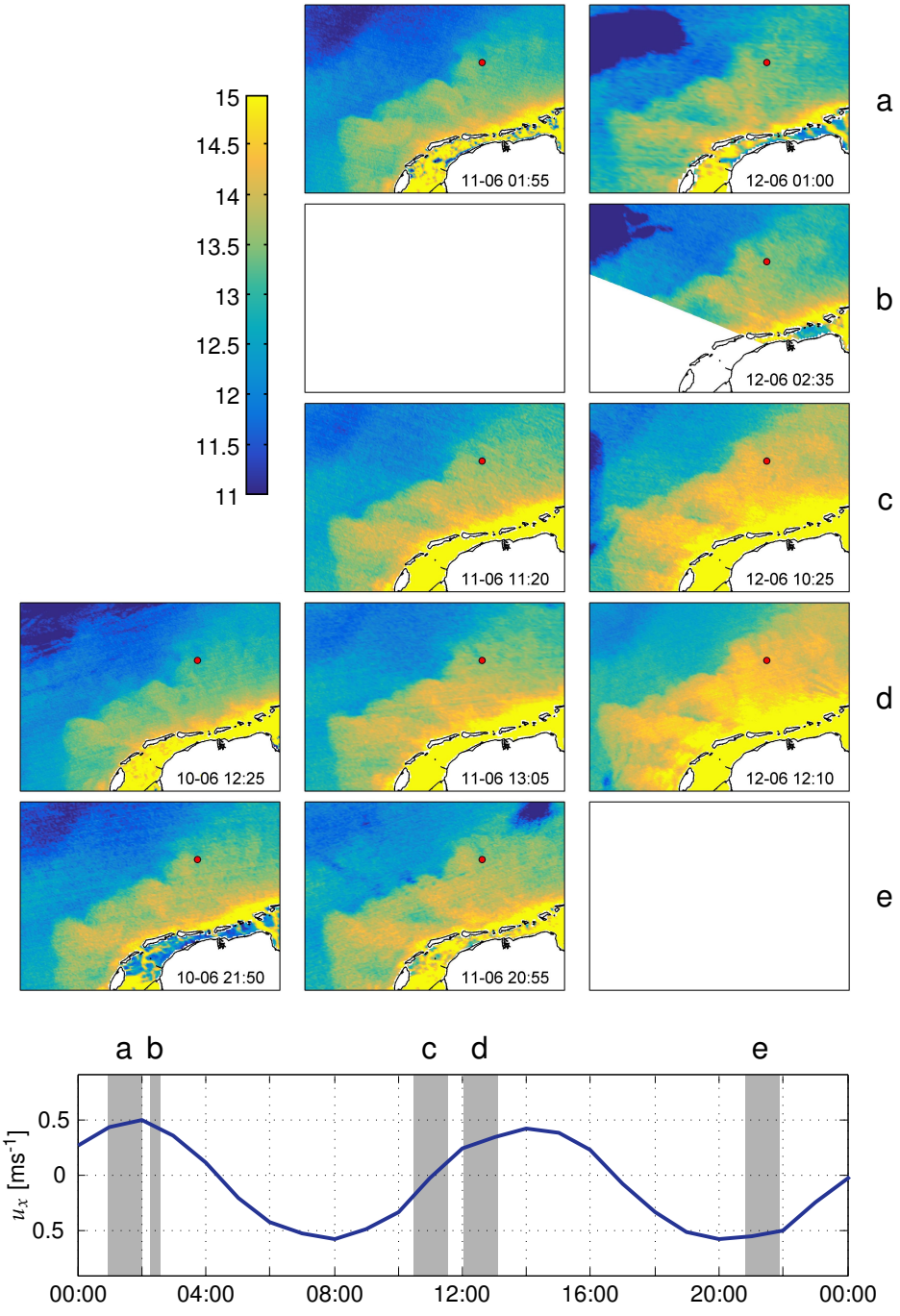

Figure 4.22: Warm water fingers during 10-12 June. Whether or not an image shows the ebb- or flood phase can be judged by looking at the time series. This shows the current velocity in x-direction (W-E). The red dot indicates the location of the Gemini wind farm

temperature and salinity stratification has been recorded by the TW/EMS measurement ship 40 km north east from Gemini. The temperature difference in water can be observed with the infrared spectrum used by satellite instruments. Satellite images are available from 2-9 August right when high current velocities occurred. In these recordings the Gemini wind farm seem to be located on the front between the warmer coastal waters and the colder North Sea water.

4.4 The Wadden Sea

In the previous section evidence has been collected possibly linking the Wadden Sea to current measurements made at the Gemini wind farm. Warmer fresher water is observed in elongated stretches of water called *warm water fingers*.

The Wadden Sea is a region of inter tidal flats in the southeastern part of the North Sea. It lies between the coast of northwestern continental Europe and the range of Frisian Islands. The Dutch part of this sea is depicted in Figure 4.23. This region receives both fresh water and additional heating compared to the North Sea.

First the numbers in Figure 4.23 indicate the location of sluices. Here considerable quantities of fresh water are discharged onto the Wadden Sea. Though the Den Oever and Kornwederzand sluice are responsible for 87% of the total yearly averaged discharge, see Table 4.4. For every sluice data is collected for the total amount of fresh water discharged onto the Wadden Sea. This value can then be translated to a average discharge per second. The cumulative result has been plotted and is displayed in Figure 4.24. For comparison the discharge at Lobith is given to give an indication of the Rhine discharge. As can be seen, in summer months the peak discharges from the sluices can be bigger then the discharge at Lobith.

Second the heating behavior of the Wadden Sea is different then that of the North Sea. Contrary to the deeper North Sea, the shallow Wadden Sea contains a large area of tidal flats, which are submerged only part of the tidal cycle. This has strong effects on the heat balance of the Wadden Sea. When tidal flats dry, they are heated by the sun in daytime. This stored heat is released from the sediment into the overlying water when becoming submerged. The tidal flats thereby contribute to the heat balance, even when not submerged [ONKEN *et al.*, 2007]. This effect will reduce the thermal response time of the Wadden Sea, allowing a fast response to meteorological forcing [VAN AKEN, 2008].

4.4.1 Warm water simulation

A simulation has been made with Delft3D to see how the results of a simplified heating model compare to the actual measured sea surface temperature at Gemini. More information about Delft3D and the used heating physics can be read in section 3.4.

Five "swimming pool" simulations have been made. With Delft3D a 5×5 grid with cell size 100×100 m has been made. For every simulation only the water depth is different. The meteorological forcing of the wind, solar radiation, cloudiness, relative humidity and air temperature are used on an hourly interval.

Table 4.4: Average and maximum freshwater discharges in $m^3\ s^{-1}$ at the different sluices for the year of 2015. The sluice numbers correspond to those in Figure 4.23.

Number	Name	Yearly averaged discharge [$m^3\ s^{-1}$]
1	Den Oever	252.43
2	Kornwederzand	241.20
3	Clevering	47.79
4	Helsdeur	11.34
5	Oostoever	6.56
6	Harlingen	2.54
7	Krassekeet	0.67
8	Dijkmanshuizen	0.67
9	Prins Hendrik	0.46
10	Eierland	0.41
11	De Schans	0.15
12	Zandkes	0.01
	Total sluices	564.23
	Lobith	1924.04

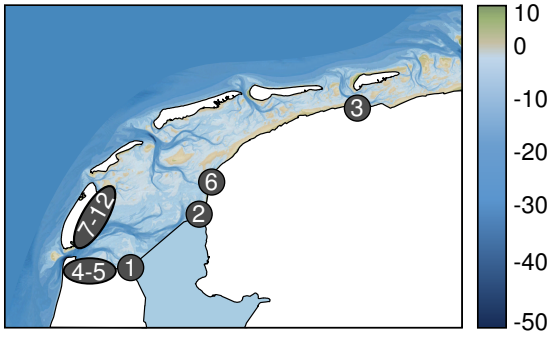

Figure 4.23: Location of sluices discharging fresh water into the Wadden Sea. The sluice numbers correspond to those in Table 4.4. Redrawn from DURAN-MATUTE *et al.* [2014]

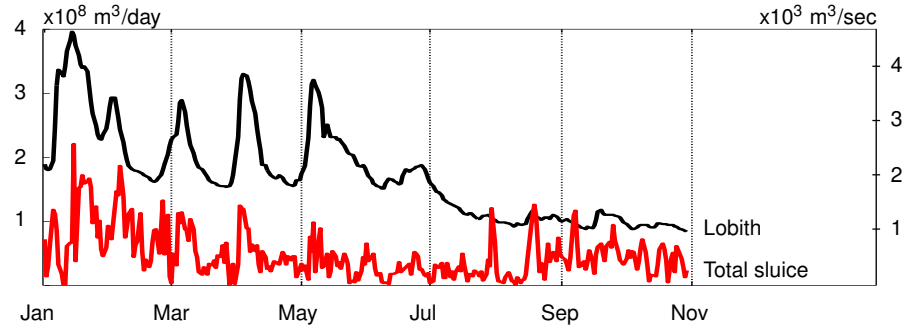

Figure 4.24: Cumulative discharge of fresh water through the sluices from Table 4.4. For comparison the discharge of the Rhine at measurement station Lobith is given

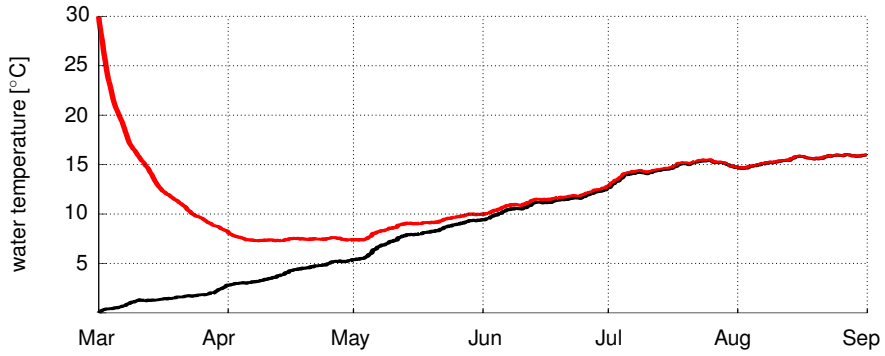

Figure 4.25: Spinup time for a 30 m depth swimming pool with two different initial conditions. The red line has water with an initial water temperature of 30 °C while the black line has a water temperature of 0 °C

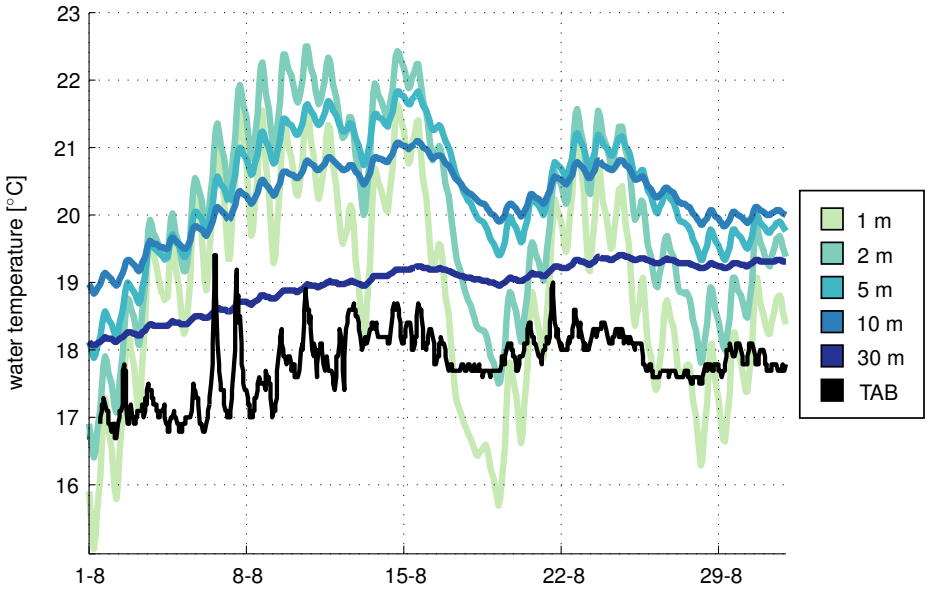

Figure 4.26: Swimming pool exercise with measurements from TAB in the month of August

For the 30 m depth simulation the spin up time has been investigated. Figure 4.25 shows the result of this investigation. First the water of the swimming pool was set to 30 °C as an initial condition after which the meteorological forcing was applied for March to September (red line). A second simulation was made in which the initial condition of the swimming pool was set to 0 °C (black line). As can be seen after 4 months both simulations reach the same water temperature. From this it can be concluded the water temperature does not feel the initial condition in August if the simulation starts in March.

For 1, 2, 5, 10 and 30 m water depth simulations have been made. Forcing is applied from March to September, but only the results of August have been plotted in Figure 4.26. For comparison the sea surface temperature measurement of the TRIAXYS buoy, the TAB02922 has been included as a black line. The water depth at the location of this buoy is around 30 m. As can be seen the actual measurements (black) are 1 °C colder then the computed swimming pool of 30 m. This makes sense, as a swimming pool has no inflow and outflow at the boundaries while in reality colder water from the North Sea is mixed by the tides. The overall shape however does coincide.

It is interesting to see the measurement has temperature peaks where the swimming pool of 30 m does not. This also has to do with the boundaries. During the measurement peaks warm water passes the measurement location which indicates the passing of warmer water bodies at the project location. The swimming pools with a smaller water depth do inhibit these temperature fluctuations.

Summarizing; The Wadden Sea contains fresher and warmer water then the North Sea. Under the influence of the tides this water is transported offshore. The heating simulation showed a swimming pool of 30 m would behave more stationary with the absence of big temperature fluctuations. In reality these fluctuations do appear.

5

Discussion

From the increasing weight of observational evidence, we now have a better picture of the mechanisms responsible for high summer currents at Gemini. Barotropic phenomena alone are not the cause. Spring tidal velocities do not exceed 0.7 m s^{-1} and wind forcing in August was the lowest of 2015. This is further confirmed by comparing the current measurements with the output of Rijkswaterstaat's barotropic DCSMv6-ZUNOv4-KF model, in which spring-tidal velocities are not exceeded in August. The hypothesis explored in this thesis is that the baroclinic currents are the most likely cause of the large velocities in August.

An EOF analysis is used to analyze the measurement signal. The resulting dominant modes represent, for a large part, the barotropic tidal signal. This is consistent with the harmonic analysis by T_TIDE providing a tidal fit on the original data [PAWLOWICZ *et al.*, 2002]. Baroclinic modes are also picked up which correlate with the change in sea water temperature over time in summer. A mathematical relationship is thus found linking episodic current events to the change in sea surface temperature.

Vertical salinity- and temperature measurements made 32 km northeast of Gemini show a seasonal stratification regime (Figure 4.16). The water column is vertically well mixed throughout the year, except during summer. Significant stratification is registered in the first half of August. It is during this period currents regularly exceed 1 m s^{-1}. Density-induced current velocities are strongest on the border between two water masses with different properties, a front. At the Gemini offshore wind park there are three possible locations from which a different water mass can emerge. The Rhine ROFI, Wadden Sea and a tidal mixing front from the central North Sea.

Fresh water from the Rhine ROFI arriving at Gemini is vertically well-mixed [DE RUIJTER *et al.*, 1997; DE BOER *et al.*, 2006, 2008, 2009; RIJNSBURGER *et al.*, 2016]. Tidal- or wind straining can stratify a vertically well-mixed body [SIMPSON, 1997]. But since the period of stratification was so long and maximum bed shear stress from waves and tides is low around Gemini, it seems unlikely tidal straining would have caused the observed stratification [PIETRZAK *et al.*, 2011]. Straining by wind is not further looked into.

The observed thermocline is further investigated using remotely sensed SST imagery. It is hard to find suitable pictures since they are so easily obscured by clouds. Still, an unique set of images from 10-12 June 2015 is found in which the weather was clear enough. The phenomena of *warm water fingers* is observed, in which elongated stretches of warm water originate from the Wadden Sea (Figure 4.22). These filaments are then advected offshore under the influence of the tide. At the time of high currents in August the weather was also clear enough to observe global temperature patterns (Figure 4.21). In the satellite images it can be seen that Gemini is located exactly on the border between colder North Sea and warmer Wadden Sea water in August. A classic tidal mixing front as predicted by the numerical model of KLEPTSOVA [2013] seems to be missing. This is not surprising as VAN AKEN [1986] predicted the onset of a tidal mixing front when salinity stratification is present. In his paper, VAN AKEN [1986] studied the area just west of Gemini. The observed vertical temperature gradient was thought to be caused by the increased heating rate of the surface layers due to the limited vertical transport of heat in the stably salt-stratified water column. The origin of fresh water was sought in precipitation excess which would work as a stabilizing agent. Though, "Since the precipitation rates, required for the onset of a stable stratification and for the supply of fresh water to the surface layer are unrealistically large, we can reject a local precipitation excess as a probable cause of the observed salt stratification" [VAN AKEN, 1986].

Rain water falling on the low lying land in the northern part of the Netherlands needs to be drained. Excess water is pumped onto rivers transporting fresh water into the IJselmeer. When possible, water in this basin is released onto the Wadden Sea through two main sluices in the Afsluitdijk. Measurements from these sluices have been analyzed. The months June and July show a low fresh water discharge of ± 500 m^3 s^{-1}. At the end of July however, three days before the salinity stratification, a pulse of fresh water is observed (Figure 4.24). With an average discharge of ± 1200 m^3 s^{-1}, the fresh water output onto the Wadden Sea exceeded that of the River Rhine at the time, which was $\pm$ 1000 m^3 s^{-1}. Fresh water discharged onto the Wadden Sea quickly becomes well-mixed before it flows into the North Sea [DURAN-MATUTE *et al.*, 2014]. This could well be the source of fresh water VAN AKEN [1986] sought in explaining the observed salt-stratified water column.

Water from the Wadden Sea is both warmer and fresher than that of the North Sea. In summer, when heating is at its strongest, this water is clearly picked up in SST images. It is warmer for two reasons. First the average water depth of 2 m allows for more rapid heating. This is further confirmed by a heating simulation in Delft3D where multiple "swimming pools" of different depth have been modeled with the meteorological forcing from 2015. Water with a smaller water depth reacts faster to the higher air temperature than deeper water (see Figure 4.26). The second reason is the "battery" working of dry tidal flats in the Wadden Sea. When tidal flats are dry during ebb, the sun still heats the dry sand plateaus. With the incoming flood the overlying water enjoys rapid heating from the solar heat stored within these flats [ONKEN *et al.*, 2007]. This makes the Wadden Sea a very effective heat pump.

We end up with a front as described by VAN AKEN [1986]. Where initially two competing ideas of an estuarine- and tidal mixing front have been brought

together to form the Wadden Sea influence (Figure 5.2). This bring into question what is meant with a tidal mixing front. If temperature is purely the main ingredient, a tidal mixing front would form further offshore. Because of the estuarine-like circulation a stratified environment is formed where a tidal mixing front can thrive. The situation in August is sketched in Figure 5.1 and Figure 5.2. A clear front is visible, exactly on the Gemini location.

Similar haline driven currents have been investigated in the Liverpool Bay area [HEAPS, 1972]. A mathematical model has been developed based on the thermal wind concept with the effects of friction (subsection 2.1.1). Maximum surface current can be computed using the salinity- and temperature measurements (Figure 4.16). From this, the maximum and minimum density become; $\rho_{\text{min}} = 1024.15$ kg m^{-3} and $\rho_{\text{max}} = 1025.31$ kg m^{-3}. With a depth of 6 m for the upper layer a maximum E-W velocity of 0.4 m s^{-1} is computed. This solution is dependent on the coefficient of friction and a value for the fresh water discharge. Nonetheless it gives a good indication of possible current velocities.

A simple balance between mixing and buoyancy can explain what happened in the first half of August. These are the competing factors determining whether a water column is mixed or stratified [SIMPSON AND BOWERS, 1981]. The tide is the largest mixing force, it is however periodic and thus predictable. The second largest mixing term is the wind. This is far less predictable and has a dynamic character. Buoyancy forces can be allocated to the intensity of solar heating and the amount of fresh water discharged onto the Wadden Sea. Heating from the sun is more in summer than it is in winter. The main dynamic buoyancy force then becomes the fresh water discharged by surrounding sluices. Figure 5.3 shows the most important dynamic mixing and buoyancy forces in the same graph. A few days before the high currents begin, a large fresh water pulse is observed. Followed by the lowest winds in 2015, this allowed the Wadden Sea influence to reach all the way to the Gemini offshore wind park (Figure 5.1). Hence a period of stratification is measured close to Gemini and high current velocities are recorded at the project location.

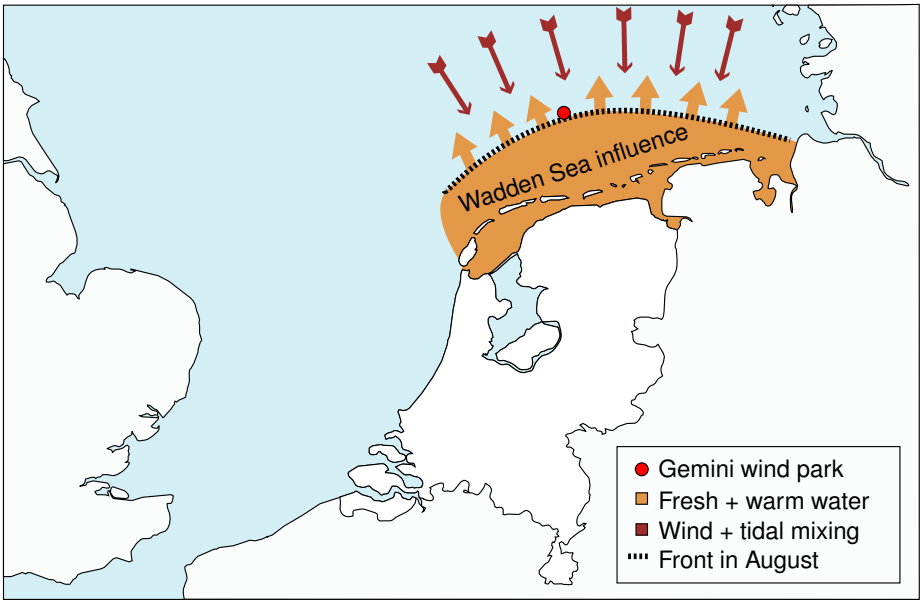

Figure 5.1: Overview map of the area. The orange area indicates the influence of warmer and fresher water from the Wadden Sea in August 2015. The dark red arrows represent mixing due to wind or tides. The location of the front (dashed line) moves according to the balance between mixing and buoyancy. Gemini is located at the red dot

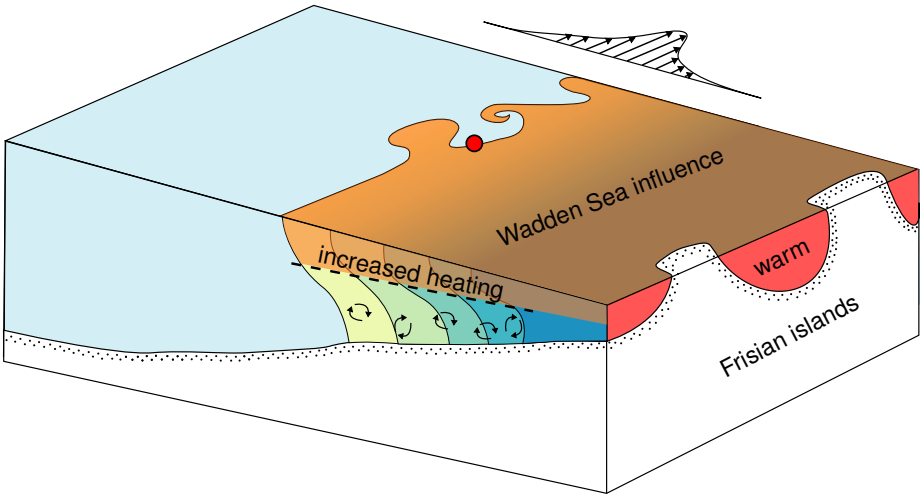

Figure 5.2: The Wadden Sea influence initialized by fresh water stratification from the Wadden Sea. The surface layer can now heat up to form a tidal front. The red dot indicates the location of Gemini, right on top of the front in August. Drawing is a combination between images from SIMPSON [1997]; HILL *et al.* [1993]; SIMPSON *et al.* [1981]; VAN AKEN [1986]

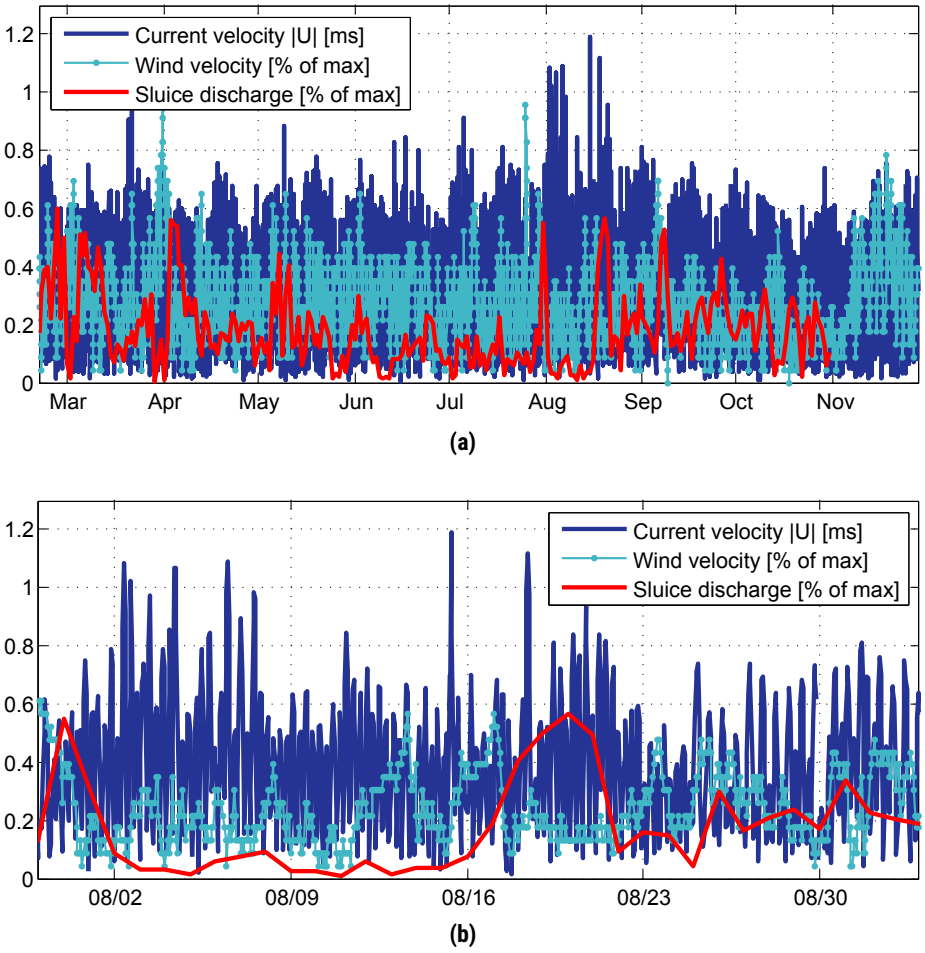

Figure 5.3: Plot of the current velocities together with the fresh water discharge onto the Wadden Sea and the wind velocity in the North Sea. Note, the wind and sluice discharge are given as a percentage of their maximum value. Sluice discharge never reaches a value of 1 in this graph because the maximum discharge occurred in January. **(a)** gives the result from March to the end of November. **(b)** is the result for August only

6

Conclusions and recommendations

6.1 Conclusions

The research presented in this thesis has improved our understanding of frontal activity north of the Wadden Sea and the currents associated with them. Little is known about current velocities in the area around the Gemini offshore wind park. The information available has been acquired and analyzed to form a complete as possible story.

In the beginning of August currents of up to 1.2 m s^{-1} are measured at Gemini. At this time spring tidal currents are 0.7 m s^{-1} and wind velocities are the lowest for whole 2015. At the same time, temperature and salinity stratification is measured in the water column 32 km northeast of Gemini.

SST satellite imagery show Gemini to be located in a region with fronts at the time of the high currents. Exactly between warm water from the Wadden Sea and colder water from the North Sea. A phenomena coined *warm water fingers* has been observed. Long elongated bodies of warm water originating from the tidal inlets of the Wadden Sea stretching $\sim$ 50 km into the North Sea. These events are rare, though, a set of three unclouded days show these fingers evolving in time. A tidal mixing front formed offshore, as predicted by SIMPSON AND HUNTER [1974]; PINGREE AND GRIFFITHS [1978]; KLEPTSOVA [2013] is not observed.

It is found that fresh water discharged onto the Wadden Sea is responsible for a stable salt stratification as described by VAN AKEN [1986]. Turbulent eddies are suppressed in the halocline allowing the surface layer to rise in temperature without it getting vertically mixed. A tidal mixing front will form within this region, instead of far offshore. Three days preceding the high current period a pulse of fresh water was discharged onto the Wadden Sea. This buoyancy provided the Wadden Sea influence with potential energy. During the following week winds were the lowest of 2015, making the mixing force small. This allowed the Wadden Sea influence to move significantly offshore, right on the Gemini location. Stratification associated with this front then led to effectively doubling the estimated surface currents at the Gemini wind farm. Lastly, a mathematical model by [HEAPS, 1972] is used to show density-currents of 0.4 m s^{-1} are viable under the measured conditions.

6.2 Recommendations

The metocean report used for this project underestimated the possible current velocities, as they were more then 20% as high as expected [DHI WASY, 2012]. A barotropic model was used neglecting the effects of stratification. For future projects in the same area a baroclinic model will give more accurate results.

Wind straining is not looked into. It is expected the wind can induce vertical stratification on a well-mixed water column. This is an area of research unexplored at the Gemini location.

The German FINO1 measurement station located to the west of Gemini records current velocities through depth with an ADCP. More than a decade of data is available at the BSH (The Bundesamt für Seeschifffahrt und Hydrographie). This study could be extended with the research of the FINO1 dataset.

6.2.1 Van Oord

For Van Oord current information is useful when making workability assessments. The future of the Wadden Sea will bring the construction of many more wind parks. I would recommend Van Oord to install additional salinity and temperature recorders onto the already installed monopiles. These measurement can provide an indication of the stratification in the water column, providing a better prediction methodology. High currents will appear when the waters are stratified, and they can persevere as long as the waters remain stratified.

In the National Energy Agreement, more then 40 parties have agreed that 16% of energy must be generated sustainably by 2023. Offshore wind energy is an indispensable part of this. It has been agreed that offshore wind energy should be generating a total of 4,450 MW of electricity by 2023. This can supply electricity to more than 5 million households. That means an extra 3,450 MW on top of the 1,000 MW that has already been built or is under construction. One of the areas the Dutch Government chooses to develop in the years to come is right next to the Gemini area. This is exactly on the border in which episodic density-induced currents, as explained in this thesis, are generated.

I am grateful to Arjen Costerus of Van Oord for kindly providing me with the buoy current data. Without this private dataset the research in this thesis would be impossible. The German TW/EMS dataset also provided free salinity and temperature measurements. However, the Dutch government does not have salinity-, temperature-, or current measurement stations in the vicinity of Gemini. For every offshore platform built in the Dutch North Sea it is allowed to place measurement equipment onto it. Especially with the upcoming necessity for renewable energy and the need to cut costs in offshore wind, a proper understanding of the environment is an absolute prerequisite. The Dutch government could add a clause in offshore wind contracts stating a proper and complete measurement station needs to be installed at every corner of a wind park, making them coastal observatories. Data could be easily transfered, as all cables are already in place. The possibilities of such an open dataset are endless. For project costs in the order of billions, such a measurement installation would be only a small addition. The insights obtained from the new research are not

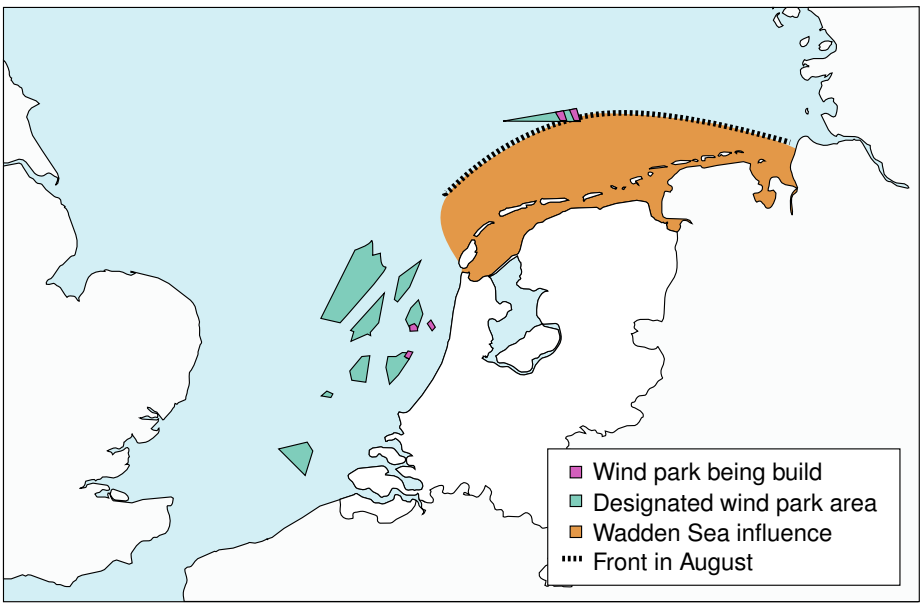

Figure 6.1: Plans of the Dutch government for placing offshore wind parks. The purple areas have already been built, while the green areas are locations for future wind parks

only valuable for academics; the advances in lowering offshore wind costs could be so significant, making the return of investment almost instant.

Appendix A

SVD decomposition

SVD is one of the most useful matrix factorizations in applied linear algebra with applications such as data compression or solving linear equations. SVD gives us an optimal low-rank representation of a system, getting rid of the least important modes. This method can be applied to time series as well, which is especially useful for this research.

In this section the SVD factorization will be elaborated. First linear algebra will be used for the formal definition. Then an example will be used for physical interpretation.

Suppose A is an $m \times n$ matrix. Then there exists the SVD factorization of the form:

$$A = USV^T \tag{A.1}$$

Where the columns of U are the left singular vectors $\vec{u}_i$. The entries on the diagonal of S are the singular values (s_i). And the columns of V (the rows of V^T) are the right singular vectors $\vec{v}_i$.

The values of S can be seen as the eigenvalues to our problem. The height of any one singular value is indicative of its importance in explaining the data. More specifically, the square of each singular value is proportional to the variance explained by each singular vector. The formal description of the SVD holds the conjugate transpose of V, (V^*), since the values discussed in this thesis hold only real numbers, thus not imaginary, the normal transpose can be used instead of the conjugate ($V^* = V^T$). Both matrix U and V have the property to be orthogonal matrices, this means: $UU^T = I$ holds.

After this decomposition, matrix A can be partially reconstructed. Providing insight into the (mathematically) most important modes of the original signal. This property proves to be very useful for interpreting time series, an example will be used explain the interpretation of these modes.

In the North Sea 10 measuring stations record the sea surface elevation. Each of these sensors has the same problem of recording a lot of noise. The measurement of one station is depicted in Figure A.01, as can be seen a clear sine pattern is noticeable caused by tidal motions.

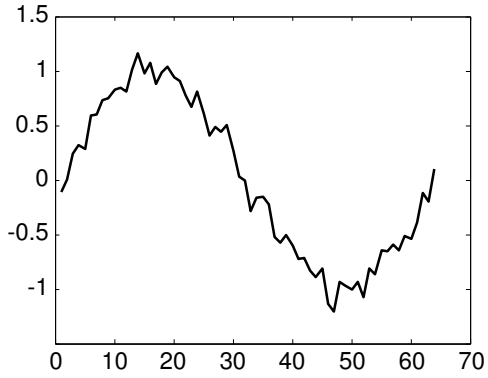

Figure A.01: Measurements of one measuring station in the North Sea. The tidal influence can be seen, but each stations records a lot of noise as well. In total 20 of these signals have been produced

From all 10 measurement time series matrix A can be constructed:

$$A_{t_m,10} = \begin{bmatrix} a_{t_1,1} & a_{t_1,2} & \cdots & a_{t_1,10} \\ a_{t_2,1} & a_{t_2,2} & \cdots & a_{t_2,10} \\ \vdots & \vdots & \ddots & \vdots \\ a_{t_m,1} & a_{t_m,2} & \cdots & a_{t_m,10} \end{bmatrix} \tag{A.2}$$

With each column representing a different measurement station and each row containing the time of measurement. For this matrix the singular value decomposition can be made resulting in the matrices U, S, and V, see eq (A.1). The diagonal matrix S contains the importance of the modes ordered from high to low.

$$S = \begin{bmatrix} 17.73 & 0 & \cdots & 0 \\ 0 & 1.11 & \cdots & 0 \\ \vdots & \vdots & \ddots & \vdots \\ 0 & 0 & \cdots & 0.47 \end{bmatrix} \tag{A.3}$$

As can be seen in Eq. (A.3) the first value ($s_{1,1}$) is almost 17 times as large as the second diagonal value ($s_{2,2}$). This means most of the original measurement signal can be reproduced by only using one mode of the SVD decomposition. The relative variance is obtained by dividing the values of S by the sum of S, see Figure A.03.

The term "mode" is used for the vectors of U. As mentioned before, these vectors are also called, the left singular vectors u_i. Vectors u_1 and u_2 are plotted in Figure A.02. It now becomes clear the measurement signal can be explained by a dominant mode ($s_1 = 17.73$) followed by 9 smaller modes (s_2 to s_{10}). These lesser modes consist of the noise also apparent in the original measurement signal. Noise is random, no mathematical description can be made explain-

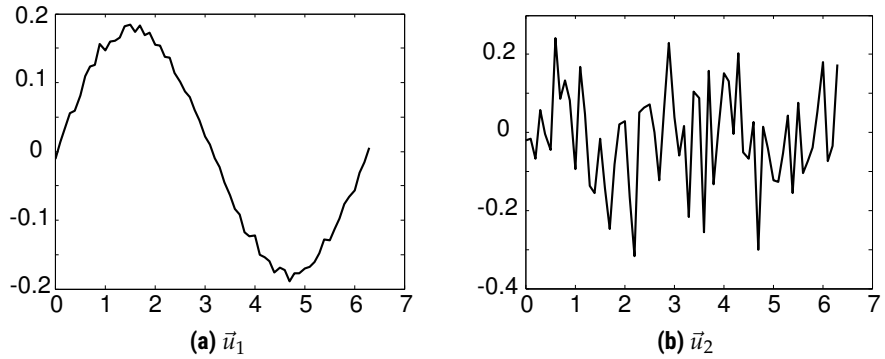

Figure A.02: The first two left singular vectors of example matrix A. **(a)** has a singular value of 17.73 while **(b)** has a singular value of 1.11. This difference indicates the raw signal of matrix A can largely be reconstructed using only one mode (left singular vector). Notice only shape is displayed, the y-axis has no physical meaning

ing/predicting it[1]. So basically the SVD decomposition was able to explain the measurements made by a sine wave with noise superimposed onto it.

Note Figure A.02 displays the shape of modes, values on the y-axis have no physical meaning.

The right singular vectors can be interpreted to give the relation between the left singular vector and the different measurement stations. Imagine this by looking at the first and second left singular vector ($\vec{u}_1$ and $\vec{u}_2$, Figure A.02). Mode $\vec{u}_1$ represents the tidal component of the sea surface elevation. For every measurement station this is signal should be the same. On the other hand, the noise signal ($\vec{u}_2$) is very different for every measurement station. This is because of the inherent random nature of noise. Now the implication of Figure A.04 becomes clear. The x-axis are the 10 different measurement stations. The solid black line indicates the dominant tidal signal which is (about) the same for every measurement station. The dotted red line, indicating the noise signal, is different for every measurement station.

Using both left- and right singular vectors together with the singular values from matrix S the original measurement signal can be (partially) reconstructed.

$$\sum_{i=1}^{i=10} \vec{u}_i \cdot s_i \cdot \vec{v}_i^T \tag{A.4}$$

With i the amount of modes to be incorporated into the reconstruction. Now we can choose to only reconstruct the dominant tidal mode of the signal by choosing $i = 1$. The result from this algebraic operation are 10 vectors, one for every measurement station. Here the reconstructed dominant mode for

[1]This holds for true noise. The computer generated noise from this example is not "pure" random. The random number generator in a computer is an algorithm which is always based on some input value (often the clock).

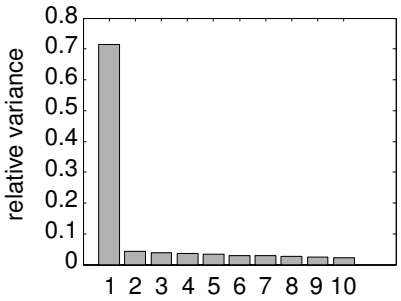

Figure A.03: Relative variance $s_i / \sum_{i=1}^{i=10} s_i$ for every mode ($\vec{u}_i$)

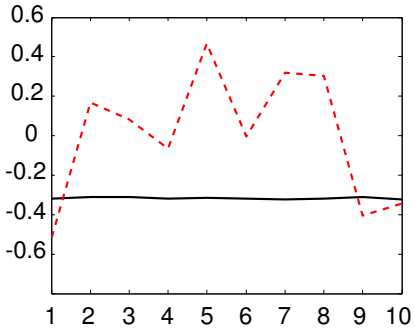

Figure A.04: The first two right singular vectors of A. The solid black line is the first right singular vector $\vec{v}_1$. The dotted red line the second vector $\vec{v}_2$

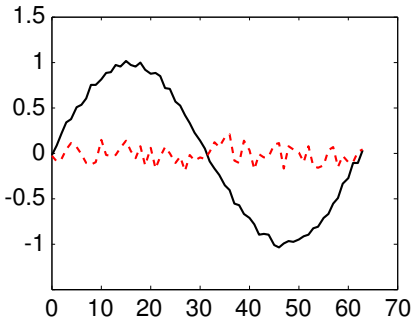

Figure A.05: Reconstructed dominant mode of the signal as the black line. The dotted red line is the reconstruction of the 2nd dominant mode. Note, these are separate components

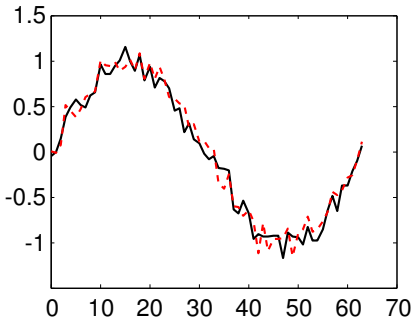

Figure A.06: Reconstruction using the dominant mode (sine) and the 2nd dominant mode (noise). The result is the original measurement signal, but know composed out of two signals. Note, these are the combination of two modes

measurement station 1 is plotted by the following operation:

$$\vec{u}_1 \cdot s_1 \cdot v_{1,1} \tag{A.5}$$

See Figure A.05 the solid black line. The same operation can be made by replacing the 1 with 2. The result will be the reconstructed second mode for measurement station 1. This is also depicted in Figure A.05, only now as the dotted red line. It is after this operation the y-axis has a physical meaning again.

The reconstruction using two modes is super positioned and placed in a graph together with the original measurement of measurement station 1. This can be seen in Figure A.06.

The signals recorded by the measurements stations have been created in Matlab using a sine function with random noise super imposed onto it. The sine has amplitude 1 and the noise amplitude 0.1. It is clear the dominant mode

represents this sine function quite accurately. The more measurement stations available, the better the sine fit will be. A mathematical perfect sine will be achieved when the measurement stations go to infinity.

Bibliography

ALVERA-AZCÁRATE, A., BARTH, A., BECKERS, J.M. AND WEISBERG, R.H. (2007) Multivariate reconstruction of missing data in sea surface temperature, chlorophyll, and wind satellite fields. *Journal of Geophysical Research*, 112(C3). doi:10.1029/2006JC003660

BROWN, J., HILL, A.E., FERNAND, L. AND HORSBURGH, K.J. (1999) Observations of a seasonal jet-like circulation at the central North Sea cold pool margin. *Estuarine, Coastal and Shelf Science*, 48(3), 343–355. doi:10.1006/ecss.1999.0426

CAMPBELL, J.B. AND WYNNE, R.H. (2011) Introduction to remote sensing. Guilford Press. doi:10.3390/rs5010282

CLAESSENS, C., DE BOER, G.J. AND PIETRZAK, J.D. (2016) SST images, southern North Sea in 2015. Van Oord

DE BOER, G.J. (2009) On the interaction between tides and stratification in the Rhine Region of Freshwater Influence. Ph.D. thesis, TU Delft, Delft University of Technology

DE BOER, G.J., PIETRZAK, J.D. AND WINTERWERP, J.C. (2006) On the vertical structure of the Rhine region of freshwater influence. *Ocean Dynamics*, 56(3-4), 198–216. doi:10.1007/s10236-005-0042-1

DE BOER, G.J., PIETRZAK, J.D. AND WINTERWERP, J.C. (2008) Using the potential energy anomaly equation to investigate tidal straining and advection of stratification in a region of freshwater influence. *Ocean Modelling*, 22(1-2), 1–11. doi:10.1016/j.ocemod.2007.12.003

DE BOER, G.J., PIETRZAK, J.D. AND WINTERWERP, J.C. (2009) SST observations of upwelling induced by tidal straining in the Rhine ROFI. *Continental Shelf Research*, 29(1), 263–277. doi:10.1016/j.csr.2007.06.011

DE RUIJTER, W.P., VISSER, A.W. AND BOS, W. (1997) The Rhine outflow: a prototypical pulsed discharge plume in a high energy shallow sea. *Journal of marine Systems*, 12(1), 263–276. doi:10.1016/S0924-7963(96)00102-9

DELTARES, D. (2014) Delft3D-FLOW user manual. *Delft, the Netherlands*

DHI WASY (2012) Offshore Wind Farms GEMINI: ZeeEnergie & Buitengaats. Updated Metocean Report (14801465). *Metocean report*, Typhoon Offshore

DIETRICH, G. (1950) Die natürlichen Regionen von Nord-und Ostsee auf hydrographischer Grundlage. *Kieler Meeresforsch*, 7(2), 35–69

DIETRICH, G. (1953) Verteilung, Ausbreitung und Vermischung der Wasserkörper in der südwestlichen Nordsee auf Grund der Ergebnisse der „Gauss "-Fahrt im Februar/März 1952. *Ber. Dtsch. Wiss. Komm. Meeresf. HF J*, 3

DURAN-MATUTE, M., GERKEMA, T., DE BOER, G.J., NAUW, J.J. AND GRÄWE, U. (2014) Residual circulation and freshwater transport in the Dutch Wadden Sea: a numerical modelling study. *Ocean Science*, 10(4), 611–632. doi:10.5194/os-10-611-2014

EISMA, D. AND KALF, J. (1987) Distribution, organic content and particle size of suspended matter in the North Sea. *Netherlands Journal of Sea Research*, 21(4), 265–285. doi:10.1016/0077-7579(87)90002-0

EKMAN, V.W. (1905) On the influence of the earth's rotation on ocean currents. *Ark. Mat. Astron. Fys.*, 2, 1–53

GARRETT, C.J.R. AND LODER, J.W. (1981) Dynamical aspects of shallow sea fronts. *Philosophical Transactions of the Royal Society of London A: Mathematical, Physical and Engineering Sciences*, 302(1472), 563–581. doi:10.1098/rsta.1981.0183.

GHRSST (2008) A Proposal for Refined GHRSST GDS 2.0 Satellite Level Definitions and Naming Convention

GILL, A.E. (1982) Atmosphere-ocean dynamics, vol. 30. Academic press. doi:10.1002/qj.49711046322

GLADKOVA, I., IGNATOV, A., SHAHRIAR, F., KIHAI, Y., HILLGER, D. AND PETRENKO, B. (2016) Improved VIIRS and MODIS SST Imagery. *Remote Sensing*, 8(2), 79. doi:10.3390/rs8010079

HEAPS, N.S. (1972) Estimation of density currents in the Liverpool Bay area of the Irish Sea. *Geophysical Journal International*, 30(4), 415–432. doi:10.1111/j.1365-246X.1972.tb05825.x

HILL, A., JAMES, I., LINDEN, P., MATTHEWS, J., PRANDLE, D., SIMPSON, J., GMITROWICZ, E., SMEED, D., LWIZA, K., DURAZO, R. AND OTHERS (1993) Dynamics of tidal mixing fronts in the North Sea [and discussion]. *Philosophical Transactions of the Royal Society of London A: Mathematical, Physical and Engineering Sciences*, 343(1669), 431–446. doi:10.1098/rsta.1993.0057

HILL, A.E., BROWN, J., FERNAND, L., HOLT, J., HORSBURGH, K.J., PROCTOR, R., RAINE, R. AND TURRELL, W.R. (2008) Thermohaline circulation of shallow tidal seas. *Geophysical Research Letters*, 35(11). doi:10.1029/2008GL033459

HOLT, J.T. AND JAMES, I.D. (1999) A simulation of the southern North Sea in comparison with measurements from the North Sea Project Part 2 Suspended Particulate Matter. *Continental Shelf Research*, 19(12), 1617–1642. doi:10.1016/S0278-4343(99)00015-1

HORNER-DEVINE, A.R., HETLAND, R.D. AND MACDONALD, D.G. (2015) Mixing and Transport in Coastal River Plumes. *Annual Review of Fluid Mechanics*, 47(1), 569–594. doi:10.1146/annurev-fluid-010313-141408

JAMES, I. (1978) A note on the circulation induced by a shallow-sea front. *Estuarine and Coastal Marine Science*, 7(2), 197–202. doi:10.1016/0302-3524(78)90075-0

KANTHA, L.H. AND CLAYSON, C.A. (2000) Numerical models of oceans and oceanic processes, vol. 66. Academic press

KLEPTSOVA, O. (2013) Unstructured Orthogonal Meshes for Modeling Coastal and Ocean Flows. Ph.D. thesis, TU Delft, Delft University of Technology. doi:10.4233/uuid:f3ba6eb1-bccc-4999-a667-6ee92b65161d

KNMI (2006) Handboek Waarnemingen. KNMI

LANE, A. (1989) The heat balance of the North Sea. *Proudman Oceanographic Laboratory*

LARSSON, B. AND ESBJÖRN, E. (1955) Cloud Cover Algorithm. *SMHI IO-BN*

LIANG, X. AND IGNATOV, A. (2013) AVHRR, MODIS, and VIIRS radiometric stability and consistency in SST bands: AVHRR-MODIS-VIIRS Consistency. *Journal of Geophysical Research: Oceans*, 118(6), 3161–3171. doi:10.1002/jgrc.20205

LWIZA, K., BOWERS, D. AND SIMPSON, J. (1991) Residual and tidal flow at a tidal mixing front in the North Sea. *Continental Shelf Research*, 11(11), 1379–1395. doi:10.1016/0278-4343(91)90041-4

MATHER, P.M. AND KOCH, M. (2011) Computer processing of remotely-sensed images: an introduction. John Wiley & Sons. doi:10.1002/9780470666517.ch4

MCCANDLISS, R.R., JONES, S.E., HEARN, M., LATTER, R. AND JAGO, C.F. (2002) Dynamics of suspended particles in coastal waters (southern North Sea) during a spring bloom. *Journal of Sea Research*, 47(3), 285–302. doi:10.1016/S1385-1101(02)00123-5

MCCAVE, I. (1987) Fine sediment sources and sinks around the East Anglian Coast (UK). *Journal of the Geological Society*, 144(1), 149–152. doi:10.1144/gsjgs.144.1.0149

ONKEN, R., CALLIES, U., VAESSEN, B. AND RIETHMÜLLER, R. (2007) Indirect determination of the heat budget of tidal flats. *Continental Shelf Research*, 27(12), 1656–1676. doi:10.1016/j.csr.2007.01.029

PAWLOWICZ, R., BEARDSLEY, B. AND LENTZ, S. (2002) Classical tidal harmonic analysis including error estimates in MATLAB using T_TIDE. *Computers & Geosciences*, 28(8), 929–937. doi:10.1016/S0098-3004(02)00013-4

PIETRZAK, J.D., DE BOER, G.J. AND ELEVELD, M.A. (2011) Mechanisms controlling the intra-annual mesoscale variability of SST and SPM in the southern North Sea. *Continental Shelf Research*, 31(6), 594–610. doi:10.1016/j.csr.2010.12.014

PINGREE, R. AND GRIFFITHS, D. (1978) Tidal fronts on the shelf seas around the British Isles. *Journal of Geophysical Research: Oceans*, 83(C9), 4615–4622. doi:10.1029/JC083iC09p04615

PRANDLE, D. (1978) Residual flows and elevations in the southern North Sea. *Proceedings of the Royal Society of London. Series A, Mathematical and Physical Sciences*, 189–228. doi:10.1098/rspa.1978.0039

PRANDLE, D. (1982) The vertical structure of tidal currents. *Geophysical & Astrophysical Fluid Dynamics*, 22(1-2), 29–49. doi:10.1080/03091928208221735

PROUDMAN, J. AND DOODSON, A.T. (1924) The principal constituent of the tides of the North Sea. *Philosophical Transactions of the Royal Society of London. Series A, Containing Papers of a Mathematical or Physical Character*, 224, 185–219. doi:10.1098/rsta.1924.0005

RIJNSBURGER, S. (2014) Stratification and mixing in the Rhine region of fresh water influence; Analysing two parallel transects. Master's thesis, TU Delft, Delft University of Technology

RIJNSBURGER, S., VAN DER HOUT, C.M., VAN TONGEREN, O., DE BOER, G.J., VAN PROOIJEN, B.C., BORST, W.G. AND PIETRZAK, J.D. (2016) Simultaneous measurements of tidal straining and advection at two parallel transects far downstream in the Rhine ROFI. *Ocean Dynamics*, 66(5), 719–736. doi:10.1007/s10236-016-0947-x

ROEST, L.W.M. (2015) Predicting currents at the Gemini wind farm (#3573176). Internship report, TU Delft, Delft University of Technology

SIMPSON, J. (1997) Physical processes in the ROFI regime. *Journal of marine systems*, 12(1), 3–15. doi:10.1016/S0924-7963(96)00085-1

SIMPSON, J. (1998) The Celtic Seas. *The Sea*, 11, 659–698

SIMPSON, J. AND HUNTER, J. (1974) Fronts in the Irish sea. *Nature*, 250, 404–406. doi:10.1038/250404a0

SIMPSON, J.H., BOS, W.G., SCHIRMER, F., SOUZA, A.J., RIPPETH, T.P., JONES, S.E. AND HYDES, D. (1993) Periodic stratification in the Rhine ROFI in the North Sea. *Oceanologica Acta*, 16(1), 23–32

SIMPSON, J.H. AND BOWERS, D. (1981) Models of stratification and frontal movement in shelf seas. *Deep Sea Research Part A. Oceanographic Research Papers*, 28(7), 727–738

SIMPSON, J.H., BROWN, J., MATTHEWS, J. AND ALLEN, G. (1990) Tidal straining, density currents, and stirring in the control of estuarine stratification. *Estuaries*, 13(2), 125–132. doi:10.2307/1351581

SIMPSON, J.H., CRISP, D.J. AND HEARN, C. (1981) The shelf-sea fronts: implications of their existence and behaviour [and discussion]. *Philosophical Transactions of the Royal Society of London A: Mathematical, Physical and Engineering Sciences*, 302(1472), 531–546

SUMIHAR, J. (2012) Development of a Kalman filter for DCSMv6

VAN AKEN, H.M. (1986) The onset of seasonal stratification in shelf seas due to differential advection in the presence of a salinity gradient. *Continental Shelf Research*, 5(4), 475–485

VAN AKEN, H.M. (2008) Variability of the water temperature in the western Wadden Sea on tidal to centennial time scales. *Journal of Sea Research*, 60(4), 227–234. doi:10.1016/j.seares.2008.09.001

VAN WIECHEN, J. (2011) Modelling the wind-driven motions in the Rhine ROFI. Master's thesis, TU Delft, Delft University of Technology

WEBER, J.E. (1983) Steady wind-and wave-induced currents in the open ocean. *Journal of Physical Oceanography*, 13(3), 524–530. doi:10.1175/1520-0485(1983)013<0524:SWAWIC>2.0.CO;2

YANAGI, T. (1987) Classification of "siome", streaks and fronts. *Journal of the Oceanographical Society of Japan*, 43(3), 149–158. doi:10.1007/BF02109215

ZIJL, F. (2013) Development of the next generation Dutch Continental Shelf Flood Forecasting models: Set-up, calibration, and validation. *Deltares Report (draft)*

ZIJL, F. AND TIESSEN, M. (2015) Stromingsvalidatie DCSMv6 en DCSMv6-ZUNOv4